

DEPARTMENT OF PHYSICS AND ASTRONOMY

UNIVERSITY OF HEIDELBERG

Diploma Thesis

in Physics
submitted by

Johanna Lena Gramling

born in Groß-Umstadt, Germany

2011

Azimuthally Sensitive Hanbury Brown–Twiss Interferometry measured with the ALICE Experiment

**This diploma thesis has been carried out by Johanna Lena Gramling
at Physikalisches Institut, University of Heidelberg
under the supervision of
Prof. Dr. Johanna Stachel**

Azimuthally Sensitive Hanbury Brown–Twiss (HBT) Interferometry measured with the ALICE Experiment

Bose–Einstein correlations of identical pions emitted in high-energy particle collisions provide information about the size of the source region in space-time. If analyzed via HBT Interferometry in several directions with respect to the reaction plane, the shape of the source can be extracted. Hence, HBT Interferometry provides an excellent tool to probe the characteristics of the quark-gluon plasma possibly created in high-energy heavy-ion collisions.

This thesis introduces the main theoretical concepts of particle physics, the quark-gluon plasma and the technique of HBT interferometry. The ALICE experiment at the CERN *Large Hadron Collider* (LHC) is explained and the first azimuthally-integrated results measured in Pb–Pb collisions at $\sqrt{s_{NN}} = 2.76$ TeV with ALICE are presented. A detailed two-track resolution study leading to a global pair cut for HBT analyses has been performed, and a framework for the event plane determination has been developed. The results from azimuthally sensitive HBT interferometry are compared to theoretical models and previous measurements at lower energies. Oscillations of the transverse radii in dependence on the pair emission angle are observed, consistent with a source that is extended out-of-plane.

Azimuthalwinkelabhängige Hanbury Brown–Twiss (HBT) Interferometrie mit dem ALICE Experiment

Bose-Einstein Korrelationen identischer Pionen, erzeugt in hochenergetischen Teilchenkollisionen, liefern Informationen über die räumliche Ausdehnung der Quelle. Werden diese durch HBT-Interferometrie in verschiedenen Richtungen zur Reaktionsebene analysiert, so lässt sich die Form der Quelle messen. HBT-Interferometrie bietet damit eine hervorragende Möglichkeit, Charakteristika eines Quark-Gluon-Plasmas, das in einer hochenergetischen Schwerionenkollision entstehen kann, zu untersuchen.

In dieser Arbeit wird der theoretische Rahmen der Teilchenphysik, das Quark-Gluon-Plasma und die Technik der HBT-Interferometrie eingeführt. Das ALICE Experiment am CERN *Large Hadron Collider* (LHC) wird vorgestellt und die ersten Ergebnisse der richtungsintegrierten Analyse von Pb–Pb Kollisionen bei $\sqrt{s_{NN}} = 2.76$ TeV, gemessen mit ALICE, werden präsentiert. Ein Paar-Cut für HBT-Analysen wurde entwickelt, ebenso wie ein Framework zur Bestimmung der Reaktionsebene. Schließlich werden die Ergebnisse der azimuthalwinkelabhängigen HBT-Interferometrie mit theoretischen Modellen und früheren Messung verglichen. Die transversalen Radien zeigen deutliche Oszillationen in Abhängigkeit vom Paaremissionswinkel, die konsistent sind mit der Interpretation einer Quelle mit größerer Ausdehnung außerhalb der Reaktionsebene.

Contents

1. Introduction	1
2. Theoretical Background	3
2.1. The Standard Model of Particle Physics	3
2.1.1. Forces and Particle Spectrum	4
2.1.2. Electroweak Interaction	5
2.1.3. Quantum Chromodynamics	5
2.1.4. Chiral Symmetry	6
2.1.5. Confinement and Asymptotic Freedom	8
2.2. The Quark-Gluon Plasma	10
3. The ALICE Experiment	15
3.1. The Large Hadron Collider (LHC)	15
3.2. Challenges for ALICE as a Heavy-Ion Detector	16
3.3. ALICE Sub-detectors	17
3.3.1. The Inner Tracking System (ITS)	18
3.3.2. The Time-Projection Chamber (TPC)	19
3.3.3. The Transition-Radiation Detector (TRD)	19
3.3.4. The Time-Of-Flight Detector (TOF)	20
3.3.5. Specialized Detectors	20
3.3.6. Forward Detectors	21
3.4. Data Acquisition and Event Reconstruction	21
3.4.1. Data Acquisition (DAQ)	21
3.4.2. Event Simulation and Reconstruction	22
4. Hanbury Brown–Twiss (HBT) Interferometry	25
4.1. Introduction	25
4.2. Theoretical Formalism	25
4.2.1. From Particle Spectra to the Correlation Function	26
4.2.2. Gaussian Parametrization	29
4.3. Experimental Technique	31
4.3.1. Fitting	33
4.4. Observed Systematics of the HBT Radii, measured with ALICE	34
4.4.1. Dependence on Particle Density	34
4.4.2. Pair Transverse Momentum Dependence	36

4.4.3. Lifetime and Homogeneity Volume	37
4.5. Summary	37
5. Two-Track Resolution	41
5.1. Analysis Framework and Data Sample	41
5.2. Variables Describing the Track Separation	43
5.2.1. Angular Distance in $\Delta\eta$ and $\Delta\varphi$	43
5.2.2. Angular Distance in $\Delta\eta$ and $\Delta\varphi^*$	44
5.2.3. Angular Distance in $\Delta\eta$ and $\Delta\varphi_{min}^*$	45
5.2.4. Consideration of the Opening Angle α	48
5.3. Optimization of the Cut	50
5.3.1. k_T Dependence	50
5.3.2. Cross-check: Different Ranges for $R_{CA\varphi}$	51
5.3.3. Cross-check: η Dependence	52
5.3.4. Cross-check: $(\Delta\eta, \Delta\varphi)$ after Applying the Cut	53
5.4. Impact on HBT Analyses	53
5.4.1. Different k_T Ranges	55
5.4.2. Comparison of <i>Cowboy</i> and <i>Sailor</i> Pairs	55
5.4.3. Fit Results	55
5.5. Summary	56
6. The Event Plane as Azimuthal Reference	59
6.1. Event Plane Method	60
6.1.1. Event Plane Resolution	61
6.2. The Analysis Framework	63
6.2.1. Analysis Procedure	63
6.2.2. Event and Track Selection	64
6.3. Performance	65
6.3.1. φ Correction	65
6.3.2. p_T Weights	67
6.3.3. Control Histograms	68
6.3.4. Centrality Dependence	69
6.4. Monte Carlo Comparison	70
6.5. Event Plane Resolution	72
6.6. Summary	74
7. Azimuthally Sensitive HBT Interferometry	77
7.1. Analysis Technique	78
7.1.1. Event, Track and Pair Selection	80
7.1.2. Corrections	82
7.1.3. Systematic Effects	85
7.2. Results	90
7.3. Comparison to RHIC and Theoretical Models	94

7.4. Summary	99
8. Summary and Outlook	103
Bibliography	105
List of Figures	111
List of Tables	113

1. Introduction

What makes up the universe? What is the origin of mass? Why is more matter than antimatter existing in the universe? What was the state of matter shortly after the big bang? These are some of the most urgent questions in modern physics and the *Large Hadron Collider* (LHC) at CERN was built to shed light on these mysteries from the perspective of high-energy particle physics. In November 2009, the first pp collisions took place in the LHC, shortly after, the machine achieved an unprecedented center-of-mass energy of $\sqrt{s} = 7$ TeV. Only one year later the first Pb–Pb collisions at $\sqrt{s_{NN}} = 2.76$ TeV marked the start of the LHC heavy-ion program.

In heavy-ion collisions at high energies a large amount of energy is compressed in a very small volume, resulting in enormous pressure and very high temperatures, comparable to the conditions that are presumed to have existed in the early state of the universe. The ALICE experiment is optimized to study these high-energy heavy-ion collisions in detail to obtain insight into the state of matter shortly after the big bang, the so-called quark-gluon plasma.

The lifetime of the fireball of hot and dense matter created in heavy-ion collisions is too short to allow a direct measurement of positions and size. However, particle correlations allow to study the space-time extension of the fireball even under such conditions. The measurement presented in this thesis uses the Bose–Einstein correlation of identical pions to extract the size of the fireball in different directions and thus measure the shape of this region. This technique is called *azimuthally sensitive HBT interferometry*.

This diploma thesis summarizes my work within the ALICE collaboration. I have contributed to the first publication on HBT interferometry in Pb–Pb collisions at the LHC by preparing a comparison of the data to theoretical model predictions. The two-track resolution obtained with ALICE is important for many analyses, I studied the dependence of the pair reconstruction efficiency on the angular distance of the pair tracks and developed a cut to avoid a bias on HBT results. Furthermore, I have developed a framework for the event plane determination that is now being used collaboration-wide. The main part of this thesis work is the development of the azimuthally sensitive HBT analysis and the performance of this measurement in Pb–Pb collisions.

After an introduction of the theoretical background of particle physics and the quark-gluon plasma in Chapter 2, the ALICE detector is explained in Chapter 3. Thereafter, the technique of HBT interferometry is described, as well as the first results obtained with the ALICE experiment at the LHC (Chapter 4). The study of the two-track resolution is explained in Chapter 5 and the event plane framework is introduced in Chapter 6. Finally, the azimuthally sensitive HBT interferometry analysis is explained and the results measured in Pb–Pb collisions are presented and compared to theoretical predictions and previous measurements (Chapter 7).

2. Theoretical Background

Conclusions on the properties of the state of matter shortly after the big bang, the so-called quark-gluon plasma (QGP), can be drawn from the reaction products in high-energy heavy-ion collisions. This requires a good understanding of the underlying physics of quarks and gluons and the formation of their bound states, the hadrons. In the last 50 years of particle physics a framework, known as the Standard Model, has been developed which is able to describe almost all experimental observations.

In this Chapter, the Standard Model of particle physics is introduced and the theory of the QGP is established. The concepts of the most important analysis strategies to study the QGP are presented as well.

2.1. The Standard Model of Particle Physics

The Standard Model is formulated as a four-dimensional quantum field theory. It is a perturbative gauge theory with the underlying symmetry group $SU(3) \times SU(2) \times U(1)$. Fundamental particles are treated as excitations of fields and interactions are mediated by the gauge bosons of the theory [1].

Although the Standard Model is very successful in describing precision data from various particle physics experiments, some open questions remain [2]:

- The Higgs boson which is predicted by the Standard Model and essential for the origin of the mass of quarks, charged leptons, and the electroweak gauge bosons is yet to be found.
- Fine tuning of several parameters is required to lead to a consistent theory.
- The coupling strengths of the interactions do not unify at high energies.
- Neutrinos, a particle species that is massless in the Standard Model, are found to have very small but finite masses.
- The study of the rotation curves of galaxies led to the conclusion that there is 5-10 times more so-called Dark Matter in the universe than ordinary matter [3]. The Standard Model cannot provide a candidate particle that could make up this Dark Matter.

There are many possible scenarios beyond the Standard Model under discussion. One possibility is to extend the Standard Model symmetry by a so-called supersymmetry, connecting fermions and bosons. Furthermore, some theories assume extra spatial dimensions, either relatively large or strongly compactified. Alternatively, elementary particles can be treated no longer as point-like but as composed objects or as extended strings. Theoretical models extending the Standard Model are based on one or a combination of these ideas.

Until one of these models is found to be realized in nature, the Standard Model remains a very successful and well-tested theory that precisely agrees with most experimental data although it has the limitations mentioned above. Since the Standard Model is an effective theory up to the TeV scale, the Large Hadron Collider (LHC) delivering collisions at several TeV center-of-mass energy will hopefully allow an insight in new physics beyond the Standard Model.

2.1.1. Forces and Particle Spectrum

There are four known fundamental forces in the universe: gravity, the electromagnetic, the weak and the strong force. Gravity is not included in the Standard Model since it is much weaker than the other forces and its role in high-energy particle physics is negligible. The forces included in the Standard Model are described within gauge theories. They are mediated by force carrier particles, the gauge bosons. For electromagnetic interactions the gauge boson is the *photon*, strong interactions are mediated by a *gluon* octet, the weak force is transmitted by the Z^0 and W^\pm bosons.

The elementary matter particles of the Standard Model are fermions with spin 1/2, called *quarks* and *leptons*. Whereas leptons only interact via the electromagnetic and weak force, quarks also interact via the strong force. The particles occur in three generations, each covering a different mass regime. Every generation contains a quark pair: *up* and *down*, *charm* and *strange*, *top* and *bottom*. Each generation also has a lepton pair containing an *electron*, *muon* or *tauon* together with the corresponding massless *neutrino* (Table 2.1).

There are no free quarks and gluons observed in nature. They are confined, which means they only occur in bound states, so-called *hadrons*: either two quarks (*mesons*) or three quarks (*baryons*) (see Section 2.1.5). Ordinary matter is made up by particles of the first generation, the lightest set of particles. Up and down quarks build nucleons, protons and neutrons, which are bound together to nuclei. Together with electrons they form the atoms that make up all the matter around us.

	1 st generation	2 nd generation	3 rd generation	force carriers
quarks	u	c	t	$W^{+,-}$
	$2/3 e$	$2/3 e$	$2/3 e$	$\pm 1 e$
	$1.7 - 3.3 \text{ MeV}/c^2$	$1.27^{+0.07}_{-0.09} \text{ GeV}/c^2$	$172 \pm 2.2 \text{ GeV}/c^2$	$80.4 \pm 0.02 \text{ GeV}/c^2$
	d	s	b	Z^0
	$-1/3 e$	$-1/3 e$	$-1/3 e$	0
	$4.1 - 5.8 \text{ MeV}/c^2$	$101^{+29}_{-21} \text{ MeV}/c^2$	$4.19^{+0.18}_{-0.06} \text{ GeV}/c^2$	$91.2 \pm 0.02 \text{ GeV}/c^2$
leptons	ν_e	ν_μ	ν_τ	$\gamma(\text{photon})$
	0	0	0	0
	$< 2 \text{ eV}/c^2$	$< 2 \text{ eV}/c^2$	$< 2 \text{ eV}/c^2$	$< 1 \cdot 10^{-18}$
	e	μ	τ	g (gluon)
	$-1 e$	$-1 e$	$-1 e$	0
	$0.511 \text{ MeV}/c^2$	$105.7 \text{ MeV}/c^2$	$1776.8 \pm 0.16 \text{ GeV}/c^2$	0

Table 2.1.: The observed Standard Model particles with their electromagnetic charge and mass [4].

2.1.2. Electroweak Interaction

In the Standard Model, the electromagnetic interaction, described by quantum electrodynamics (QED), is combined with the weak interaction. Although the forces appear to be very different, they can be unified at an energy scale of about 100 GeV. The electroweak theory can be formulated as a $SU(2) \times U(1)$ gauge symmetry, i. e. it contains 3+1 massless gauge bosons. Linear combinations of these fields can be identified with the observed W^\pm and Z^0 bosons and the photon. In nature, the charged W^\pm bosons and the neutral Z^0 boson have masses of 80 and 91 GeV/c^2 , respectively. Only the photon is massless. This discrepancy can be solved by introducing another boson, the Higgs boson. The so-called Higgs mechanism [5] allows the gauge bosons to acquire mass by “eating up” Goldstone bosons that occur because of the spontaneously broken $SU(2)_H$ symmetry of the Higgs potential. In addition, Yukawa terms of the Higgs boson coupling to fermions lead to fermion mass terms and let the quarks and charged leptons acquire their masses. The Higgs boson is the only particle predicted by the Standard Model that has not yet been observed. The LHC experiments aim to discover - or exclude - it by the end of the year 2012.

2.1.3. Quantum Chromodynamics

Quantum chromodynamics (QCD) describes the strong interaction of quarks and gluons and their bound states, the hadrons. It is the underlying theory for the physics of the QGP. QCD is an $SU(3)$ gauge theory. There arise three *color* charges, commonly labeled “red”, “green” and “blue”. The interaction of color-charged objects is mediated by a gauge boson octet, called *gluons*. The Lagrangian of the

theory, following from promoting the Dirac Lagrangian to be invariant under local $SU(3)$ transformations, reads [6]:

$$\mathcal{L}_{QCD} = \bar{\psi}_i(i\gamma^\mu\partial_\mu - m)\psi_j - gG_\mu^a\bar{\psi}_i\gamma^\mu T_{ij}^a\psi_j - \frac{1}{4}G_{\mu\nu}^a G_a^{\mu\nu}. \quad (2.1)$$

The first term describes the equations of motion of a free fermion given by the Dirac equation, where ψ_j and $\bar{\psi}_i$ denote the incoming and outgoing quarks in the theory. The second term contains the gluon fields $T^a G_\mu^a$. From this term a 2-quark-1-gluon vertex with the coupling strength g arises. The last term describes the pure gluon part. $G_{\mu\nu}^a$ has the form:

$$G_{\mu\nu}^a = \partial_\mu G_\nu^a - \partial_\nu G_\mu^a - gf^{abc}G_\mu^b G_\nu^c \quad (2.2)$$

where the last term arises because of the non-abelian character of $SU(3)$. One can see that apart from the free gluon description given by the terms quadratic in ∂G , mixed terms in ∂G and $gf^{abc}G_\mu^b G_\nu^c$ occur in the Lagrangian. They give rise to a 3-gluon vertex with the coupling strength g . The square of the last term of Equation(2.2) leads to a 4-gluon vertex with coupling strength g^2 . The gluon self-interaction is the reason for many distinguishable features of the strong interaction (see Sections 2.1.5 and 2.2).

2.1.4. Chiral Symmetry

To analyze the low-energy structure of QCD and the corresponding QCD vacuum one can focus on the u and d quarks and neglect heavier quarks. The fermionic QCD Lagrangian for these quarks reads:

$$\mathcal{L}_q = \bar{u}i\gamma^\mu D_\mu u + \bar{d}i\gamma^\mu D_\mu d - m_u\bar{u}u - m_d\bar{d}d \quad (2.3)$$

with the generalized derivative $D_\mu = \partial_\mu + igT_a G_\mu^a$. Since the quark masses are small compared to the typical QCD energy scale of about 200 MeV they can be neglected in the following consideration. One can rewrite the Lagrangian in terms of isospin¹ doublets $q = \begin{pmatrix} u \\ d \end{pmatrix}$ [6]:

$$\mathcal{L}_q = \bar{q}i\gamma^\mu D_\mu q. \quad (2.4)$$

Since QCD is only sensitive to color charges it does not discriminate between the different quark flavors. Under the assumption that the quark masses are equal, the Lagrangian is symmetric under transformations in this two-dimensional flavor space, i.e. the Lagrangian has an isospin symmetry. Since no couplings arise between left and right handed quarks the two parts can transform separately under U_L and U_R :

$$\begin{pmatrix} u \\ d \end{pmatrix}_L \rightarrow U_L \begin{pmatrix} u \\ d \end{pmatrix}_L, \quad \begin{pmatrix} u \\ d \end{pmatrix}_R \rightarrow U_R \begin{pmatrix} u \\ d \end{pmatrix}_R. \quad (2.5)$$

¹Isospin is a quantum number related to the quark flavor symmetry in the first generation. It was introduced on hadron level to categorize mesons and baryons built out of light quarks.

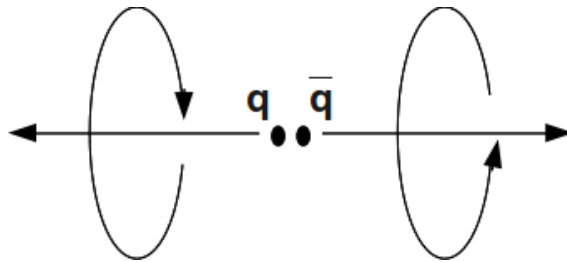


Figure 2.1.: A $q\bar{q}$ pair created out of the vacuum cannot have total momentum or angular momentum. Hence, it has to have a chiral charge and its creation breaks chiral symmetry spontaneously [6].

This means that both the left handed and the right handed part have an isospin symmetry. The Lagrangian has a so-called *chiral symmetry*, it is symmetric under $U(2)_L \times U(2)_R$. This can be decomposed into $SU(2)_L \times SU(2)_R \times U(1)_B \times U(1)_A$ [6]. The $U(1)_B$ symmetry is exact and therefore leads, according to Noether's theorem, to a conserved charge, the baryon number. The $U(1)_A$ part is classically exact but broken by quantum anomalies [6].

In the following, the properties of the remaining symmetry $SU(2)_L \times SU(2)_R$ are discussed. In QCD, quark-antiquark pairs have a strong attraction. In the limit where the quarks are massless the energy needed to form such a pair is infinitely small. This means that the QCD vacuum contains infinitely many of those pairs. Such a pair cannot have a total momentum or angular momentum, which leads to the fact that it has to have a total chiral charge (Figure 2.1) and $\langle 0 | \bar{Q}Q | 0 \rangle = \langle 0 | \bar{Q}_L Q_R + \bar{Q}_R Q_L | 0 \rangle \neq 0$. So the vacuum is not symmetric under $SU(2)_L \times SU(2)_R$, it mixes helicities. The creation of real $q\bar{q}$ pairs implies a spontaneous breaking of the chiral symmetry.

The corresponding terms $\bar{q}_L q_R$ are similar to mass terms. These can be understood as effective masses for the considered quarks that arise due to the propagation through the $q\bar{q}$ pairs in the vacuum, caused by the spontaneous symmetry breaking (SSB) of chiral symmetry. These effective masses are of the order of $300 \text{ MeV}/c^2$, much larger than the bare quark masses. This has an important implication on the isospin symmetry of QCD: as long as the considered quark masses are small compared to the $300 \text{ MeV}/c^2$, which the quarks acquire due to SSB of chiral symmetry, they behave as if they were degenerated in mass, i.e. as if they had the same mass.

Therefore, the isospin symmetry does not result from a fundamental relation of u and d quarks but only from the fact that their bare masses are small compared to their *effective* mass of $300 \text{ MeV}/c^2$. For this reason, the isospin symmetry works well even for hadrons containing a much heavier s quark. The s quark is much lighter than $300 \text{ MeV}/c^2$ and therefore it can be treated as having a similar mass than the

u and d quark. The generalization to a $SU(3)$ isospin symmetry is, according to this argument, to a certain extent justified.

Nevertheless, the small differences in the bare masses break the isospin symmetry explicitly. Chiral symmetry is also explicitly broken, since the bare quark masses are not zero. Both symmetries are only approximate. The Goldstone theorem states that each spontaneously broken symmetry is accompanied by massless Goldstone bosons. Since the chiral symmetry is only approximate, the Goldstone bosons related to its spontaneous breaking are not completely massless. The lightest mesons, the pions, which will be the particles of interest for the HBT analysis presented in this thesis can be identified as the Goldstone bosons connected to the SSB of chiral symmetry.

2.1.5. Confinement and Asymptotic Freedom

Since QCD is a non-abelian theory, force carriers are themselves interacting and color-charged, each gluon carries one color and one anticolor charge. This leads to several interesting phenomena that are specific for QCD.

In QED, the polarization of virtual electron-positron pairs in the vacuum leads to charge screening: the electromagnetic field caused by a test charge is weakened by the vacuum polarization. Hence, the effective charge is smaller at large distances and larger at small distances. This can be formulated in a running coupling strength α_{em} depending on the interaction distance. However, its variation is small from the Planck scale ($1.616 \cdot 10^{-35}$ m) to infinity [6].

In QCD the same effect occurs. The $q\bar{q}$ pairs that fill up the vacuum screen a color charge reducing the effective charge at large distances. In addition, virtual gluon pairs can be created out of the vacuum as well, which are also color-charged. The gluons in the loop can occur in different modes. Only loops where both gluons are in a transverse mode weaken the charge, in other cases the field is augmented and its color-charge is changed. The behavior of the coupling constant α_s at different energy scales is given by [6]:

$$\alpha_s(Q) = \frac{2\pi}{(11 - \frac{2}{3}n_f) \ln(Q/\Lambda)}, \quad (2.6)$$

where Q denotes the momentum transfer through the interaction and Λ is the momentum scale at which α_s becomes of the order of one. Λ is experimentally found to be around $200 \text{ MeV}/c$, the inverse of the size of a hadron. The term $(11 - \frac{2}{3}n_f)$ comes from the calculation of the possible loop diagrams. $\frac{2}{3}n_f$ corresponds to the $q\bar{q}$ loops with n_f being the number of considered quark flavors, and the factor 11 arises from the gluon loops. The experimentally determined Q dependence of α_s is shown in Figure 2.2.

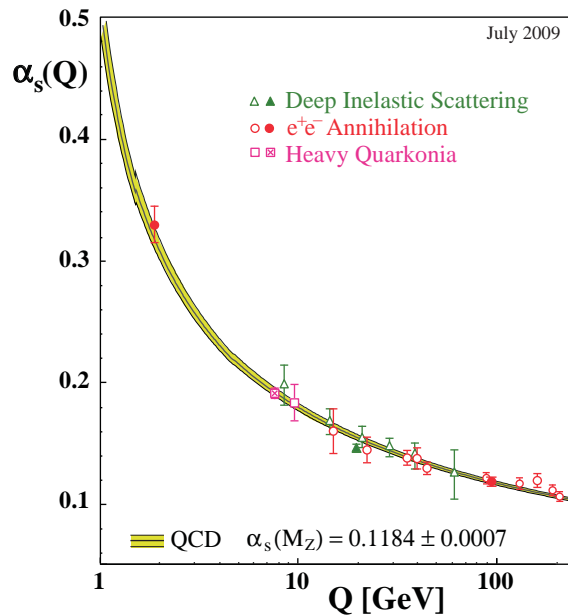


Figure 2.2.: Summary of measurements of α_s as a function of the respective energy scale Q . The curves are predictions from QCD. (Figure from [7])

In contrast to QED, the variation in α_s from Planck scale to infinity is quite large. It follows from the $1/\ln(Q/\Lambda)$ dependence of α_s that the strong coupling becomes infinitely weak at high momentum transfer Q , i.e. at high energies or small distances. This fact allows to apply perturbation theory down to energy scales of $Q \approx 1 \text{ GeV}/c$ and implies that quarks and gluons experience asymptotic freedom at high energies. On the other hand, the coupling increases for low momentum transfer Q , i.e. low energies or large distances. The limit of Equation (2.6) is given by $Q = \Lambda$, i.e. when there is enough energy to produce a light meson or when the distance gets larger than the hadron size. This leads to *confinement*, meaning that no color-charged objects can exist freely.

This can be portrayed as followed: when two color-charged objects are separated, a flux tube containing all field lines builds up. This leads to an effective potential that rises linearly with the distance of the charges. This flux tube or color string fragments as soon as it contains more energy than the $q\bar{q}$ pair production energy, and hadrons are produced. Thus, only color-neutral objects like mesons and baryons are observed in nature, free quarks cannot be seen. Color-neutral gluon bound states, called glueballs, are theoretically also possible, but have not been observed experimentally.

2.2. The Quark-Gluon Plasma

From the above discussion of QCD, two possible transitions are expected to occur in nature: the restoration of chiral symmetry at high energies and a transition from confinement to deconfinement going from low to high energies. The chiral symmetry is restored as soon as the energy is high enough, or rather α_s small enough, such that the creation of $q\bar{q}$ pairs from the vacuum requires a finite amount of energy. Therefore, the order parameter of this transition is the vacuum expectation value of $q\bar{q}$ pairs, $\langle 0|\bar{q}q|0\rangle$. It is zero above the transition temperature and non-zero below.

In the confined phase a discrete $\mathbb{Z}(3)$ symmetry coming from exchanging the colors exists, since this does not change the overall charge of color-singlet objects. It is clearly broken if quarks and gluons are deconfined. The order parameter of this transition is the Polyakov loop: it describes the path of a virtual $q\bar{q}$ pair in space-time. If the quarks are not confined, the corresponding action is proportional to the circumference of the loop; if they are confined, it is proportional to the area. Mesons can occur in the confined case, since there is a “loop inside the loop” going in the other direction, such that area between those loops and the corresponding action is small.

A priori, there is no reason why these two transitions should be connected. But confinement occurs at low energy scales compared to the quark masses and the SSB of chiral symmetry leads to the fact that quarks have large effective masses. Hence, confinement can persist at energy scales that are larger than the quark bare masses thanks to the broken chiral symmetry. It is then related to chiral symmetry and breaks down at the same energy at which chiral symmetry is restored.

The deconfined phase of quarks and gluons is called quark-gluon plasma (QGP). The term *plasma* refers to a system in which charges are screened by mobile charge-carriers. Indeed, deconfined quarks and gluons screen long-range interactions and only short-range interactions remain. α_s is small at small distances, hence, only small interaction between quarks and gluons are expected, i.e. they are quasi-free. To distinguish the regimes of confinement and deconfinement, a critical temperature T_c at which the transition occurs can be estimated. For different baryochemical potentials the value for the critical temperature changes. A QCD phase diagram can be constructed displaying the phase boundary in the plane of temperature and baryochemical potential (Figure 2.3).

An analytic calculation of the critical temperature is non-trivial, since perturbation theory is only applicable at energies well above the critical temperature where α_s is small. A simple approach to estimate T_c is the *MIT bag model* [9]. In this model, the quarks and gluons are taken to be confined in a bag containing a perturbative vacuum. The bag is surrounded by a realistic QCD vacuum containing $q\bar{q}$ condensates. A bag pressure is defined as the energy difference between inside and

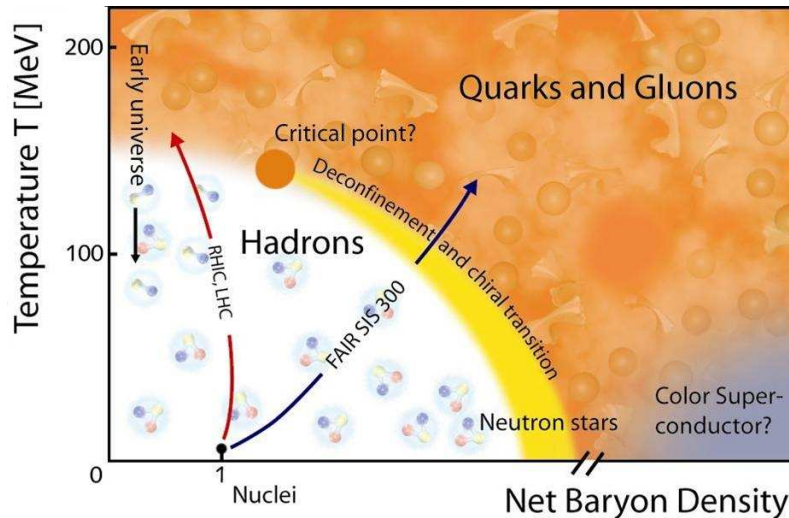


Figure 2.3.: A sketch of the QCD phase diagram [8].

outside the bag. As soon as the quarks and gluons have an energy large enough to overcome the bag pressure they are no longer bound but deconfined. The critical temperature calculated from this approach is $T_c = 146$ MeV for a baryochemical potential $\mu_B = 0$ [9]. A very small baryochemical potential is expected for high-energy heavy-ion collisions.

Another approach to non-perturbative QCD is to perform the calculation analytically for one distinct point in space-time. If this is done for many points, i.e. on each point of a space-time lattice, quantities like the expectation value of the $q\bar{q}$ condensate or the Polyakov loop, from which the critical temperature can be estimated, are extracted. The results are between $T_c = 150$ MeV and 190 MeV for a vanishing baryochemical potential [10]. Such lattice-QCD calculations are very demanding in terms of computing power.

If the nuclei in a heavy-ion collision do not collide head-on, not all nucleons participate in the collision. The nucleons can be separated into *spectator nucleons* that do not interact significantly and nucleons in the *fireball region* that actually collide. The centrality of the collision, i.e. the value of the impact parameter, is an important characteristic of the event. Experimentally, it is estimated by the multiplicity of measured particles or the energy deposition in a calorimeter and then, by a comparison to a Glauber model fit [11], quoted in percentages of the total nuclear cross-section.

When the nuclei traverse each other, hard and very energetic parton-parton interactions may happen, producing high-energy objects. Shortly after, the quarks and gluons of the compressed nucleons form the QGP. After some time the medium is ex-

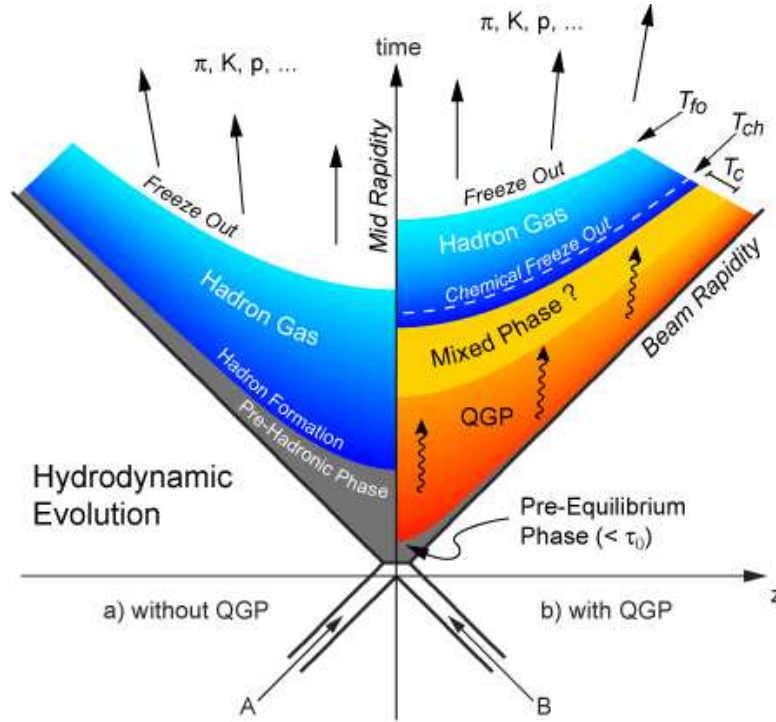


Figure 2.4.: Time evolution in a heavy-ion collision with (right) and without (left) the formation of a QGP. [12].

pected to reach equilibrium. From this point on the QGP evolution can be described theoretically by hydrodynamics. It can be treated as an almost perfect fluid, since only weak interactions occur at small scales. Hydrodynamic models can predict the expected energy density and pressure and the resulting evolution of the QGP region under the assumption of initial conditions and an equation of state. The expansion of the QGP leads to cooling and a decrease of pressure. Finally, the QGP freezes out into hadrons, which can be measured in the detector. The transition from QGP to observable particles has several steps. The first is the so-called *chemical freeze-out*, where quarks and gluons are bound to hadrons and inelastic interactions do no longer occur. At this stage, the particle composition is fixed. As long as the particles interact elastically, the momenta can still change, but from some point on the particles are propagating practically without any interaction. This is called *kinetic* or *thermal freeze-out*. A sketch of the time-evolution in a heavy-ion collision is shown in Figure 2.4.

All experimental studies of the QGP are indirect, as the observables can only rely on the measured reaction products after the freeze-out phase. Nevertheless, there are several ways to access QGP properties experimentally:

- **Particle Yields:** The particle yield as a function of transverse momentum

in heavy-ion collisions can be studied in comparison to pp collisions. The pp results have to be scaled to the number of binary nucleus-nucleus collisions to allow a direct comparison. The scaled ratio of the spectra measured in heavy-ion and pp collisions is called nuclear modification factor, R_{AA} [13]. It provides an insight into the particle production mechanisms, as well as the in-medium energy-loss. The ratio can also be measured separately for different particle species to obtain information on the mass dependence of the energy-loss mechanisms. Furthermore, the particle yields can be compared in dependence on the particle emission angles relative to a high- p_T particle to study the modification of the particle yield accompanying this reference particle (I_{AA}) [14]. Instead of a pp reference, peripheral events, in which no QGP is expected to form, can be used to measure the same observables in a different way.

- **Heavy Quarks and Quarkonia:** Heavy quarks are only created in the early phase of the collision, since their high mass requires a hard scattering process. They are good probes for the in-medium energy-loss mechanisms since they exist through the whole evolution of the QGP. Bound states of heavy $q\bar{q}$ are “melted” at a certain temperature depending on their binding energy, similar to the ionization of a hydrogen atom. Observing the melting of several quarkonia states can serve as a thermometer. At LHC energies, recreation of quarkonia and even an enhancement, i.e. a rising R_{AA} is predicted, the yields are predicted by statistical hadronization (Figure 2.5 shows a prediction and comparison to RHIC² data) [15].
- **Leptons and Photons:** Directly produced leptons and photons are interesting probes, since they are not expected to interact with the QGP. They provide a valuable reference to other observables, which reflect the influence of the medium. In addition, photons coming from thermal radiation can be used to estimate the temperature of the QGP. For this purpose, they need to be carefully separated from photons from other sources, which is experimentally challenging.
- **Jets and Hard Probes:** Similar to heavy quarks, jets are high- p_T objects produced in an initial hard interaction. A jet is a stream of many high-momentum particles that are found within a predefined cone. These are the fragmentation products of a hard scattered parton. A back-to-back parton scattering leads to an event with two jets. When partons radiate gluons in the early state, many-jet events occur. Studying jets can provide information on the in-medium parton energy loss, as well as on the fragmentation pattern in the presence of a QGP. For most di-jets that are produced back-to-back on the

²RHIC, the relativistic heavy-ion collider, is an accelerator located at the Brookhaven National Laboratory (BNL). It delivers heavy-ion collisions at a center-of-mass energy of up to 200 GeV per nucleon pair and is herewith the second-highest-energy heavy-ion collider.

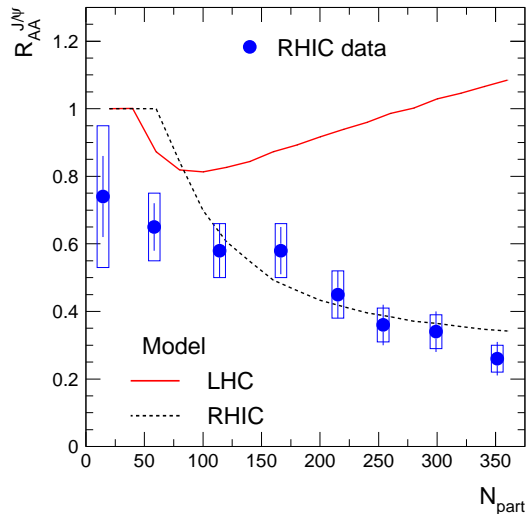


Figure 2.5.: Calculation from the Statistical Hadronization Model compared to RHIC data and predictions for LHC energies (Figure from [15]).

edge of the fireball, one of the two jets has a longer path length through the medium. It will lose energy, leading to a large momentum difference between the two back-to-back jets coming from partons with the same momentum. The phenomenon of a jet being modified by the medium in such a way is called *jet quenching*.

- **Flow and Particle Spectra:** Important information is obtained by examining the collective behavior of the particles. The bulk properties of low-momentum particles can be especially interesting for hydrodynamic model comparisons. A central observable is the particle flow. It probes anisotropies in the azimuthal particle distribution that have their origin in the geometry of the emission region and in density fluctuations. The flow is dependent on the energy density, the pressure gradient and the viscosity of the created medium and can therefore distinguish between different hydrodynamic scenarios.

Information on the fireball expansion can also be extracted from the azimuthally-integrated momentum distributions of different particle species. The functional form of the spectra expected from a Blast-Wave expansion (shock-wave scenario in a fluid) of the QGP is fitted to the data to extract temperature and radial expansion velocity.

- **Two-Particle Correlations:** By studying Bose–Einstein correlation of identical bosons the space-time characteristics of the emitting fireball region can be accessed. This technique is the central topic of this thesis and explained in detail in the following chapter.

3. The ALICE Experiment

ALICE, *A Large Ion Collider Experiment*, is one of the large experiments at the *Large Hadron Collider* (LHC) at CERN. It is a detector dedicated to the study of the hot and dense matter created in high-energy heavy-ion collisions. It is built by a collaboration of more than 1000 members from about 30 countries. The experiment measures $16 \times 16 \times 26 \text{ m}^3$ and has a weight of about 10000 t [17]. Many specialized sub-detector systems assure excellent tracking quality and particle identification over a large momentum range even in the high-multiplicity environment observed in central Pb–Pb collisions at the LHC.

In this Chapter, the LHC is briefly introduced, then, the requirements for a detector studying heavy-ion collisions and the realization in ALICE are outlined. ALICE and its sub-detectors are discussed and the data flow is described.

3.1. The Large Hadron Collider (LHC)

The Large Hadron Collider (LHC) is a synchrotron with a circumference of 27 km. Two beams circulate in different directions in separate beam pipes that are surrounded by superconducting magnets bending the beam trajectories on the orbit (Figure 3.1). It is built in the tunnel of the *Large Electron-Positron* (LEP) Collider which was operating from 1989 to 2000. The largest energy to which particles can be accelerated with the LHC is $\sqrt{s} = 14 \text{ TeV}$ for protons and $\sqrt{s_{NN}} = 5.5 \text{ TeV}$ for lead ions. There are 1232 superconducting dipoles operating at a temperature of 1.9 K, which is colder than the average temperature of the universe. They provide a magnetic field of up to 8 T (Figure 3.2). The LHC is designed for a luminosity of up to $10^{34} \text{ cm}^{-2}\text{s}^{-1}$ for proton collisions and $10^{27} \text{ cm}^{-2}\text{s}^{-1}$ for Pb–Pb collisions [20]. Four big experiments record and analyze the collisions. Besides ALICE, these are ATLAS (*A Toroidal LHC ApparatuS*) and CMS (*Compact Muon Spectrometer*), multi-purpose detectors focusing on Higgs production processes and physics beyond the Standard Model, as well as LHCb (*The LHC beauty experiment*) which studies matter-antimatter asymmetry in b-quark systems. Furthermore, the smaller experiments TOTEM (*Total Cross Section, Elastic Scattering and Diffraction Dissociation at the LHC*), LHCf (*Large Hadron Collider forward*), and MoEDAL (*Monopole and Exotics Detector at the LHC*) complete the physics program.

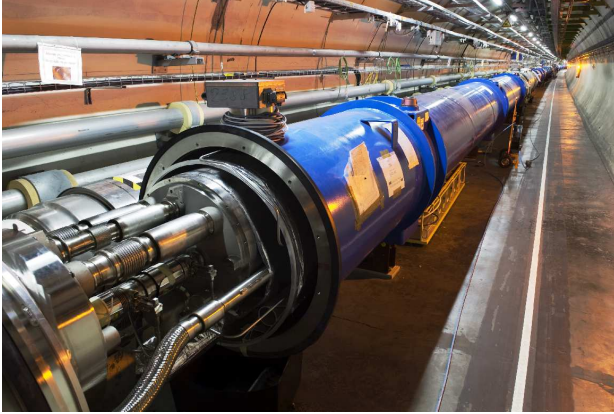


Figure 3.1.: View inside the LHC tunnel. The connection between two dipole magnets is visible [18].

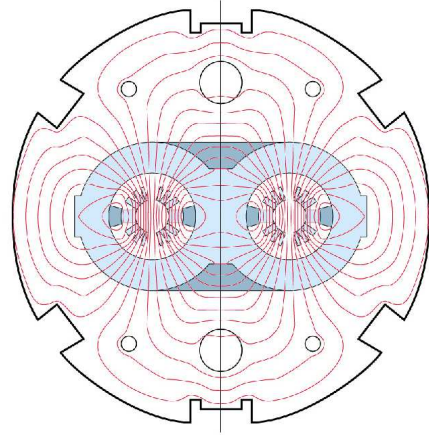


Figure 3.2.: Schematic cross-section of an LHC dipole with the two beam pipes. The magnetic field lines are indicated [19].

3.2. Challenges for ALICE as a Heavy-Ion Detector

The main focus of ALICE is the study of quantum chromodynamics (QCD), describing the interaction of quarks and gluons, the constituents of hadrons. In particular, the properties of strongly-interacting matter at extremely high temperatures and energy densities, where a quark-gluon Plasma (QGP) can be formed, are studied with ALICE. In addition, the analysis of pp collisions at LHC energies provides valuable references for the Pb–Pb observables and leads to further insights in special topics where ALICE is complementary to the other LHC experiments, such as minimum bias measurements, observables requiring an excellent particle identification, and the physics of low- p_T particles and diffractive events.

One of the main constraints of the detector design is to ensure good-quality tracking and particle identification (PID) even when the event multiplicities are up to 3 orders of magnitude higher than in pp collisions. Figure 3.3 shows a typical event display of a heavy-ion collision. The design was optimized for multiplicities of $\langle dN_{ch}/d\eta \rangle = 4000$ but tested up to twice the value. Experimentally, the multiplicity in central Pb–Pb collisions at $\sqrt{s_{NN}} = 2.76$ TeV is found to be $\langle dN_{ch}/d\eta \rangle = 1601 \pm 60$ (sys.) [22].

A tracking strategy using 3D hit information and many hit points per track in a moderate magnetic field ensures good-quality reconstruction even in high-multiplicity events. To allow tracking down to very low momenta as it is needed for resonance or heavy-flavor analyses, the material budget needs to be very low to reduce absorption and distortion from multiple scatterings with the detector material. Large radii of the tracking devices lead to a good resolution for high- p_T tracks. By combining the information from different tracking detectors the covered momentum range

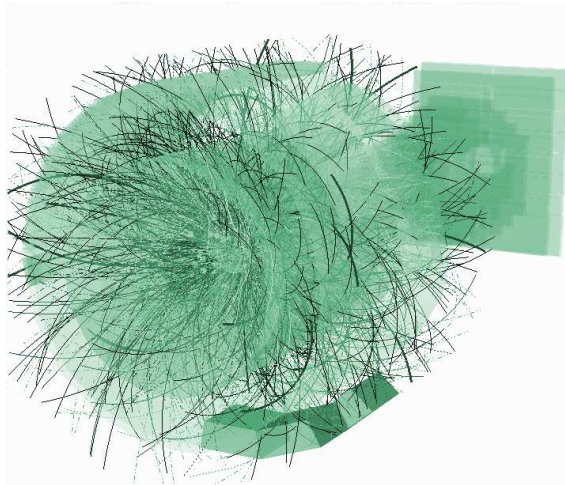


Figure 3.3.: Event-display of one of the first Pb–Pb collision at $\sqrt{s_{NN}} = 2.76$ TeV observed with ALICE during the 2011 LHC heavy-ion run [21].

reaches from tens of MeV/ c to a few hundred GeV/ c required for jet and high- p_T measurements.

For particle identification only the combination of many approaches can be fully efficient. The specific ionization energy-loss, a time-of-flight measurement, transition and Cherenkov radiation, an electromagnetic calorimeter, the muon system and the reconstruction of decay topologies is combined to provide information on the particle species.

3.3. ALICE Sub-detectors

ALICE consists of a central barrel covering $|\eta| < 0.9$ enclosed in a solenoid that is reused from the L3 experiment, which was previously installed in the same experimental area. The provided magnetic field is 0.5 T. The central part is optimized for the detection of hadrons, electrons and photons. Muons are detected in a forward muon spectrometer, which will not be further discussed here. In addition, forward and trigger detectors complete the design (Figure 3.4). In the following, the main subsystems are introduced, starting from the interaction point and going outwards.

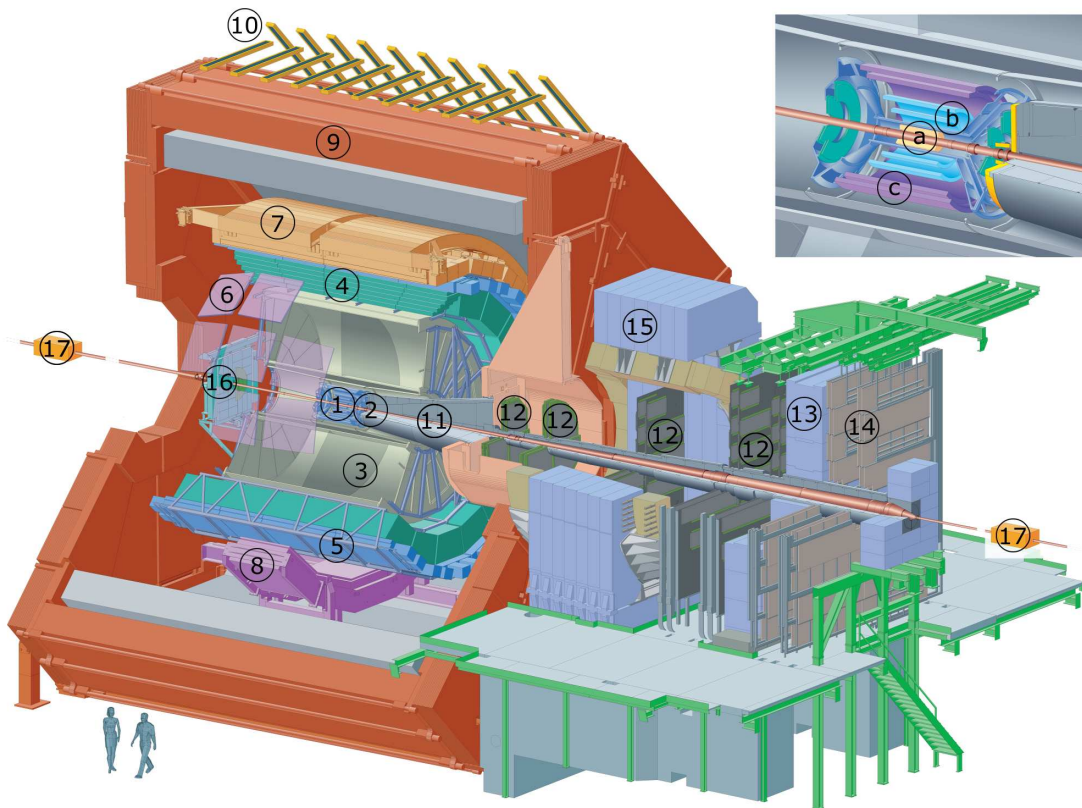


Figure 3.4.: The setup of the ALICE detector [23]: (1) ITS; (a) ITS SPD Pixel; (b) ITS SDD Drift; (c) ITS SSD Strip; (2) FMD, T0, V0; (3) TPC; (4) TRD; (5) TOF; (6) HMPID; (7) EMCAL; (8) PHOS; (9) L3 Magnet; (10) ACORDE; (11) Absorber; (12) Muon Tracking; (13) Muon Wall; (14) Muon Trigger; (15) Dipole; (16) PMD; (17) ZDC.

3.3.1. The Inner Tracking System (ITS)

The ITS is the closest detector to the interaction point. It is a silicon detector, consisting of three different subsystems: the Silicon Pixel Detector (SPD), the Silicon Drift Detector (SDD), and the Silicon Strip Detector (SSD). In total, it is 98 cm long and spans from a radius of 4 cm to 43 cm. The excellent spatial resolution is used for the reconstruction of primary and secondary vertices with a spatial resolution of up to $100\ \mu\text{m}$ in the transverse direction. It contributes to the global tracking as well as to PID via a dE/dx measurement in the SDD and SSD. Standalone tracking can be performed to detect very low- p_T particles down to $35\ \text{MeV}/c$ that do not reach the other detectors. In addition, the number of clusters in the SPD can serve as a multiplicity and centrality estimator. The SPD is read out within $6\ \mu\text{s}$ [17]. It can be also used as a trigger. Some SPD modules are not active, which leads to an acceptance that is not uniform in azimuth. This is problematic for some analyses, for example for the event plane estimation and discussed further in Chapter 6.



Figure 3.5.: View inside the ALICE solenoid. The position of the central barrel detectors, the ITS, the TPC and the TRD, are visible [24].

3.3.2. The Time-Projection Chamber (TPC)

The TPC is the main tracking device in ALICE. With an active volume of 90 m^3 , a length of 5 m, an inner radius of 80 cm, and an outer radius of 250 cm it is the largest TPC ever built (see Figure 3.5). It has 18 trapezoidal sectors with multi-wire proportional chambers for read-out at both ends. The large radius of the TPC as well as its fine granularity ensures a good tracking. Particles with p_T from $150\text{ MeV}/c$ up to $100\text{ GeV}/c$ can be measured. The very precise measurement of the specific energy-loss through ionization (dE/dx) (energy resolution of 5%) [17] together with the momentum measurement is used for PID. In the global tracking procedure the TPC information is combined with the information from the ITS and other detectors to reconstruct so-called global tracks. Using only TPC information for reconstruction (“TPC-only tracks”) can ensure a uniform acceptance in azimuth but the momentum resolution might be not as good as for global tracks. Since the finite drift time of the charged ions of $90\text{ }\mu\text{s}$ leads to a relatively slow read-out compared to other detectors, the TPC limits the rate of events that can be read out and recorded.

3.3.3. The Transition-Radiation Detector (TRD)

To distinguish between electrons and pions especially at high momenta, which is difficult with a dE/dx measurement, the different amount of transition radiation of these particle species can be used. Transition radiation occurs, when a charged particle traverses the boundary between two materials with different dielectric constants. Since the amount of transition radiation is proportional to $\gamma = v/c$, electrons and pions can be distinguished well. This is important for heavy-flavor physics since an electron is often part of the decay chain and pions are abundant in heavy-ion

collisions. The TRD provides such a measurement and contributes to the tracking. It consists out of 18 sectors with 6 detector layers each. Its signal can also be used as a trigger for high-energetic electrons. To activate the electronics readout it needs a pretrigger signal that can come from TOF, V0 or T0 (these detectors are introduced in the two following sub-sections). For the 2011 runs, 10 out of 18 modules are in operation.

3.3.4. The Time-Of-Flight Detector (TOF)

The TOF detector provides a complementary measurement to dE/dx for particle identification. It is located at a radius of 3.8 m from the interaction point. The system of multi-gap resistive plate chambers achieves an overall time resolution of 100 ps [17]. The measurement of the time of flight of particles can distinguish between protons, kaons and pions especially at intermediate p_T of 0.5-3.0 GeV/ c for pions and kaons and 0.5-6.0 GeV/ c for protons [17].

3.3.5. Specialized Detectors

A set of special purpose detectors are installed in the central barrel each covering a smaller range in azimuth than the main detectors described above:

- **EMCal:** The Electromagnetic Calorimeter (EMCal) is a lead-scintillator sampling calorimeter. It can detect direct photons, neutral pions, and η mesons via their decay photons. It can also be included in the triggering.
- **PHOS:** The Photon Spectrometer (PHOS) consists out of scintillating crystals and lead-tungstate crystal elements. Its purpose is similar to that of the EMCal, but it has a higher granularity and energy resolution (up to 4%) than the EMCal and has a smaller coverage. It can also be included in the triggering.
- **HMPID:** The High Multiplicity Particle Identification detector (HMPID) provides precise information for the PID of high momentum hadrons. It is a ring imaging Cherenkov detector.
- **ACORDE:** The Alice Cosmic Ray Detector (ACORDE) consists of 60 large scintillators that are mounted on top of the magnet. It serves as a cosmic ray trigger which is useful in the detector calibration and alignment process and it can measure single atmospheric muons in combination with TPC, TRD and TOF.

3.3.6. Forward Detectors

- **PMD**: The Photon Multiplicity Detector (PMD) is built out of two gas proportional chambers and a lead converter in between. It measures photon multiplicities at pseudorapidities of $2.3 < \eta < 3.7$.
- **FMD**: The Forward Multiplicity Detector (FMD) uses silicon strips to measure the charged-particle multiplicity at $-3.4 < \eta < -1.7$ and $1.7 < \eta < 5.0$.
- **V0**: The V0 detector is used as a minimum-bias trigger and to reject events that are not supposed to be used in a physics analysis, like reactions between beam and gas. This is performed by the measurement of the interaction time with a good time resolution of 1 ns. Its two scintillator counters are placed at $2.8 < \eta < 5.1$ and $-3.7 < \eta < -1.7$. Its signals are used as a measure of the centrality of the event.
- **T0**: Similar to the V0 detector, the T0 detector measures the exact interaction time with a precision of 25 ps. It provides the reference time for TOF and can be used to reject beam-gas events by estimating the vertex position.
- **ZDC**: The Zero Degree Calorimeter (ZDC) provides a measurement of the impact parameter of the collision by measuring the number of spectator nucleons. It consists of one electromagnetic calorimeter and one neutron and one proton calorimeter on each side of the interaction point at a distance of 116 m.

3.4. Data Acquisition and Event Reconstruction

3.4.1. Data Acquisition (DAQ)

In ALICE, *online* refers to processes that have to be done in real time, i.e. directly when the event is happening in contrast to *offline* activities that are independent of the actual time when the event happened. The task of the data acquisition (DAQ) system is to collect all the information on a given event from the several sub-detectors and combine them (“event building”). In addition, information on the data-taking conditions have to be extracted. The system has to be able to buffer events and export the information to a permanent storage (CASTOR). The ALICE DAQ system is able to handle a data rate of up to 1.25 GB/s [17].

The decision whether an event is interesting enough to read out all the sub-detectors and write it to storage is made by a two-layer trigger system. In the first step, a hardware trigger (Central Trigger Processor (CTP)), directly using the detector signals provides a fast decision on 3 levels. The decision time on the highest level (L2) is comparable to the TPC drift time. Additionally, the CTP can be used

to avoid problems due to pile-up can be by allowing only a certain number of high-multiplicity events in a certain time-window.

In the second step, the high-level trigger (HLT), a farm of about 1000 computers processing the data in parallel, performs an online event reconstruction per sub-detector and does a fast analysis to allow for more sophisticated triggers as for example on high-energy jets or muon pairs.

3.4.2. Event Simulation and Reconstruction

As soon as the so-called raw data produced by the DAQ system is stored, the offline reconstruction can start. The average amount of data produced by ALICE in a year is estimated to be 10-15 PB. The raw data of one central Pb–Pb event is about 14 MB, 10^8 events per year are expected [17]. The output of the reconstruction has a size of about 3 MB. The reconstruction and analysis of such an enormous amount of data requires computing resources that not even an organization like CERN can provide. The GRID concept of combining several computing resources in different locations collaboration-wide is realized in ALICE. The ALICE GRID has at present 53 centers in several countries [25]. The so-called GRID middle-ware used in ALICE is AliEn (ALICE Grid Environment) providing a user interface and an integration in ROOT [26].

The ALICE-specific framework used for reconstruction and analysis as well as for the simulation of Monte-Carlo events is called AliRoot [27]. It is based on ROOT and mainly written in C++.

The following steps are performed when simulating an event:

- **Event Generation:** a collision is simulated by an event generator interfaced with AliRoot, for example Pythia [28] or Phojet [29] for pp events and HIJING [30] or Therminator [31] for Pb–Pb events. It produces a kinematics tree containing the full particle information.
- **Transport:** the generated particles have to be propagated through the modeled ALICE detector. This is done by detector description and simulation tools like Geant3 [32], Geant4 [33], or Fluka [34]. Hereby, they can interact with the detector material producing secondary particles and with the active detector region causing signals, called hits. The detector response to these hits is simulated, resulting in so-called digits, i.e. ADC counts.

At this point, the simulated detector response and the actual signals measured in a collision are comparable. Hence, all the following steps are identical for simulated and real data.

- **Cluster finding:** detector signals that are close in space and/or time can be combined to clusters to reduce random noise. This is done for each sub-detector individually.
- **Tracking:** the clusters in all sub-detectors are combined to tracks beginning with the TPC using a Kalman-filter procedure [35]. From the extracted track curvature and the energy-loss the particle momentum and identity is extracted.
- **Vertex reconstruction:** from the tracks or from several track segments the primary vertex and possible secondary vertices are reconstructed.

The information extracted during reconstruction is stored as an Event Summary Data (ESD) object. Afterwards, an Analysis Object Data (AOD) can be created containing only analysis-specific information.

4. Hanbury Brown–Twiss (HBT) Interferometry

4.1. Introduction

In order to gain insight into the detailed properties of the QGP created in high-energy heavy-ion collisions it is important to address the space-time characteristics of the emitting source. The small size and short duration of the reaction prohibit a direct measurement of times or positions. However, experimentally particle correlations provide a direct link to the size and the lifetime of the source.

The correlation of two interfering particles emitted from a chaotic source was first studied by Hanbury-Brown and Twiss in 1956 [36]. They measured the correlation of photons emitted from a star to determine the size of the emission region. Independently, this concept was applied in nuclear collisions, and correlations of identical pions were found to be sensitive to the size of the emitting source that is created (Goldhaber, Goldhaber, Lee, Pais [37]). Nowadays, measurements of particle correlations to extract space-time characteristics of the source are also called Femtoscopy, referring to the femtometer length scale of the studied systems. The term also includes measurements of the correlation of non-identical particles via strong or Coulomb interaction. It has become a precision tool in heavy-ion experiments and is also theoretically well understood.

In this Chapter, the theoretical background of HBT interferometry is presented. The construction of the correlation function from particle spectra is shown as well as the Gaussian parametrization. Afterwards, the experimental technique is outlined.

4.2. Theoretical Formalism

When a phase-space volume smaller than $\Delta p \Delta x \approx \hbar$ is considered, a chaotic system of identical non-interacting particles exhibits quantum fluctuations following Bose–Einstein (or Fermi–Dirac) statistics. The study of the quantum correlation of identical particles emitted in an heavy-ion collision can be used to extract information on the space-time properties of the emission region. To study the correlation

in detail a two-particle correlation function can be constructed as the ratio of the two-particle and single-particle spectra. In the following, higher-order symmetrization is neglected. This means, a quantum-statistical correlation is only assumed and calculated between a pair of particles, not between all of them. The distortion of the correlation function due to this approximation was found to be only important when the phase space density is close to unity as it can be the case in collisions of small systems at low energies [38].

4.2.1. From Particle Spectra to the Correlation Function

The emission of free and uncorrelated particles can be described statistically and quantum-mechanically, leading to single-particle spectra that are defined as:

$$\mathcal{P}_1(\mathbf{p}) = E \frac{dN}{d^3p} = E \langle \hat{a}_p^\dagger \hat{a}_p \rangle, \quad (4.1)$$

where E is the particle energy, N the expected number of particles, p indicates the four-momentum and \mathbf{p} the three-momentum of the particle. In the following, bold characters always indicate three-vectors. The expression is formulated in terms of creation and annihilation operators \hat{a}_p^\dagger and \hat{a}_p for on-shell particles with momenta p . The brackets denote an average over the source ensemble.

Correspondingly, the two-particle spectra can be generally defined as:

$$\mathcal{P}_2(\mathbf{p}_1, \mathbf{p}_2) = E_1 E_2 \frac{dN}{d^3p_1 d^3p_2} = E_1 E_2 \langle \hat{a}_{p_1}^\dagger \hat{a}_{p_2}^\dagger \hat{a}_{p_2} \hat{a}_{p_1} \rangle, \quad (4.2)$$

for two particles with energies E_1 and E_2 and momenta p_1 and p_2 , respectively. The two-particle correlation function is defined as the ratio of the two-particle and single-particle spectra:

$$C(\mathbf{p}_1, \mathbf{p}_2) = \mathcal{N} \frac{\mathcal{P}_2(\mathbf{p}_1, \mathbf{p}_2)}{\mathcal{P}_1(\mathbf{p}_1) \mathcal{P}_1(\mathbf{p}_2)}, \quad (4.3)$$

where \mathcal{N} is a normalization factor. This expression can be generally used for all two-particle correlation studies. The following arguments will be made for Bose–Einstein correlated pairs of identical pions. The relevant variables used to describe a pion pair are the pair momentum $k = (p_1 + p_2)/2$, the pair momentum difference $q = p_1 - p_2$ and the space-time emission distance $r = x_1 - x_2$.

In order to simplify the description of the pion emission, an emission function $S(x, p)$ is introduced, giving the probability for the creation of a free particle with momentum p at the space-time point x [39]:

$$S(x, p) = \int \frac{d^4 y}{2(2\pi)^3} e^{-py} \left\langle J^* \left(x + \frac{y}{2} \right) J \left(x - \frac{y}{2} \right) \right\rangle, \quad (4.4)$$

which is a Wigner function, defined in terms of the classical source amplitude $J(x)$ and its complex conjugate $J^*(x)$, where y indicates a spatial integration parameter. In terms of this emission function the single-particle spectrum is given by:

$$E \frac{dN}{d^3 p} = \int d^4 x S(x, p). \quad (4.5)$$

This semi-classical approach replacing quantum-mechanical particle emission probabilities with classical source functions means that the applicability of this formulation is limited by quantum uncertainty. The influence on the correlation function can be checked by evaluating the source function in terms of wave packets with a finite width in space-time. A spatial broadening of the pair emission distribution is observed which is negligible for large sources well above 1 fm [40].

If an initially uncorrelated emission is assumed and all kinds of interactions are neglected but the effect from symmetrization is considered, the two-particle emission function can be formulated in terms of single-particle emission functions, where the emission points are weighted with the symmetrized wave function. A factorization of the wave function of the pion pair can be factorized into the contributions from Coulomb and Strong interaction and a part which only contains the symmetrization of the free wave function. In the following considerations the former are neglected and only the latter are considered. Methods to account for the contributions from Coulomb and Strong interaction are discussed later. The two-pion wave function then reads:

$$\phi(x_1, x_2, p_1, p_2) = \frac{1}{\sqrt{2}} [\phi(x_1, p_1) \phi(x_2, p_2) + \phi(x_1, p_2) \phi(x_2, p_1)]. \quad (4.6)$$

With a plane wave assumption, the square is given by:

$$|\phi(x_1, x_2, p_1, p_2)|^2 = \left| \frac{1}{\sqrt{2}} (e^{ip_1 x_1} e^{ip_2 x_2} + e^{ip_2 x_1} e^{ip_1 x_2}) \right|^2 = 1 + \cos(q \cdot r). \quad (4.7)$$

Using Equations (4.2), (4.5), and (4.7), the two-particle emission function can be formulated in the following way:

$$\begin{aligned} \mathcal{P}_2(\mathbf{p}_1, \mathbf{p}_2) &= E_1 E_2 \frac{dN}{d^3 p_1 d^3 p_2} \\ &\approx \int d^4 x_1 d^4 x_2 S(x_1, p_1) S(x_2, p_2) |\phi(p_1, p_2, x_1, x_2)|^2. \end{aligned} \quad (4.8)$$

In the last expression of Equation (4.9) it is assumed that the emission function has a sufficiently smooth momentum dependence such that the function evaluated at the average pair momentum k (as it would be correct for the interference part) can be taken to be approximately equal to the one evaluated at p_i [41]. This *smoothness approximation* was found to be reasonable for high-energetic, large sources, but questionable for smaller sources [38]. Another useful approximation at this point is that the source function can be evaluated on-shell, since the typical source radii are larger than the Compton wavelengths of the observed pions [39].

Now, the correlation function can be formulated in the following way, using Equations (4.9) and (4.2):

$$C(\mathbf{q}, \mathbf{k}) = \frac{\int d^4x_1 d^4x_2 S(x_1, p_1) S(x_2, p_2) |\phi(x_1, x_2, p_1, p_2)|^2}{\int d^4x_1 S(x_1, p_1) \int d^4x_2 S(x_2, p_2)} \quad (4.9)$$

$$\approx 1 + \frac{|\int d^4x S(x, k) e^{iqx}|^2}{|\int d^4x S(x, k)|^2} = 1 + |\tilde{s}(q)|^2$$

with $\tilde{s}(q)$ being the Fourier transform of the normalized source function $s(x, k)$:

$$\tilde{s}(q) = \int d^4x s(x, k) e^{iqx} = \frac{\int d^4x S(x, k) e^{iqx}}{\int d^4x S(x, k)}. \quad (4.10)$$

For the last steps of Equation (??) the smoothness approximation is again applied, i.e. the momentum of a single particle of the pair, p_i , has been replaced by the pair momentum k . The observed correlator $|\tilde{s}(q)|^2$ can be linked to the spatial characteristics of the source, $s(x, k)$. Although the correlator is obtained as a Fourier transform of the emission function $s(x, k)$, the latter cannot be reconstructed uniquely from the momentum correlator. The reason is the mass-shell constraint of the observed pions, which implies that only three of the four relative momentum components are kinematically independent [41]:

$$k \cdot q = p_1^2 - p_2^2 = m_1^2 - m_2^2 = 0 \quad (4.11)$$

$$\Rightarrow q^0 = \frac{\mathbf{k}}{k^0} \cdot \mathbf{q} = \beta \mathbf{q}. \quad (4.12)$$

Here, m_i is the particle mass, β is the pair velocity normalized to the speed of light and q^0 , k^0 indicate the zero component of the four-momentum difference and the pair momentum four-vector. Hence, the q -dependence of $C(\mathbf{q}, \mathbf{k})$ allows to test only three of the four independent x -directions of the emission function. This introduces an unavoidable model-dependence in the reconstruction of $s(x, k)$, which can only be removed by additional information not encoded in the two-particle correlations between identical particles [41]. Furthermore, the correlator mixes spatial and temporal information in a non-trivial way depending on the pair velocity β .

4.2.2. Gaussian Parametrization

To extract physical information from a measured correlation function, the size and shape of the source have to be described by a few parameters that are linked to properties of the measured correlation function. In practice, the two-particle correlation function is usually parametrized by a Gaussian function in the relative momentum components. A relation of the corresponding width parameters (*HBT radii*) with the space-time structure of the source can be established in the following way.

The space-time saddle point $\bar{x}(k)$ of the emission function $S(x, k)$ indicates the point in space-time that has the maximum probability of emitting a pair particle with momentum k (Note, that again the momentum of a single particle of the pair, p_i , has been replaced by the pair momentum k , according to the smoothness approximation). A quadratic saddle-point approximation for $S(x, k)$ around $\bar{x}(x, k)$ yields [42]:

$$S(x, k) = N(k)S(\bar{x}(k), k) \exp \left[-\frac{1}{2} \tilde{x}^\mu(k) B_{\mu\nu}(k) \tilde{x}^\nu(k) \right] + \delta S(x, k), \quad (4.13)$$

where $N(k)$ is the normalization factor,

$$\bar{x}(k) = \langle x \rangle = \frac{\int d^4x S(x, k) x}{\int d^4x S(x, k)}, \quad (4.14)$$

$$\tilde{x}_\mu(k) = x_\mu - \bar{x}_\mu(k), \quad (4.15)$$

$$(B^{-1})_{\mu\nu}(k) = \langle \tilde{x}_\mu \tilde{x}_\nu \rangle. \quad (4.16)$$

The term $\delta S(x, k)$ contains only higher order information and is neglected. The correlation function following from the above approximation then reads [39]:

$$C(\mathbf{k}, \mathbf{q}) = 1 + \exp[-q^\mu q^\nu \langle \tilde{x}_\mu \tilde{x}_\nu \rangle(\mathbf{k})]. \quad (4.17)$$

The point of the highest emission probability, $\bar{x}(k)$ is not accessible via the correlation function, only the variance or effective width, the *length of homogeneity*, $\langle \tilde{x}_\mu \tilde{x}_\nu \rangle$ can be extracted. The spatial correlation tensor $B_{\mu\nu}(k)$ is symmetric and thus has 10 independent entries. Again, the mass-shell constraint leads to the fact that only 6 linear combinations of these 10 parameters can be measured with identical particle interferometry. The actual form of these combinations depends on the parametrization of the correlation function. The connection between the extracted parameters, the *HBT radii*, and the variances is model independent, i.e. independent of the details of the emission function $S(x, k)$.

The tensor $B_{\mu\nu}(k)$ is able to characterize essential features of the emission function even if $S(x, k)$ is not differentiable or if its curvature at the saddle point does not represent its average sufficiently well [41].

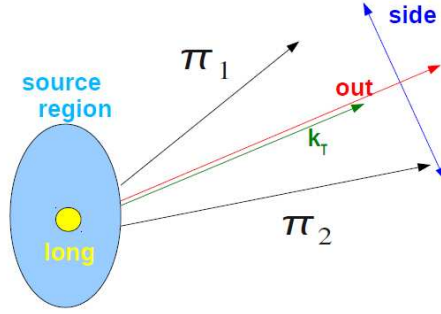


Figure 4.1.: The Pratt–Bertsch parametrization, illustrated in the transverse plane.

Cartesian Decomposition

The correlation function is usually described within the Pratt–Bertsch parametrization: the *out* axis pointing along the transverse pair momentum k_T , the *long* direction along the beam axis, and the *side* axis perpendicular to the other two (Figure 4.1).

The standard Cartesian parametrization can be obtained by eliminating q^0 from Equation (4.17):

$$C(\mathbf{q}, \mathbf{k}) = 1 + \exp\left[-\sum_{i,j=o,s,l} R_{ij}^2(k) q_i q_j\right], \quad (4.18)$$

where o, s, l indicate the three directions *out*, *side* and *long* and the HBT radii are given by the variances:

$$R_{ij}^2 = \langle (\tilde{x}_i - \beta_i \tilde{t})(\tilde{x}_i - \beta_i \tilde{t}) \rangle. \quad (4.19)$$

Since $\beta_{side} = 0$ from the definition of the *side* direction, the radii read:

$$R_{out}^2 = \langle (\tilde{x} - \beta_T \tilde{t})^2 \rangle \quad (4.20)$$

$$R_{side}^2 = \langle \tilde{y}^2 \rangle \quad (4.21)$$

$$R_{long}^2 = \langle (\tilde{z} - \beta_L \tilde{t})^2 \rangle. \quad (4.22)$$

Clearly, the radius parameters mix spatial and temporal information. Only R_{side} is directly connected to the spatial variance, since by construction the pair velocity in this direction vanishes. R_{out} is sensitive to the transverse pair velocity β_T , R_{long} to the longitudinal pair velocity β_L . In an azimuthally integrated analysis of boost invariant collisions at mid-rapidity the cross-terms (R_{ij} for $i \neq j$) vanish because of symmetry considerations.

The radius parameters can also be connected to the key properties of the source modeled within a hydrodynamic calculation. The radii are given by [41]:

$$R_{side}^2(k_T) = \frac{R_{geo}^2}{1 + m_T \eta_f^2}, \quad (4.23)$$

$$R_{out}^2(k_T) = R_{side}^2(k_T) + \frac{1}{2} \left(\frac{T}{m_T} \right)^2 \beta_T^2 \tau_0^2, \quad (4.24)$$

$$R_{long}^2(k_T) = \frac{\tau_0^2 T K_2(m_T/T)}{m_T K_1(m_T/T)}, \quad (4.25)$$

where k_T is the transverse pair momentum, R_{geo} is the actual geometrical source size, K_1 and K_2 are modified Bessel functions, T is the temperature at which the medium reaches equilibrium, and the transverse pair mass m_T is given by $m_T = \sqrt{m_\pi^2 + k_T^2}$. The factor η_f indicates the transverse flow strength and τ_0 the freeze-out time. This implies that R_{side} is sensitive to the actual source size and influenced by the source dynamics given by the transverse flow and the particle masses and momenta. R_{out} in addition is also sensitive to the freeze-out time and initial temperature T . R_{long} can be used to estimate the freeze-out time since it is proportional to τ_0 .

The correlation function is commonly expressed in a *longitudinally co-moving system* (LCMS), a rest frame moving along the beam axis such that the total longitudinal momentum of the pair vanishes.

4.3. Experimental Technique

The experimental construction of the correlation function is given by:

$$C(\mathbf{q}, \mathbf{k}) = \frac{A(\mathbf{q})}{B(\mathbf{q})} \cdot \xi(\mathbf{q}). \quad (4.26)$$

The numerator $A(\mathbf{q})$ is the signal distribution and the denominator $B(\mathbf{q})$ the background distribution. Ideally, $B(\mathbf{q})$ is identical to the signal distribution but without the quantum correlation effect. The correction factor $\xi(\mathbf{q})$ accounts for non-HBT correlations, e.g. due to energy-momentum conservation, or for effects such like finite momentum and two-track efficiency.

$A(\mathbf{q})$ and $B(\mathbf{q})$ are the distributions of the momentum differences of the pion pairs for a certain event, track and pair selection. The selection criteria must be identical for both signal and background distributions. Selection criteria are for example: (i) event quality; (ii) event centrality; (iii) longitudinal vertex position; (iv) track quality; (v) pair quality; (vi) pair momentum; and (vii) pair emission angle.

Single-particle efficiencies divide out, if the background is properly constructed, but two-track efficiencies can have a huge influence on the correlation function since they produce strong additional correlation structures. A cut on close track pairs is applied to exclude pairs that are potentially affected by two-track reconstruction difficulties from the correlation function. More details are discussed in Chapter 5.

The background is built by constructing pairs of particles that come from different events and are therefore uncorrelated (*event mixing*). The violation of energy-momentum conservation introduced by event mixing is negligible in the case of high-multiplicity events such as in high-energy heavy-ion collisions. In order to avoid additional structures in the correlation function, the particles forming the pairs in the background distribution should originate from events with similar characteristics. The events should also have a similar vertex position and the detector acceptance should be similar. That is, the events should have similar single-particle distributions, similar centralities and orientations of the reaction plane, and similar z-vertex positions.

The obtained correlation function then has to be corrected for finite resolution effects and mis-identified particles. Furthermore, final state interactions have to be considered. These effects are discussed in the following.

Some particles measured in the experiment come from resonance decays. A fraction of them might be identified and removed from the analysis, but especially the ones coming from short-lived particle decays, e.g. from η mesons, remain. Such particles are basically uncorrelated with the other particles. This fraction of uncorrelated particles remaining in the correlation function will reduce the measured correlation by a factor of λ . This has to be taken into account in the fitting procedure (see Section 4.3.1).

Coulomb interaction between the pions of the pair has a large effect at low q and has to be taken into account when fitting experimental data. The relative two-particle Coulomb wave function reads [43]:

$$\psi_C = \Gamma(1 + i\eta) \exp\left(-\frac{1}{2}\pi\eta\right) \exp(i\mathbf{q}\mathbf{r}) \times F(-i\eta, 1, i(qr - \mathbf{q}\mathbf{r})) \quad (4.27)$$

where $\eta = \mu e^2/\hbar q$ with the reduced mass μ and the elementary charge e , and F is the regular confluent hypergeometric function. It can also be written in the following form [38]:

$$\psi_C = \Gamma(1 + i\eta) \exp\left(-\frac{1}{2}\pi\eta\right) \exp(i\mathbf{q}\mathbf{r}) \left[1 + \sum_{n=1}^{\infty} h_n \left(\frac{r}{a_0}\right)^n\right] \quad (4.28)$$

$a_0 = 387$ fm is the two-pion Bohr radius and $h_1 = 1$, $h_n = \frac{n-1-i\eta}{-in\eta} h_{n-1}$. In the limit of vanishing separation of the pions, $r \rightarrow 0$, the squared wave function is given by

the Gamov Factor:

$$G(\eta) = e^{-\pi\eta} |\Gamma(1 + i\eta)|^2 = \frac{2\pi\eta}{e^{2\pi\eta} - 1} \quad (4.29)$$

The Gamov Factor overestimates the actual Coulomb effect due to the approximation $r \rightarrow 0$. The assumption of a small source compared to the relevant Coulomb length scale given by $q^2/(2\mu e)$ is not justified in the case of heavy-ion collisions [44]. Here, screening due to the presence of the medium reduces the Coulomb effect as well. The Coulomb interaction can be calculated with Equation (4.28) for a source radius estimated from the measured radius parameters. Since the considered radius influences the extracted radii, this is an iterative process, but usually needs only a few steps. The squared unsymmetrized Coulomb wave function for a finite Gaussian source, $K(\mathbf{q})$, is included in the fitting procedure (explained in the following Section). Like this, the effect of the Coulomb interaction on the radius parameters is taken into account (effect of up to about 10% on the extracted radii).

4.3.1. Fitting

After the application of all necessary corrections, the correlation function is fitted to extract the HBT radii parameters according to Bowler and Sinyukov [45]:

$$C(\mathbf{q}) = N[\lambda G(\mathbf{q})K(\mathbf{q}) + (1 - \lambda)]. \quad (4.30)$$

The Gaussian fitting function has the following form:

$$G(\mathbf{q}) = 1 + \exp(-R_o^2 q_o^2 - R_s^2 q_s^2 - R_l^2 q_l^2) \quad (4.31)$$

$$- 2R_{os}^2 q_o q_s - 2R_{ol}^2 q_o q_l - 2R_{sl}^2 q_s q_l). \quad (4.32)$$

If the analysis is performed integrated over the full azimuth the cross-terms in the second row vanish. These fitting parameters are the *HBT radii*. As already mentioned, correlations do not measure the entire size of the source but only address the properties of the ‘‘homogeneity region’’ [46]. If the collective expansion is strong, as it is the case in high-energy heavy-ion collisions, the homogeneity region is significantly smaller than the entire source volume.

A χ^2 test is inappropriate for fitting correlation functions because the ratio of two Poisson distributions is not itself Poisson distributed, especially when taking the ratio of small numbers. For this reason, a log-likelihood fit function of the form given by:

$$\chi_{ML} = -2 \left[A \ln \left(\frac{C(A+B)}{A(C+1)} \right) + B \ln \left(\frac{A+B}{B(C+1)} \right) \right] \quad (4.33)$$

where A is the signal distribution, B the background distribution and C the ratio, is better suited [38].

4.4. Observed Systematics of the HBT Radii, measured with ALICE

In the following, the trends of the HBT radii in dependence on the pair momentum and the particle density are discussed, using the first heavy-ion HBT results measured at the LHC with ALICE [47] as an example.

As already discussed, HBT radii probe the homogeneity region, and not the entire source size. Nevertheless, the claim that two-particle correlations probe spatial scales is supported by the fact that the radii exhibit a strong correlation with system size. Therefore, measuring the systematic variation of the radii with system composition and centrality represents the most basic test of both theoretical concepts and experimental techniques. Furthermore, the connection between space-momentum correlations induced by an expansion of the source and the dependence of the radii on the transverse pair momentum $k_T = (p_{T,1} + p_{T,2})/2$ allows to test the hydrodynamical picture in detail.

The data used for the presented ALICE results was collected in collisions at $\sqrt{s_{NN}} = 2.76$ TeV during the first heavy-ion run at LHC in November 2010. About $1.6 \cdot 10^4$ events from the most central 5% of the hadronic cross-section were analyzed. The average charged-particle multiplicity in this sample is $\langle dN_{ch}/d\eta \rangle = 1601 \pm 60$ (sys.) [22]. Primary pions with pseudorapidity $|\eta| < 0.8$ reconstructed with ITS and TPC were identified via their specific energy loss inside the TPC.

4.4.1. Dependence on Particle Density

There are several ways to confirm the connection between the HBT radii and the system size:

- The measured homogeneity lengths are found to be increasing with a decreasing impact parameter. HBT radii are found to be larger for more central events, as would be expected from a simple geometric picture of two overlapping nuclei.
- The radii were found to be dependent on the size of the colliding nuclei, they increase with increasing projectile mass.
- The radii show a linear dependence with the final-state particle density, $(dN_{ch}/d\eta)^{1/3}$, with finite intercepts. The uniformity of the scaling with the final-state particle density supports the argument that the radii parameter probe the *freeze-out* source geometry. Since the number of participants is strongly connected to the final-state particle density, the dependence of the

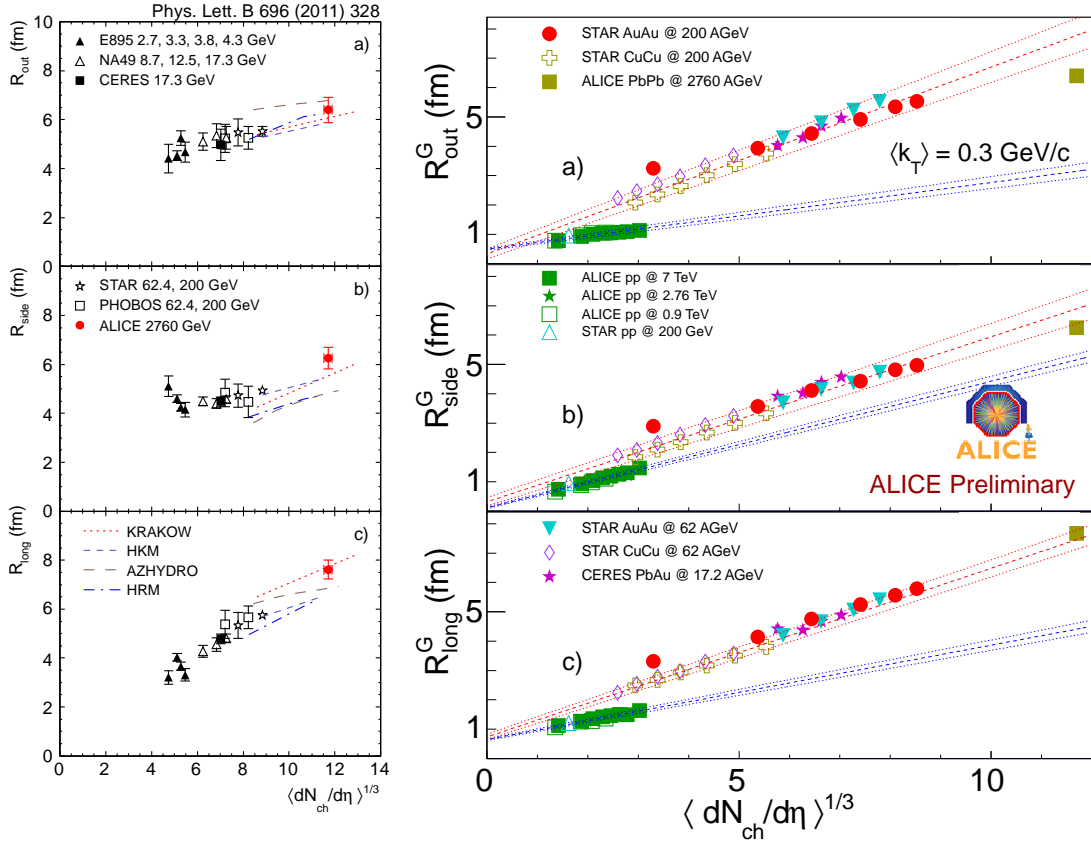


Figure 4.2.: Multiplicity dependence of the measured radii compared to results from previous experiments at lower energies (left) [47], and for various centralities and several collision systems (right) [55].

radii on N_{part} is also approximately linear but not as uniform as the scaling with $(dN_{ch}/d\eta)^{1/3}$.

In the left panel of Figure 4.2 the radii parameter extracted from central Pb–Pb events measured with ALICE at the LHC are compared to results for very central events from previous experiments at lower energies. A clear increase of the radii can be seen for all three components as a function of charged-particle pseudorapidity density. Model calculations following a hydrodynamic approach, AZHYDRO [48], KRAKOW [49, 50], HKM [51, 52], as well as predictions from a hadronic-rescattering model HRM [53, 54], are compared to the data. The models reproduce the overall trend well. The right panel of Figure 4.2 compares the measured values to results for different centralities and collision systems from various experiments as well as to the ALICE results from proton-proton collisions (pp). The data confirms the scaling of the radii with multiplicity observed in former experiments. The pp radii also show a linear dependence but compared to heavy-ion results the slope and the intercept is

different. This indicates an influence of the initial geometry on the measured HBT radii. With ALICE it will be possible for the first time to measure pp and heavy-ion collisions with comparable event multiplicities such that they can be analyzed with the same experiment and techniques to study in detail the role of the initial collision geometry.

4.4.2. Pair Transverse Momentum Dependence

As seen before, the emission function describing the pion pair emission from the source is a function of both the pair momentum \mathbf{k} and the momentum difference \mathbf{q} . If the correlation function is parametrized by a Gaussian in the relative momentum \mathbf{q} , the extracted radii parameters still contain the pair momentum dependence of the emission function. Only if the \mathbf{k} and \mathbf{q} dependent parts of the emission function factorize and the \mathbf{k} dependence therefore drops out in the ratio of the correlation function, the radii are not expected to exhibit a dependence on \mathbf{k} . In thermal sources, space-momentum correlations introduced by temperature gradients or collective expansion (flow) prevent such a factorization. Hence, the dynamic substructure of the source encoded in such space-momentum correlations influences the momentum dependence of the radii parameter. The k_T dependence of the radii therefore leads to strong constraints on hydrodynamic models that aim to describe the reaction dynamics.

A characteristic fall-off of the pion source radii with k_T , which is observed in data, is generally interpreted as the signature of a collective expansion. This can be understood in the following way (illustrated in Figure 4.3): for each particle a part of its velocity is coming from the random thermal motion and another part is coming from the collective expansion, pointing outwards of the source region. If only large pair momenta are considered, both particles must originate from the same region of the source, since only then the expansion velocity points in the same direction and can be combined to a large pair momentum. If small pair momenta are considered, also pairs with pions coming from different regions of the source are possible, since the random thermal velocity might be enough to change the emission direction; the resulting total velocity of this particle is then small.

Figure 4.4 shows the measured k_T dependence for the three radii parameters as well as for the ratio R_{out}/R_{side} . A decrease of the radii with increasing pair transverse momentum consistent with an expanding source is observed. Compared to results from the STAR experiment at RHIC, from Au+Au collisions at $\sqrt{s_{NN}} = 200$ GeV the radii are found to be larger for all k_T . The ratio of R_{out}/R_{side} is slightly smaller compared to RHIC. The above-mentioned theoretical models are compared to the data, showing that hydro models including hadronic rescattering, namely KRAKOW and HKM, describe the data best.

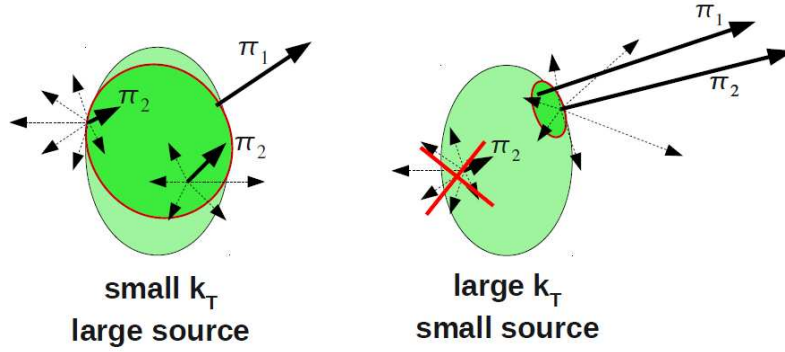


Figure 4.3.: Illustration of the k_T dependence of the radii due to an expanding source.

4.4.3. Lifetime and Homogeneity Volume

The product of the three radii is connected to the homogeneity volume at freeze-out. Compared to previous experiments at lower energies a clear increase is seen as well as a linear dependence on the particle density (Figure 4.5, left). Within hydrodynamic scenarios the decoupling time τ_0 can be estimated from the longitudinal component R_{long} (see also Equation (4.25)):

$$R_{long}^2(k_T) = \frac{\tau_0^2 T K_2(m_T/T)}{m_T K_1(m_T/T)}. \quad (4.34)$$

K_1 and K_2 are modified Bessel functions of the first and the second kind, respectively, the temperature T is here assumed to be 0.12 GeV and the transverse mass m_T is given by $m_T = \sqrt{m_\pi^2 + k_T^2}$. The extracted decoupling times presented in Figure 4.5 (right) scale with particle density. The value measured by ALICE is about 40% higher than those observed at previous experiments.

4.5. Summary

Bose–Einstein correlations of identical pions provide information on the size of the emission region at freeze-out. The two-particle correlation function can be calculated from the single particle and pair distributions. Under several assumptions that are well-justified in the case of heavy-ion collisions, the measurable correlator leads to the Fourier transform of the distribution of spatial distances. In practice, the Fourier transform cannot be performed unambiguously and further model assumptions are needed to reconstruct the source from the measured correlations. Within a Gaussian parametrization the extractable radii parameters provide insight into the space-time structure of the source.

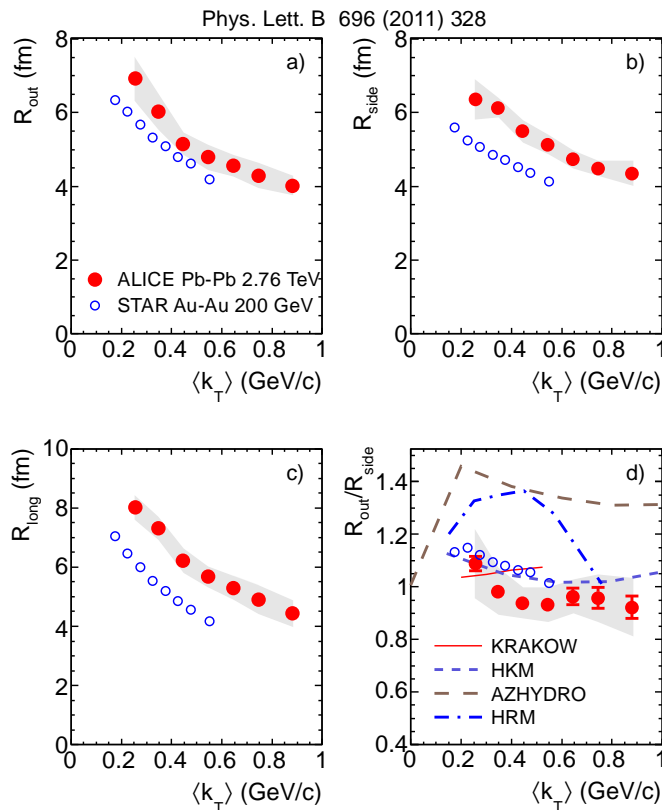


Figure 4.4.: Transverse pair momentum dependence of the measured HBT radii compared to RHIC results from STAR and to model predictions (Figure from [47]).

The scaling of the experimentally extracted radii parameters with final-state particle density supports the argument that HBT probes the freeze-out characteristics of the source rather than the initial conditions. The dependence of the radii on collision centrality and system size shows that HBT radii probe the system size, although only the homogeneity region of the source is assessed.

The decrease of the measured radii with increasing pair transverse momentum is a sign of collective expansion. The exact slope provides strong constraints on hydrodynamical models that aim at describing the source evolution.

ALICE measured the HBT radii in Pb–Pb collisions at $\sqrt{s_{NN}} = 2.76$ TeV at LHC. The radii are found to be 10–35% larger than at RHIC, the increase is seen in the longitudinal as well as in the transverse directions. Trends in the k_T and multiplicity dependence of the radii are consistent with previous experiments and well predicted by some models. Quantitatively, hydrodynamic scenarios including hadronic rescattering are preferred by the data. The measured homogeneity volume is found to be twice as large as at RHIC. The extracted decoupling time is larger than at RHIC by more than 40%. Both quantities scale with charged-particle pseudorapidity density.

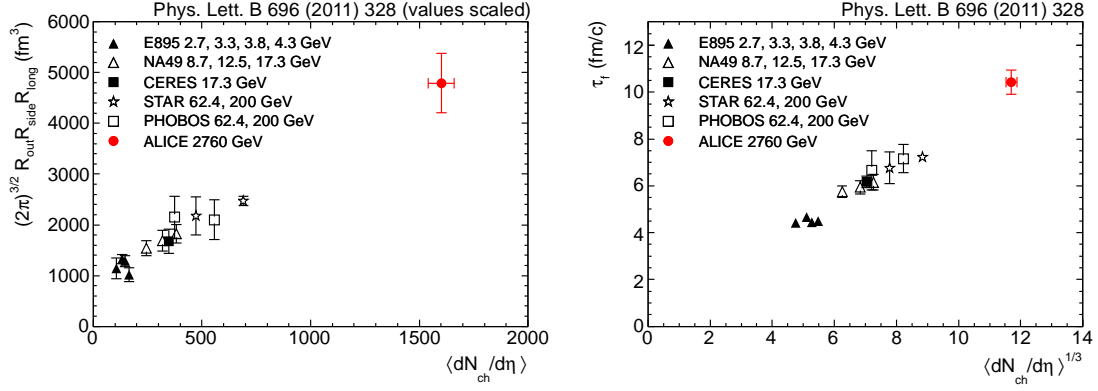


Figure 4.5.: Product of HBT radii (left) and decoupling time (right) obtained by ALICE, compared to the results obtained by previous experiments at lower energies (Figures from [47]).

The results suggest that the system created in Pb–Pb collisions at LHC expands to a larger size, has a higher initial temperature, and lives longer than at lower energies.

5. Two-Track Resolution

As discussed in the previous Chapter, the technique of Hanbury Brown–Twiss (HBT) interferometry uses the Bose–Einstein correlation of identical particles to gain information on the space-time extension of the region from which the particles are emitted. For this purpose, the number of correlated pairs as a function of their momentum difference, normalized to a sample of uncorrelated pairs, is analyzed. The Bose–Einstein statistics results in a peak in the region where the tracks have very similar momenta.

Pairs formed out of tracks with similar momenta and a small angular difference are affected by particular reconstruction effects, namely:

- **Track merging:** Two tracks that are spatially very close are falsely reconstructed as one. This shows up as an inefficiency of close pairs compared to a sample of unaffected pairs.
- **Track splitting:** One track is falsely reconstructed as two tracks that are spatially close. This shows up as an enhancement of close pairs compared to an uncorrelated sample.

Such pairs appear in the correlation function in the HBT peak region at low momentum differences and affect the extracted HBT radii. A cut on the track separation that removes all affected pairs from the numerator (correlated pairs) and the denominator (uncorrelated pairs) of the correlation function can prevent a bias on the HBT results.

In this Chapter, a detailed study of such a cut is presented. First, the analysis framework and data sample used for the development of the cut is explained. The effect of track merging and track splitting as a function of the angular distance of the tracks of a pair is shown in terms of several variables that could be used for a cut. The effects are quantified and a cut value is extracted. Finally, the effects on the correlation functions and the fit results are presented.

5.1. Analysis Framework and Data Sample

The ratio of a correlated sample of pairs and an uncorrelated sample, where one track of each pair is rotated in azimuth by π , is analyzed with respect to the angular

Variable	Description
p_{T1}	transverse momentum of particle 1
η_1	pseudorapidity of particle 1
φ_1	transverse direction of particle 1
$nsh1$	number of shared clusters of particle 1
p_{T2}	transverse momentum of particle 2
η_2	pseudorapidity of particle 2
φ_2	transverse direction of particle 2
$nsh2$	number of shared clusters of particle 2
q_{inv}	momentum difference
$mindist$	minimal distance inside the TPC
$dist$	distance at the TPC entrance
$corr$	correlation coefficient (not used)
$qfac$	quality factor (not used)

Table 5.1.: Variables stored in the `NTuple` created by the AliROOT class `AliTwoTrackRes`.

distance between the tracks of the pairs. The rotation of one pair track by π is here used instead of event mixing to obtain a sample of uncorrelated pairs, which is a valid approach in this case. In such a ratio, two-track effects are clearly visible since they are only present in the sample of unrotated pairs. They show up either as an inefficiency in the case of track merging or as a sharp peak if tracks are split. To understand the structures in such a ratio, a Monte Carlo sample is used in the following. Bose–Einstein correlations are not present in Monte Carlo, therefore a flat ratio is expected and the two-track effects will be clearly visible as a deviation from unity.

Technically, this study is based on the AliRoot class `AliTwoTrackRes` which can be found in `PWG2/FEMTOSCOPY/AliFemto`. It creates one `NTuple` of real pairs, and one `NTuple` of pairs of which one track was rotated by π . The variables stored in the `NTuple` are listed in Table 5.1.

In the following, only the kinematic variables p_{Ti} , φ_i and η_i of the tracks are used. The momenta are either taken from the global track information or from the TPC information only. Comparing these two cases serves as a consistency check.

The Monte Carlo sample used for this study was created using the thermal heavy-ion generator Therminator [31]. It contains about 86 000 0-5% central Pb–Pb events that are propagated through a full ALICE detector simulation. The track quality cuts that are applied in the analysis are listed in Table 5.2. These cuts ensure a reasonably clean sample of primary tracks with a good reconstruction quality and are similar to the track cuts used in a typical HBT analysis.

Cut Variable	Cut Value
Distance of closest approach to primary vertex	$< 3\sigma$
Number of reconstructed TPC clusters	< 75
Maximum χ^2 per TPC cluster	3.5
Refit of TPC part of track	active
Kink ¹ rejection	active

Table 5.2.: List of track cuts that are applied in the two-track resolution study.

5.2. Variables Describing the Track Separation

In order to define a useful two-track cut, a set of variables has to be found first, in which the region affected by two-track reconstruction effects is well-defined and the distinction between affected pairs and unaffected pairs is very clear.

The reconstruction efficiency of pairs with close tracks depends on their distance. Therefore, a reasonable approach is to study track merging and track splitting as a function of the angular distance between the tracks of a pair.

5.2.1. Angular Distance in $\Delta\eta$ and $\Delta\varphi$

As a first step, the $(\Delta\eta, \Delta\varphi)$ distribution of the pairs is studied. If the pair distribution from the “real”, i.e. correlated, `NTuple` is divided by the one from rotated pairs, shown in Figure 5.1, an inefficiency due to track merging in the region of small $\Delta\eta$ and $\Delta\varphi$ becomes clearly visible. Additionally, a very narrow spike indicates track splitting. The exact shape of the ratio depends on the transverse pair momentum $k_T = (p_{T,1} + p_{T,2})/2$: for small k_T the spike is more visible and the inefficiency hole is not as deep. Since splitting occurs mainly due to shared hits in the ITS, the spike is not present in the case of TPC-only tracks (Figure not shown). Track merging is more important than track splitting both for global and TPC-only tracks as can be seen by the fact that in both cases the inefficiency caused by track merging is dominant over a spike from split tracks.

The transverse angular difference $\Delta\varphi$ is taken at the vertex and the bending of the tracks in the transverse plane due to the magnetic field is not considered. However, the variable that determines whether or not two tracks get merged is their “corrected” $\Delta\varphi$, the angular distance inside the detector including the effect of the magnetic field.

¹A kink track is a track of a charged particle decaying into one light neutral and one heavier charged daughter. This results in a track that has a small kink at the decay point.

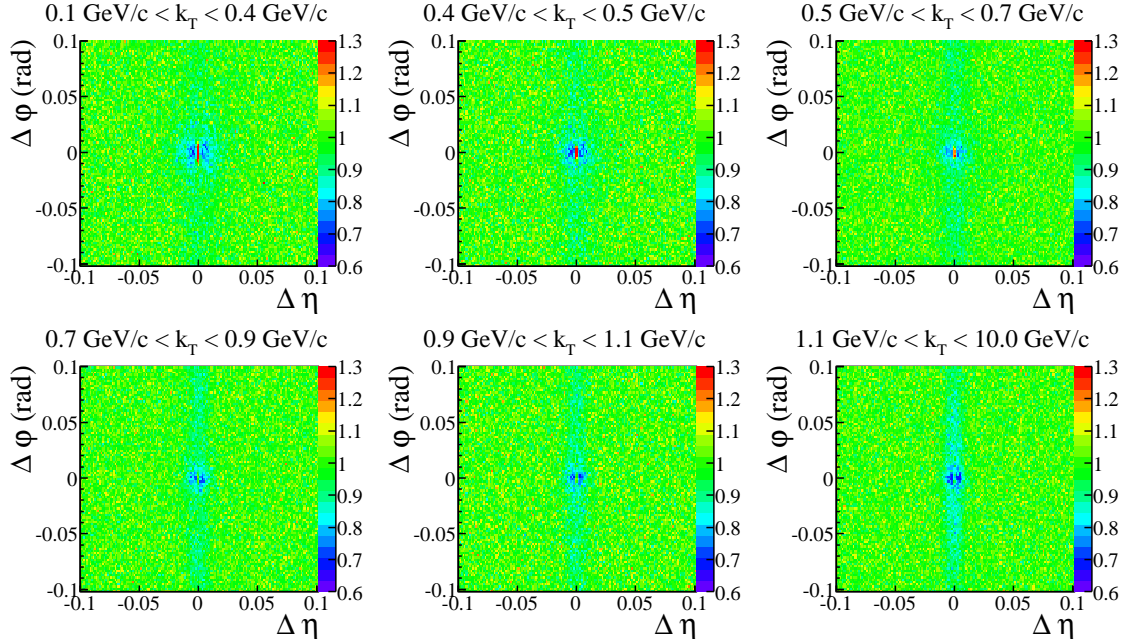


Figure 5.1.: Two-dimensional ratio in $(\Delta\eta, \Delta\varphi)$ for different ranges in pair momentum k_T (global tracks).

5.2.2. Angular Distance in $\Delta\eta$ and $\Delta\varphi^*$

To obtain the angular distance of two tracks in the transverse plane at a given cylindrical radius R the bending inside the magnetic field has to be taken into account. This can be calculated explicitly and the angular distance of the tracks in φ then reads:

$$\Delta\varphi^* = \varphi_1 - \varphi_2 + \arcsin\left(\frac{z \cdot e \cdot B_z \cdot R}{2p_{T1}}\right) - \arcsin\left(\frac{z \cdot e \cdot B_z \cdot R}{2p_{T2}}\right). \quad (5.1)$$

Here, φ_1 and φ_2 are the azimuthal angles of the tracks at the vertex, p_{T1} and p_{T2} are their transverse momenta. e stands for the elementary charge. B_z indicates the magnetic field in z direction (see also Figure 5.2). The inefficiency region appears different for different radii R as can be seen in Figure 5.3. For radii inside the ITS, i.e. $0.2\text{ m} < R < 0.8\text{ m}$, the inefficiency is hardly visible and spread out. For radii inside the TPC, i.e. $0.8\text{ m} < R < 2.5\text{ m}$ the hole is well-defined and considerably deep.

The observed trends regarding the k_T dependence (Figure 5.4) are similar to the ones discussed for $\Delta\varphi$ (Figure 5.1): the inefficiency around $\Delta\eta = 0$ and $\Delta\varphi = 0$ is deeper for higher pair momenta. A “smearing” in $\Delta\varphi^*$ is present, even though not

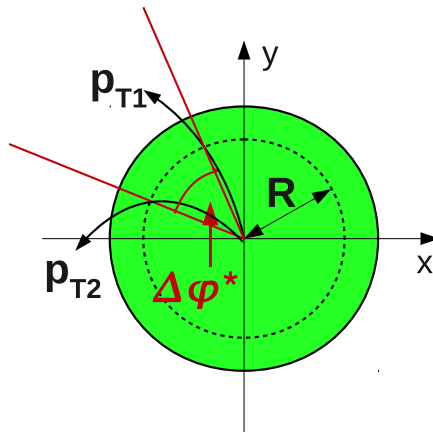


Figure 5.2.: Illustration of the variable $\Delta\varphi^*$.

equally prominent for all radii. This can be understood by the following consideration. Pairs that do not come too close at the considered radius, can come closer at another radius. So they can be affected by merging even though their distance at the considered radius might be large enough. This “smearing” is more visible for lower k_T bins, since such pairs are bent stronger in the magnetic field and their difference in φ can change significantly from one radius to another, whereas tracks from pairs with high k_T almost keep their direction and therefore their $\Delta\varphi$.

The trends discussed above are also clearly seen in the projections on $\Delta\eta$ and $\Delta\varphi^*$ over the peak region, shown in Figure 5.5 and in Figure 5.6.

For $R = 1.2\text{m}$, the inefficiency hole is deepest and in addition the smearing in $\Delta\varphi^*$ is less than for all other bins. A cut on $\Delta\eta < 0.01$ and $\Delta\varphi^* < 0.02$ rad at a radius of 1.2m was used in the first ALICE Pb–Pb HBT analysis [47]. It is a reasonable compromise, since the smearing does not dominate while the inefficiency hole is relatively deep, but it can be improved by using $\Delta\varphi^*$, where the distance is smallest, which will be discussed in the next section.

5.2.3. Angular Distance in $\Delta\eta$ and $\Delta\varphi_{min}^*$

To avoid the observed smearing in $\Delta\varphi^*$ discussed above, $\Delta\varphi^*$ is calculated at that radius where it is minimal for the specific pair, i.e. where the two particles come the closest in φ . This radius is called $R_{CA\varphi}$ in the following. By using that variable, a well-defined inefficiency hole in a flat ratio around $\Delta\eta = 0$ and $\Delta\varphi_{min}^* = 0$ is obtained and the smearing disappears (Figure 5.7).

When looking at TPC-only tracks, only the distance inside the TPC range matters. Therefore, if $R_{CA\varphi}$ is determined inside the TPC volume, i.e. between 0.8 m and

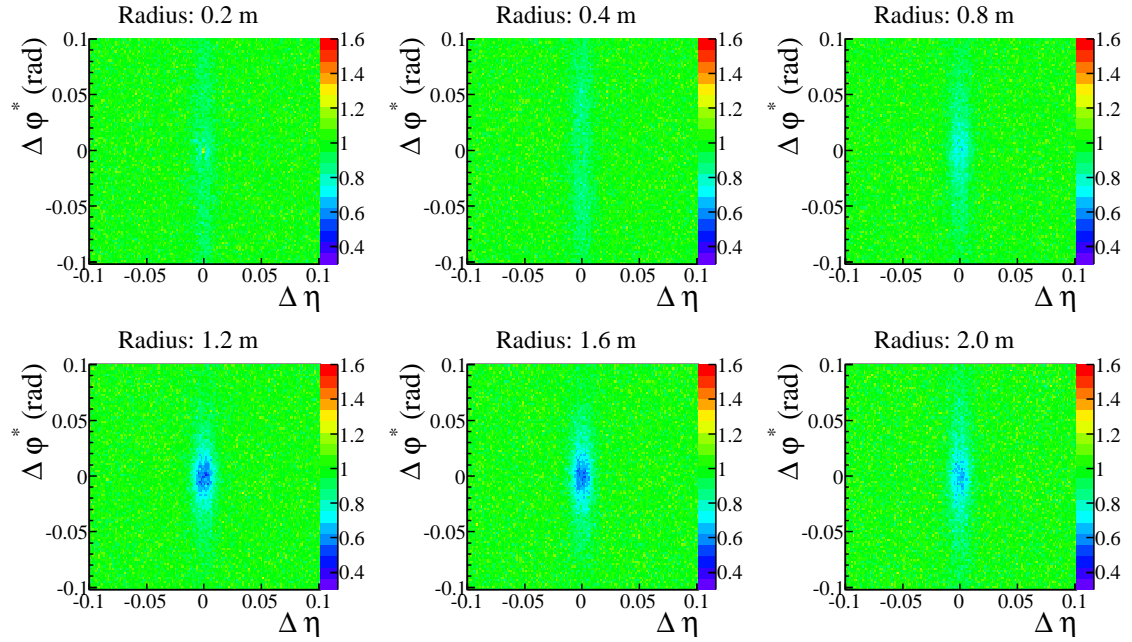


Figure 5.3.: Two-dimensional ratio in $(\Delta\eta, \Delta\varphi^*)$ at different radii for pairs with $0.7 \text{ GeV}/c < k_T < 0.9 \text{ GeV}/c$.

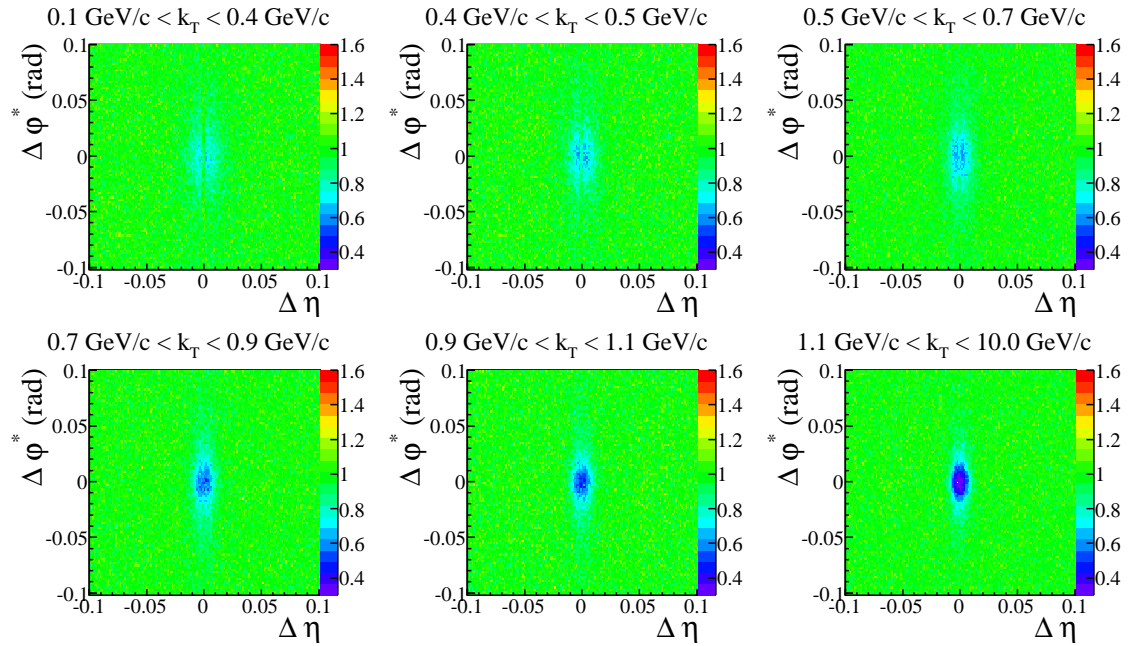


Figure 5.4.: Two-dimensional ratio in $(\Delta\eta, \Delta\varphi^*)$ for different ranges in transverse pair momentum k_T at a radius of 1.2 m.

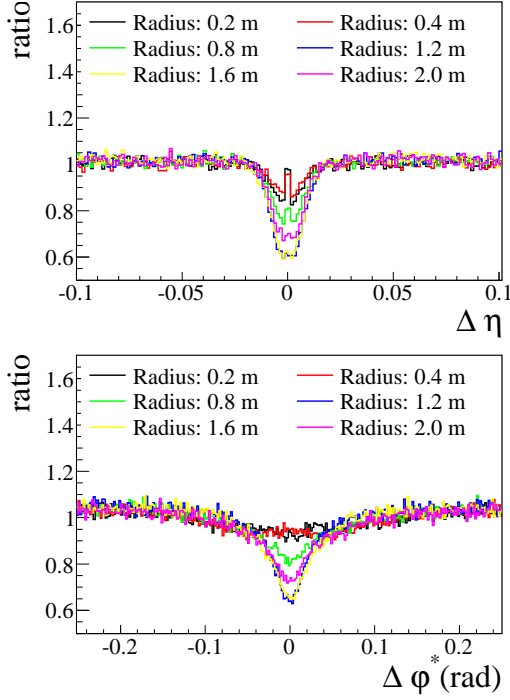


Figure 5.5.: Projections in $\Delta\eta$ and $\Delta\varphi^*$ for $0.7 \text{ GeV}/c < k_T < 0.9 \text{ GeV}/c$ at different radial distances.

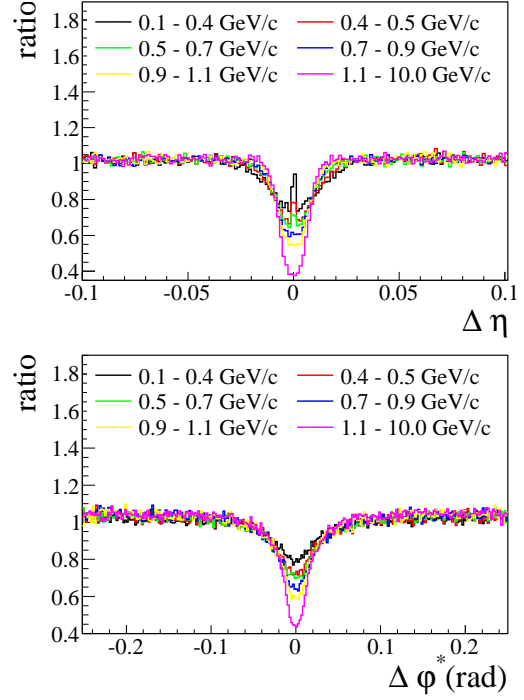


Figure 5.6.: Projections in $\Delta\eta$ and $\Delta\varphi^*$ for different ranges in pair momentum k_T at a radial distance of 1.2 m.

2.5 m, the smearing already disappears (Figure 5.8). In addition, the inefficiency hole is deeper than in the case of global tracks. This can be understood by considering the different pair topologies that are possible (see also Figure 5.14):

- **Sailors:** pairs of tracks that are bent away from each other by the magnetic field. Their $R_{CA\varphi}$ will have the lowest value allowed within the volume under consideration.
- **Cowboys:** pairs of tracks that are bent towards each other by the magnetic field and may cross at some point. Their $\Delta\varphi_{min}^*$ will be zero if they cross within the volume under consideration. If not, they will have either the highest or lowest allowed value.

In case of *sailor* pairs with $\Delta\varphi = 0$ at the vertex, they might be correctly reconstructed if their difference in momentum is large enough and they are well separated later on, i.e. inside the TPC. These pairs show up at very small angular differences in $\Delta\eta$ and $\Delta\varphi_{min}^*$ but are almost not affected by reconstruction effects. Taking $R_{CA\varphi}$ only inside the TPC volume leads to a deeper hole because all these pairs appear at larger angular distances. Around $\Delta\eta = 0$ and $\Delta\varphi_{min,TPC}^* = 0$ only the affected

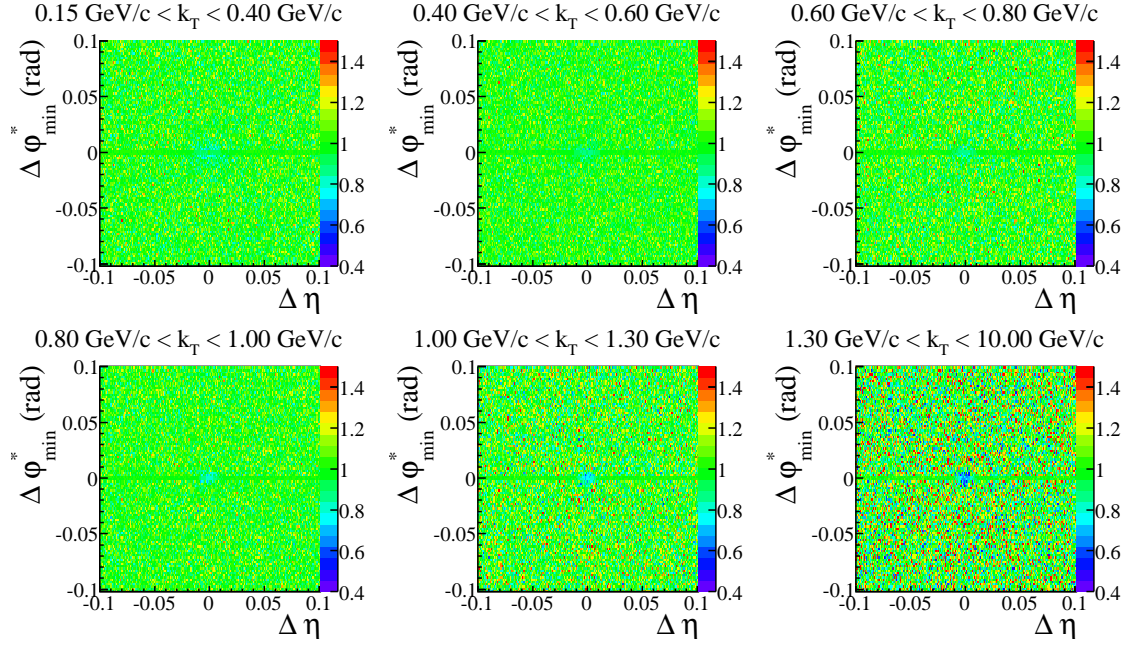


Figure 5.7.: Two-dimensional ratio in $\Delta\eta$ and $\Delta\varphi_{min}^*$ for different ranges in transverse pair momentum (global tracks).

pairs remain. For this reason, $R_{CA\varphi,TPC}$ is preferable to use for applying the cut when looking at TPC-only tracks.

For global tracks the inefficiency hole is also deeper, if the minimal distance in φ is determined only within the TPC region. However, a cut on $\Delta\varphi_{min,TPC}^*$ is not sufficient to remove all affected pairs as can be seen by looking at $(\Delta\eta, \Delta\varphi)$ after the cut (see also Section 5.3.4). Thus, for global tracks the minimal distance should be determined in the whole range between 0 m and 2.5 m to safely exclude the region of affected pairs. This shows that two-track merging effects are also present in the ITS.

For the implementation of a cut it is more convenient to calculate $\Delta\varphi^*$ in steps of 1 cm, for example, instead of determining the minimum exactly. At every step it is checked whether the separation is large enough until either the angular distance is smaller than the cut values - then the pair is taken out - or the maximal radius is reached - then the pair is accepted for the analysis.

5.2.4. Consideration of the Opening Angle α

Another idea for improving the choice of variables and to avoid having unaffected pairs in the cut region is to use the local opening angle of the pair at the point of their

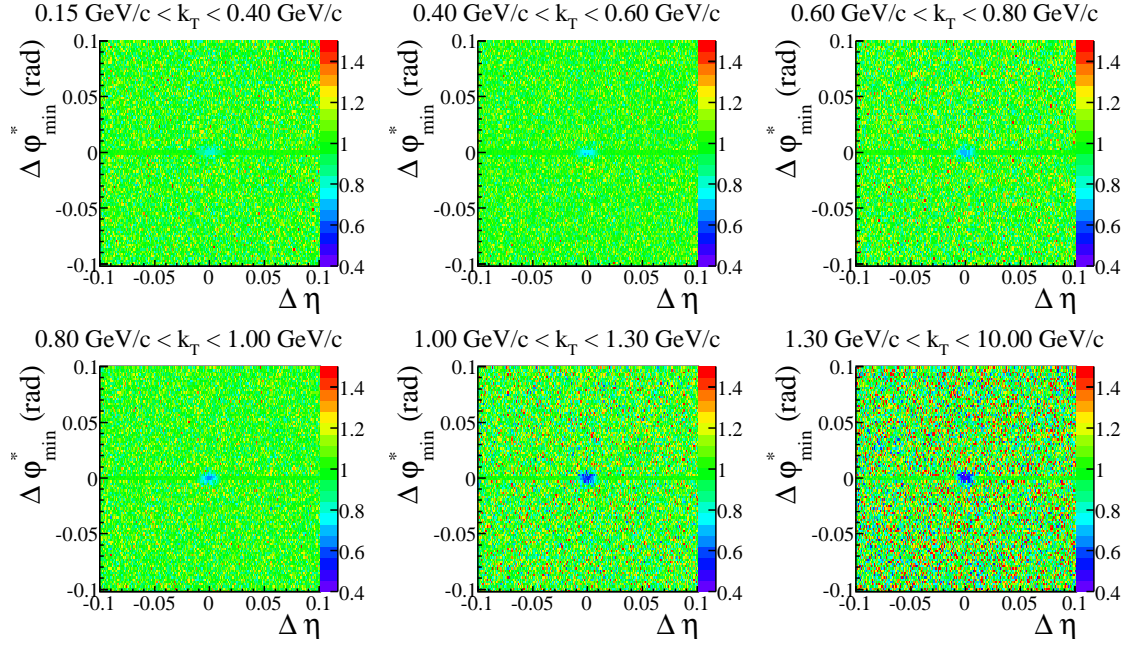


Figure 5.8.: Two-dimensional ratio in $\Delta\eta$ and $\Delta\varphi_{min,TPC}^*$, with the minimum in $\Delta\varphi^*$ determined inside the TPC (TPC-only tracks).

closest approach in addition to their distance as discussed above. The opening angle can be calculated by determining the radius of the point of the closest approach of the pair tracks, and calculating their momenta at that point taking into account the bending in the magnetic field. From the scalar product of the momentum vectors at that point, the opening angle α can be extracted:

$$\mathbf{p}_1 \cdot \mathbf{p}_2 = |\mathbf{p}_1||\mathbf{p}_2| \cos(\alpha). \quad (5.2)$$

The opening angle can also be considered only in the transverse plane as it is easier to interpret. The results for this variable in addition to the angular distance are shown in Figure 5.9.

The range at which the pair inefficiency is spread out in the opening angle α is quite large. Only pairs with large opening angles, i.e. relatively large momentum difference, would benefit from including the opening angle and would be prevented from being removed by a cut. However, such pairs are not relevant for a HBT analysis, since they do not appear in the peak region of the correlation function. Therefore, including the opening angle does not improve the result in this case.

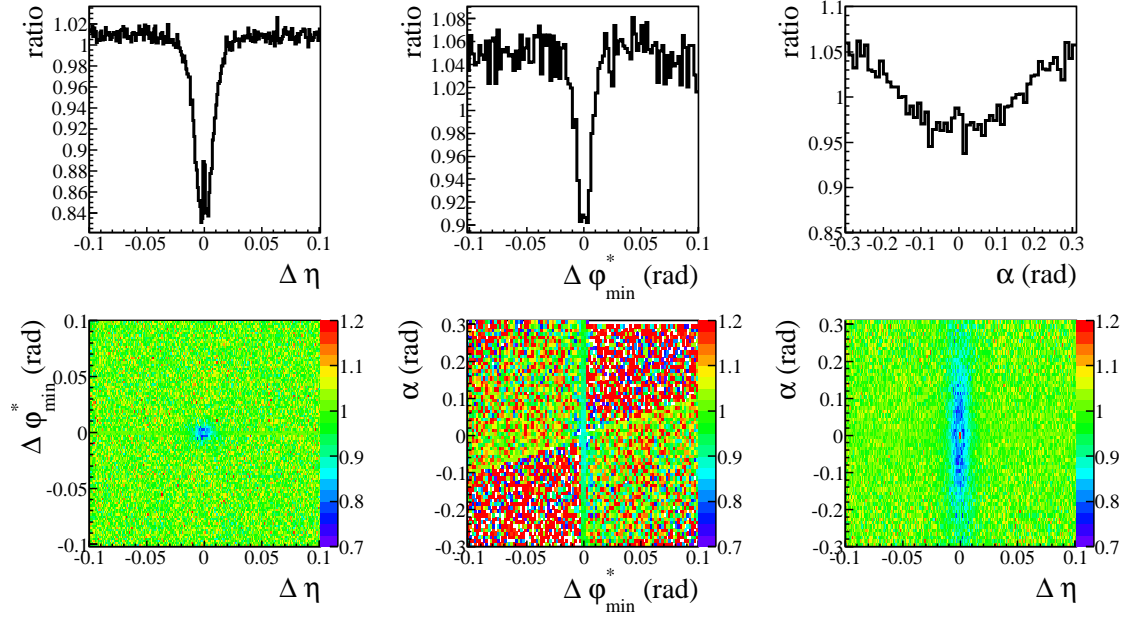


Figure 5.9.: Projections of the three-dimensional correlation on $\Delta\eta$, $\Delta\varphi_{\min}^*$ and the opening angle in the transverse plane, α .

5.3. Optimization of the Cut

In the previous Section, suitable variables for a cut on the track separation have been established. Now the cut values for $\Delta\eta$ and $\Delta\varphi_{\min}^*$ need to be determined. In order to perform a quantitative analysis of the region affected by two-track resolution effects, the observed inefficiency hole is fitted with a Gaussian function with negative amplitude in two dimensions. From this fit the width in $\Delta\eta$ and $\Delta\varphi_{\min}^*$ at the point where the function value is 5% below the average, is extracted, i.e. regions where the efficiency is below 95% are excluded. This is illustrated in Figure 5.10a. The extracted width is studied as a function of the transverse pair momentum k_T or the pseudorapidity η .

5.3.1. k_T Dependence

The extracted widths as a function of k_T are shown in Figure 5.10b. For global tracks, $R_{CA\varphi}$ is determined between 0 cm and 250 cm, while for TPC-only tracks it is determined between 80 cm and 250 cm, i.e. inside the TPC range. The comparison of the results from global tracks and TPC-only tracks shows that the obtained fit values are very similar. The different ranges in which the closest distance in φ is determined turn out to be equivalent. The obtained widths in $\Delta\eta$ are slightly

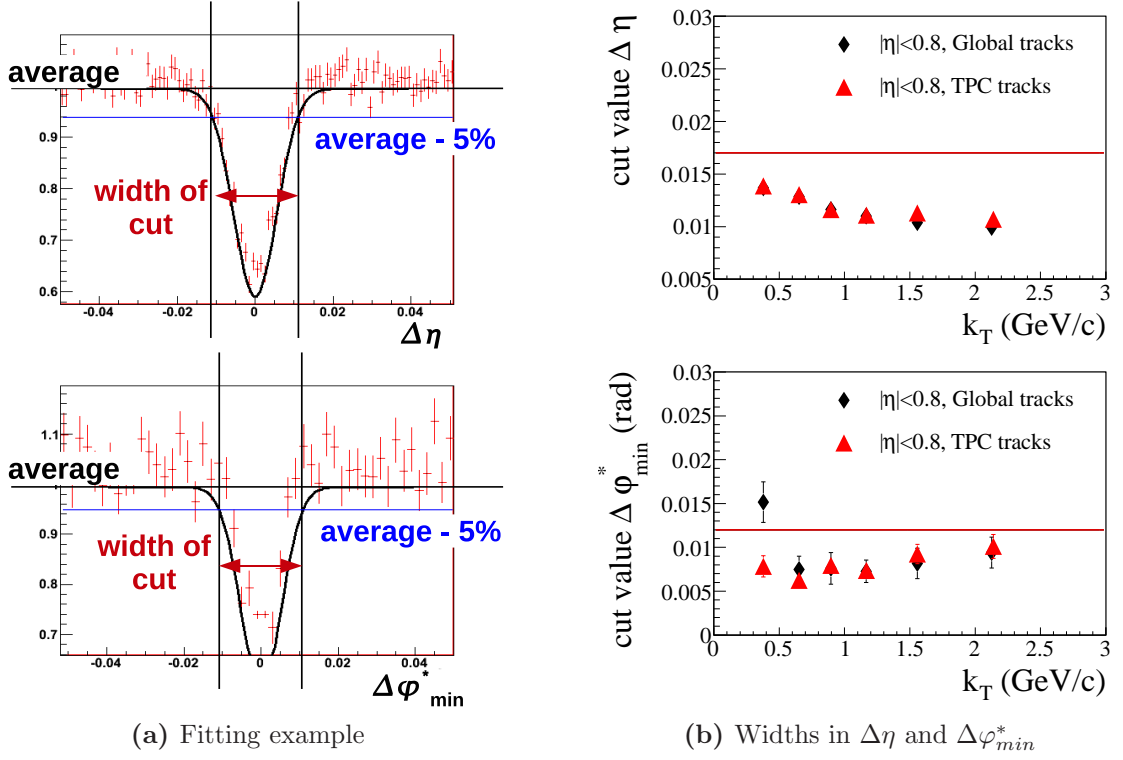


Figure 5.10.: a) Example of fit to the width at 5% below the average. b) Extracted widths of the inefficiency region for different k_T bins, obtained from a Gaussian fit in two dimensions to $(\Delta\eta, \Delta\varphi_{min}^*)$ for global tracks and to $(\Delta\eta, \Delta\varphi_{min}^*, TPC)$ for TPC-only tracks. The solid lines indicate the chosen cut values.

decreasing with k_T , but a cut value which is constant with k_T is easier to apply in practice. For safely excluding the affected region, the following cut values are chosen:

Tracks	$ \Delta\eta $	$ \Delta\varphi_{min}^* $
Global	> 0.017	> 0.012
TPC-only	> 0.017	> 0.012

Table 5.3.: Defined cut values.

5.3.2. Cross-check: Different Ranges for $R_{CA\varphi}$

In order to check whether the cut values depend on the radius where $\Delta\varphi^*$ becomes minimal, $R_{CA\varphi}$, the data are split up in samples of pairs with $R_{CA\varphi} = 0$ m, $0 \text{ m} \leq R_{CA\varphi} \leq 0.8$ m, $0.8 \text{ m} \leq R_{CA\varphi} \leq 2.5$ m, and $R_{CA\varphi} = 2.5$ m. The obtained widths are

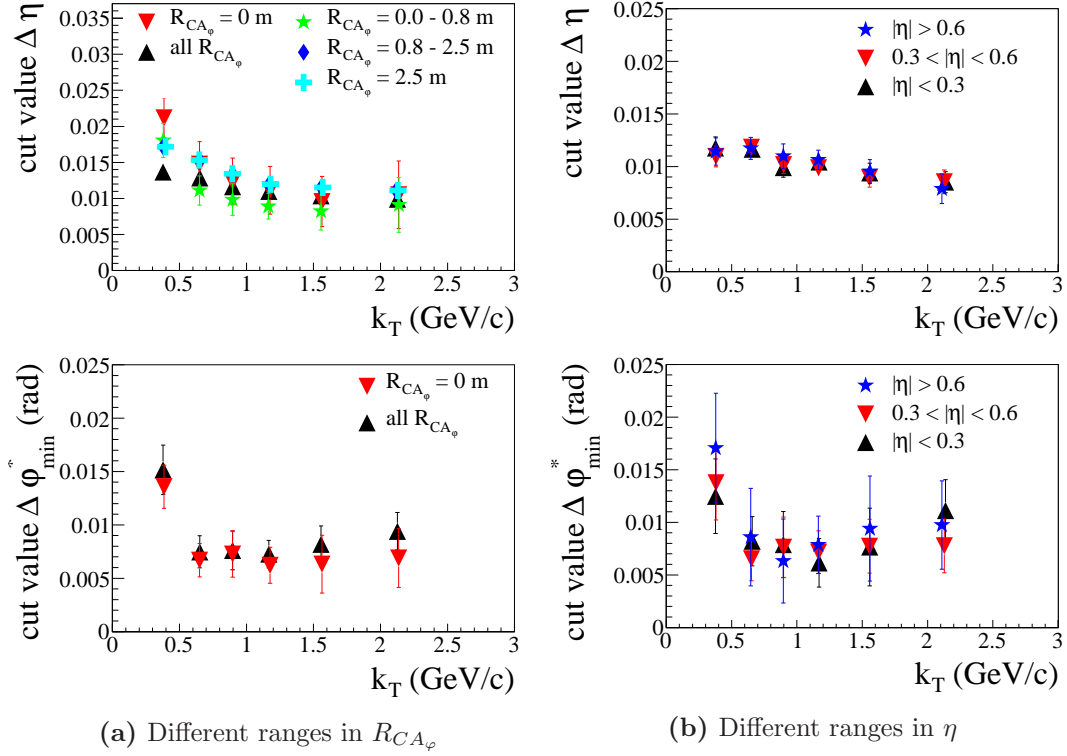


Figure 5.11.: Cut values for different k_T bins, obtained from a Gaussian fit in two dimensions to $(\Delta\eta, \Delta\varphi_{min}^*)$, (a) comparing results obtained from samples of pairs with different R_{CA_φ} and (b) within different η ranges (5.11b).

comparable, as can be seen in Figure 5.11a, although there are differences between the samples: for $0 \text{ m} < R_{CA_\varphi} < 2.5 \text{ m}$, $\Delta\varphi_{min}^*$ is 0 since the two tracks cross at R_{CA_φ} . For the ranges that are not shown in the plots, the observed inefficiency for the considered track type is so weak that the fit fails.

5.3.3. Cross-check: η Dependence

To study a possible pseudorapidity dependence of the widths of the inefficiency hole, the pairs are split up in samples within different η ranges: $|\eta| < 0.3$, $0.3 < |\eta| < 0.6$, $|\eta| > 0.6$. There is no strong dependence on η visible (Figure 5.11b). The behavior for TPC-only tracks is similar (Figure not shown).

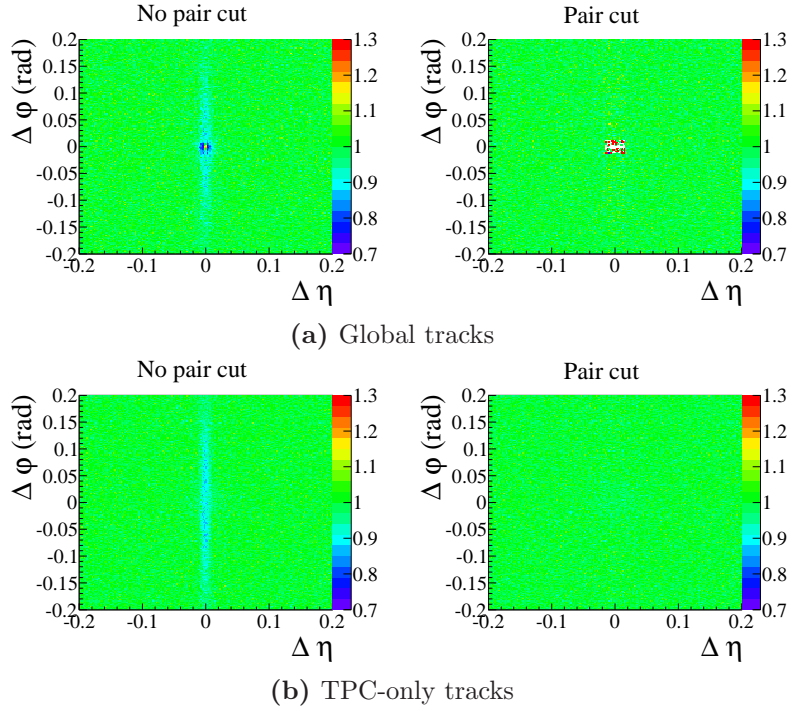


Figure 5.12.: Two-dimensional ratio in $(\Delta\eta, \Delta\varphi)$ with and without the pair cut applied for (a) global tracks and (b) TPC-only tracks.

5.3.4. Cross-check: $(\Delta\eta, \Delta\varphi)$ after Applying the Cut

Figure 5.12 shows the $(\Delta\eta, \Delta\varphi)$ plane with and without applying the cut. After the cut, the smeared inefficiency in $\Delta\varphi$ is gone, the ratio is flat at unity. For global tracks, the cut leads to a very underpopulated region (Figure 5.12a), for TPC-only tracks this is not the case (Figure 5.12b). This demonstrates a stronger connection of $\Delta\varphi$ and $\Delta\varphi_{min}^*$ in the case of global tracks due to *sailor* pairs where the two variables are equal as explained in Section 5.2.3.

5.4. Impact on HBT Analyses

The next step is to study the correlation function and check the influence of the cut on its properties. There is no Bose–Einstein correlation in Monte Carlo, hence an HBT peak is not observed in the sample. In order to verify the obtained fit results, a correlation is put in “by hand” by applying a Gaussian weight to the numerator pairs according to their relative momentum. The artificial HBT radius used here is 7 fm.

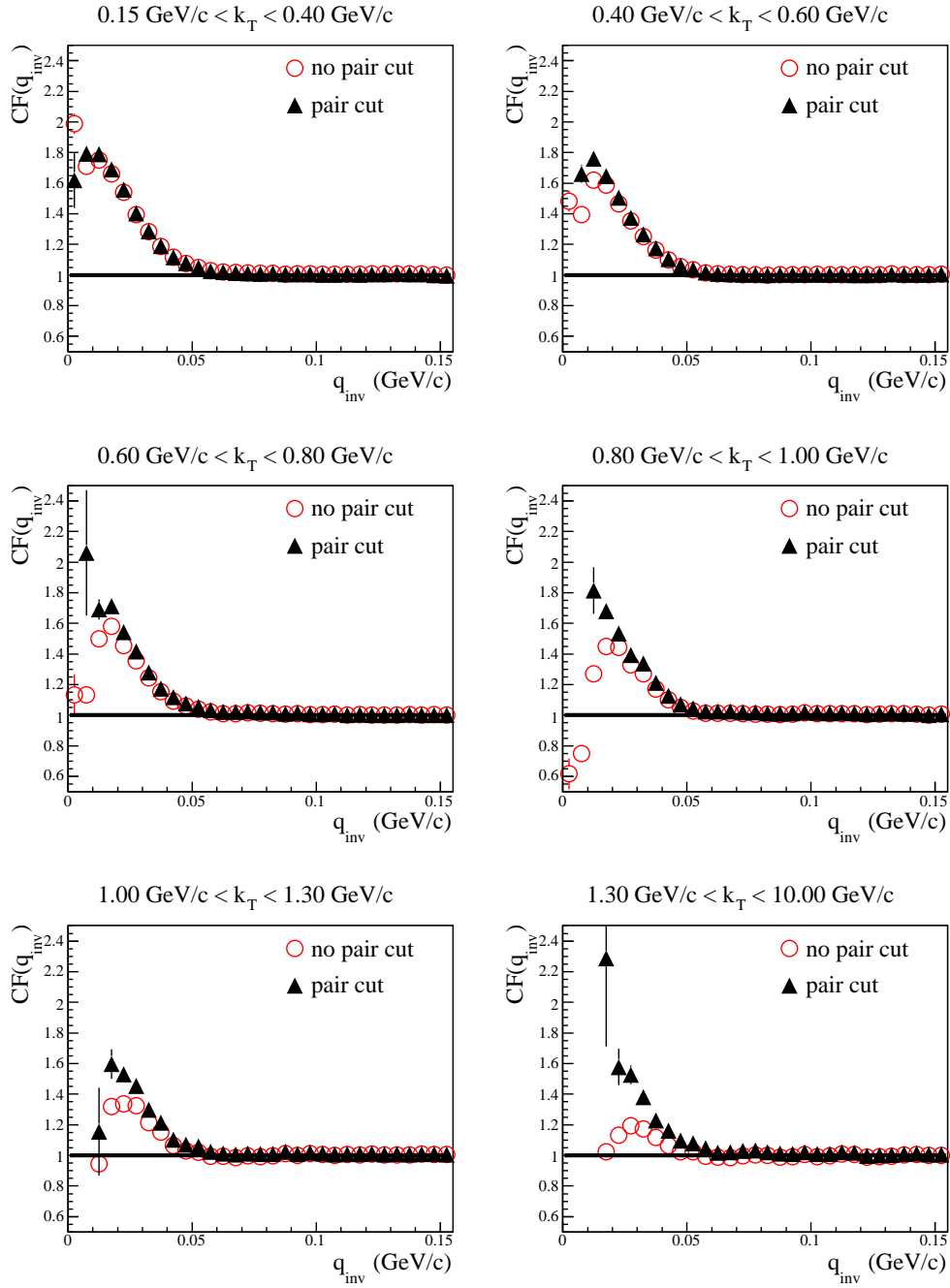


Figure 5.13.: Correlation functions for different k_T bins.

The two-track inefficiency is visible in the correlation function as a step fall at very small q_{inv} , which is observed by comparing the correlation functions with and without applying the cut (Figure 5.13).

5.4.1. Different k_T Ranges

By comparing different k_T bins, the previously mentioned observation that the effect of the two-track inefficiency is more pronounced for higher k_T is confirmed. The effect of the two-track reconstruction is almost completely removed from the correlation function for all k_T bins (Figure 5.13). The reason for the small remaining effect could be that a cut value constant in k_T is assumed. This would show up as a slightly better performance for higher k_T . Also, the cut values are extracted from the width of the inefficiency hole at 5% below the average. The remaining pairs could also lead to a small but visible effect.

5.4.2. Comparison of Cowboy and Sailor Pairs

A further cross-check is to separate pairs with different topologies. By comparing the correlation functions for *sailor* and *cowboy* pairs (see also Figure 5.14), it is seen that *cowboy* pairs are much more affected by two-track resolution effects than *sailor* ones. Since *cowboys* tend to continue propagating close to each other, this is expected. The two-track cut removes the difference, shown in Figure 5.15. The comparison is done in bins of k_T . The trends pointed out before are again visible: the two-track reconstruction effects are more pronounced for high transverse pair momenta and the cut removes the effect for all k_T ranges.

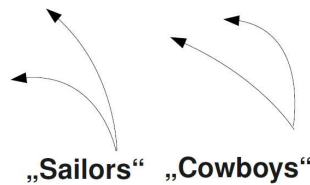


Figure 5.14.: Sketch for *cowboy* and *sailor* pairs.

5.4.3. Fit Results

To study the influence of the two-track effects on the observable to be measured, i.e. the HBT radii, the correlation functions are fitted with a Gaussian. The resulting HBT radii are shown in Figure 5.16. At high k_T one can see a clear drop of the radii below the correct input radius of 7 fm. The correct value is recovered when the cut is applied. For higher k_T values the Gaussian fit fails completely for *cowboy* pairs if no cut is applied. If the cut is applied, the values for *cowboy* and *sailor* pairs are consistent within the errors.

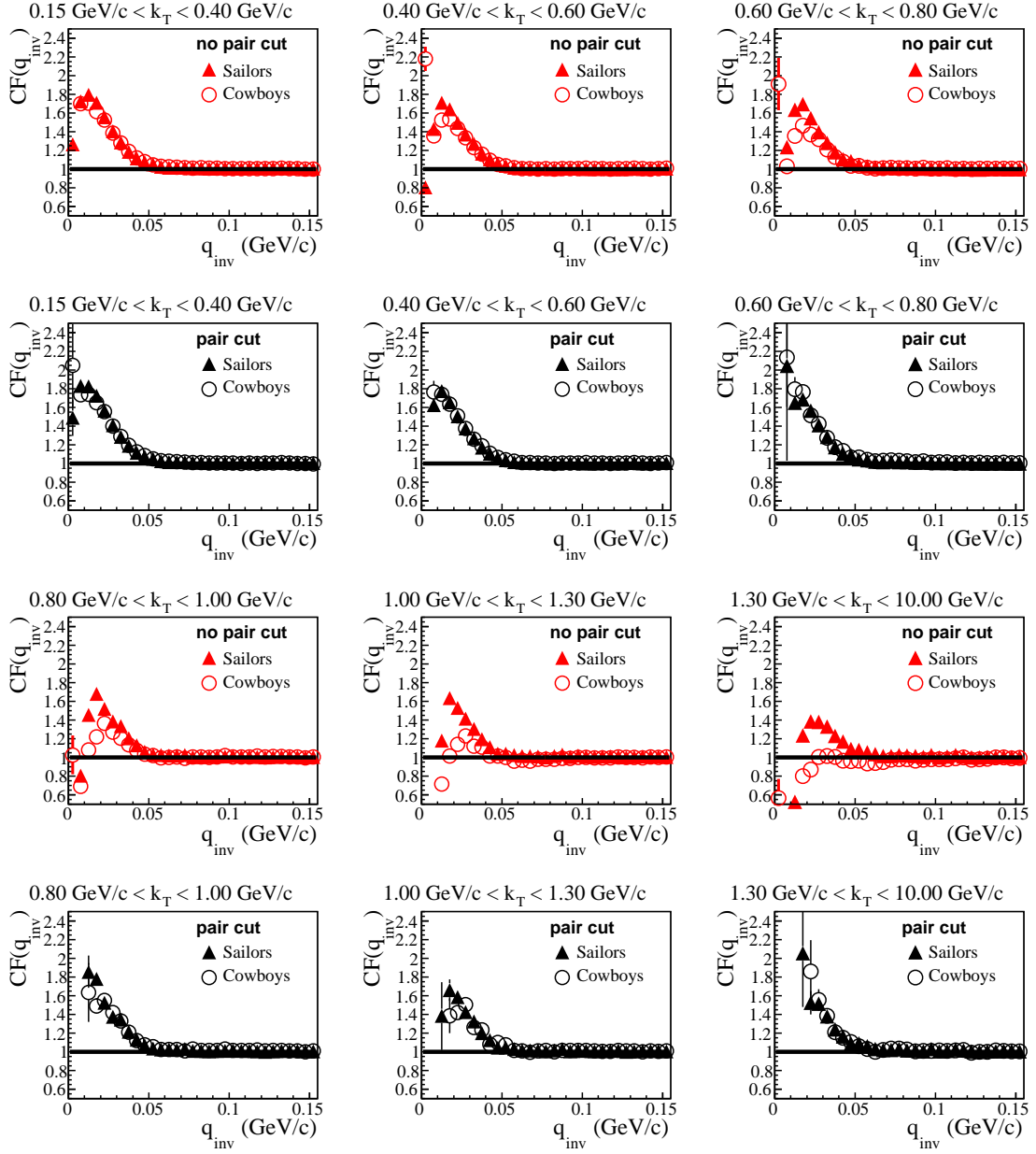


Figure 5.15.: Correlation functions for *cowboy* and *sailor* pairs in different k_T bins.

5.5. Summary

In the analysis of Bose–Einstein correlations via HBT interferometry, the source radii extracted from a fit to the correlation function are affected by two-track reconstruction effects, namely track splitting and track merging. The latter is found to be more important for high-energy Pb–Pb collisions at the LHC.

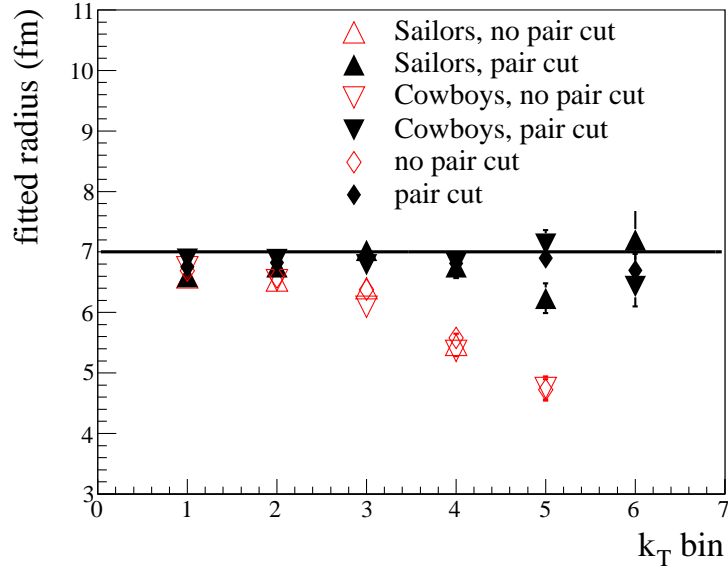


Figure 5.16.: HBT radii extracted from a fit to the correlation functions for *cowboy* and *sailor* pairs, with (black filled symbols) and without (red open symbols) a pair cut applied. The solid line indicates the input radius of 7 fm.

These effects have to be considered for pairs of tracks that are very close to each other in space and have a small momentum difference. This implies that these effects concern the most interesting region of the correlation function at small q_{inv} . A cut can be applied on the angular distance of the pair tracks to remove all pairs coming from the affected region. Since the correlation function is a ratio, the same cut applied on numerator and denominator removes the effect on the correlation function.

When looking at the angular distance it is important to consider the bending of the tracks in the transverse plane due to the magnetic field. The variable $\Delta\varphi_{min}^*$, defined as the angular distance at the closest approach of the tracks in φ , is introduced and leads to a well-defined inefficiency region in the $(\Delta\eta, \Delta\varphi_{min}^*)$ plane. Hence, these variables are used to define a suitable and effective cut.

Possible cut values are extracted from a two-dimensional Gaussian fit to the inefficiency region. The cut values show no strong dependence on the pseudorapidity of the pair or the radius at which $\Delta\varphi_{min}^*$ is calculated.

By applying this cut, the effect of the two-track inefficiency on the correlation function is almost completely removed. This is the case for the whole studied k_T range (0.15-10 GeV/c). A comparison of *cowboy* and *sailor* tracks confirms that the cut is

5. *Two-Track Resolution*

successful. The cut is validated on a Monte Carlo sample by extracting successfully a predefined HBT radius.

By implementing this cut, HBT analyses can be performed without being affected by two-track reconstruction effects in the extracted radii. For other physics analyses the cut range can be an indication of the kinematic region of affected pairs.

6. The Event Plane as Azimuthal Reference

When studying azimuthally sensitive HBT interferometry, information on the initial shape and the evolution of the source is obtained by extracting HBT radii from particles that are emitted in different directions in azimuth. A dependence of the radii on the azimuthal direction is expected from the almond-like shape of the overlapping region in non-central collisions. This shape is naturally connected to the direction of the impact parameter of the colliding nuclei. Since there is no preferred direction in the studied collisions, an isotropic distribution of the direction of the impact parameter in a sample of events is expected. When performing an analysis on many events, as it is necessary for an HBT analysis, all hints on the shape of the source region would average out and the analysis would not be meaningful. Therefore, azimuthally sensitive HBT interferometry is performed with respect to the so-called reaction plane.

Theoretically, the reaction plane is defined as the plane spanned by the impact parameter and the beam axis (Figure 6.1). Experimentally, there is no access to the direction of the impact parameter and therefore neither to the reaction plane, in case of a high-energy collider experiment. However, an event plane can be estimated which, in the ideal case, gives back the reaction plane. The initial geometrical anisotropy of the overlapping region translates into an asymmetry in the azimuthal particle distribution, which can be measured and used to estimate the reaction plane direction.

The estimated event plane can act as the reference in the azimuthal direction for the HBT analysis as well as for other analyses, e.g. to study variables in dependence on the path length which the particles traversed in the medium. As a part of this thesis, an analysis class was developed to provide information on the event plane orientation. This method enables different physics analyses to access the event plane information easily.

In this Chapter, the implementation of this analysis class in AliRoot and its default event and track selection are discussed. The performance of the implemented method is presented as a function of the event centrality. Furthermore, the results obtained by the implemented method are confronted with the reaction plane from Monte

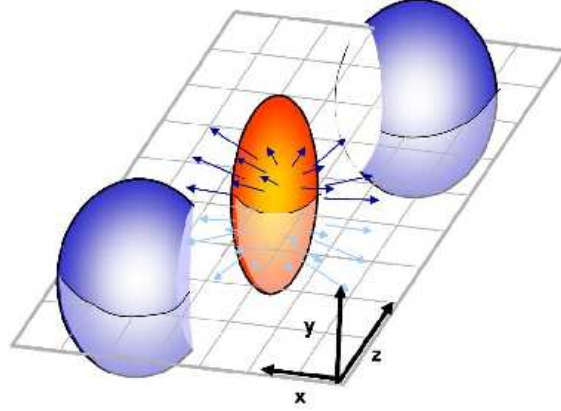


Figure 6.1.: Sketch of the reaction plane definition [56]: the colliding nuclei are shown in blue, the almond-shaped overlapping region in orange. The reaction plane is shown as the gray grid. The black arrows indicate the particle momenta.

Carlo. If an event is split up into sub-events, the measured sub-event event plane correlation can be used to calculate the achieved event plane resolution.

6.1. Event Plane Method

The diameter of the almond-like shaped overlapping region in non-central heavy ion collisions is small in the direction of the reaction plane and larger out-of-plane (Figure 6.1). This leads to a larger pressure gradient in-plane, causing a momentum anisotropy which leads to an asymmetric particle distribution in the transverse plane. Therefore, the azimuthal particle distribution can be used to estimate the initial collision geometry, i.e. the direction of the reaction plane. The azimuthal particle distribution with respect to the reaction plane can be decomposed in a Fourier series [57]:

$$E \frac{d^3 N}{d^3 p} = \frac{d^2 N}{2\pi p_T dp_T dy} \left(1 + \sum_{n=1}^{\infty} 2v_n \cos[n(\varphi - \Psi_{RP})] \right), \quad (6.1)$$

where N is the number of particles, p is the particle momentum, p_T the transverse momentum, φ is the particle emission angle, and Ψ_{RP} is the reaction plane angle. The coefficients v_n , which quantify the anisotropy of the particle distribution, are given by:

$$v_n = \langle \cos[n(\phi_i - \Psi_{RP})] \rangle, \quad (6.2)$$

where the angle brackets denote an average over all particles i in the event. In such an expansion, the mirror symmetry of the overlapping region with respect to the reaction plane does not allow sine terms. v_1 is known as directed flow, v_2 as elliptic flow, and v_3 as triangular flow; higher harmonics can be studied as well. In general, these coefficients depend on the considered transverse momentum p_T of the particles as well as on the considered rapidity range. The asymmetry of the initial geometry is of second order, i.e. the second order Fourier coefficient, the elliptic flow v_2 , is the coefficient that is directly sensitive to the almond-like shape of the overlapping region. It links the particle distribution, which can be measured, with the initial geometry of the source.

Experimentally, the *Event Plane Method* can then be used to estimate the reaction plane orientation from the azimuthal particle distribution [57]. This is done by creating an *Event Flow Vector*, the so-called Q -Vector, by summing over the emission angles, φ , of the particles:

$$\begin{aligned} Q_{n,x} &= \sum_i w_i \cos(n \cdot \varphi_i) = Q_n \cos(n \cdot \Psi_n), \\ Q_{n,y} &= \sum_i w_i \sin(n \cdot \varphi_i) = Q_n \sin(n \cdot \Psi_n). \end{aligned} \quad (6.3)$$

The event plane angle Ψ_n is then accordingly given by:

$$\Psi_n = \frac{1}{n} \cdot \arctan\left(\frac{Q_{n,y}}{Q_{n,x}}\right). \quad (6.4)$$

Here, n again indicates the order in the Fourier series. By referring to the connection of v_2 with the reaction plane direction, the second order event plane will be used in the following to approximate the reaction plane. In the ideal case, the weight w_i that appears in Equation (6.3) is v_n , the n^{th} order Fourier coefficient of the azimuthal particle distribution. This value is not known a priori and has to be approximated. The event plane method is by construction very sensitive to azimuthal differences in the detector efficiency. To avoid a bias, such differences have to be corrected (see Section 6.3.1).

6.1.1. Event Plane Resolution

The event plane estimate with the above procedure has a finite resolution \mathcal{R}_n [57]:

$$\mathcal{R}_n = \langle \cos[n(\Psi_n - \Psi_{RP})] \rangle. \quad (6.5)$$

This factor depends on the number of particles used for the Q -Vector calculation as well as on the average elliptic flow in the event. If the number of particles N , from which the Q -Vector is constructed, increases, the estimate of the reaction plane by the Event Plane Method is more precise and less sensitive to statistical fluctuations. For events with large elliptic flow, the resolution also improves, since the correlation of the particles with the reaction plane is larger and therefore the event plane extracted from the observed correlations is more precise.

Quantitatively, the so-called resolution parameter χ can be used to describe these dependencies:

$$\chi = v_n \sqrt{N}. \quad (6.6)$$

The event plane resolution is then given by [57]:

$$\mathcal{R}(\chi) = \frac{\sqrt{\pi}}{2} \chi \exp(-\chi^2/2) \left[I_0\left(\frac{\chi^2}{2}\right) + I_1\left(\frac{\chi^2}{2}\right) \right], \quad (6.7)$$

where I_0 and I_1 are modified Bessel functions.

Experimentally, the resolution can be evaluated by applying the event plane method on two sub-events and comparing the obtained results. The sub-events are constructed by dividing one event into two samples with equal multiplicities. They can be created in various ways: randomly, as a sample of positively charged particles and a sample of negatively charged particles, a sample of particles with positive or negative rapidity, and combinations of these approaches. Each method has its advantages and probes different systematic effects. In the following, tracks from the central barrel are assigned randomly to either one or the other sub-event. The advantage is that the method can be applied even for events with only a few particles. The disadvantage is that non-flow effects can contribute, which could be reduced by using sub-events, that are separated in rapidity and therefore are only correlated through long-range effects such as flow.

The event plane results from the sub-events are correlated with each other as well as with the true reaction plane. The strength of the correlation reflects the event plane resolution, which is given by [57]:

$$\mathcal{R}_{n,sub} = \sqrt{\langle \cos[n(\Psi_n^1 - \Psi_n^2)] \rangle}, \quad (6.8)$$

where Ψ_n^i is the sub-event event plane angle. Theoretically, the correlation of the results from sub-events can be described by [58]:

$$\begin{aligned} \frac{dN}{d\theta_{\Delta EP}} = \frac{1}{2} \exp \frac{\chi^2}{2} \left\{ \frac{2}{\pi} \left(1 + \frac{\chi^2}{2} \right) + \frac{\chi^2}{2} \cos 2\theta_{\Delta EP} \left[I_0 \left(\frac{\chi^2}{2} \cos 2\theta_{\Delta EP} \right) \right. \right. \\ \left. \left. + L_0 \left(\frac{\chi^2}{2} \cos 2\theta_{\Delta EP} \right) \right] + \frac{\chi^2}{2} \left[I_1 \left(\frac{\chi^2}{2} \cos 2\theta_{\Delta EP} \right) + L_1 \left(\frac{\chi^2}{2} \cos 2\theta_{\Delta EP} \right) \right] \right\}, \end{aligned} \quad (6.9)$$

where $\theta_{\Delta EP}$ denotes the difference between the sub-event event plane angles, I_0 and I_1 are modified Bessel functions and L_0 and L_1 are modified Struve functions.

Fitting the experimental distribution of the event plane angle difference with Equation (6.9) allows to extract the corresponding resolution parameter χ_{sub} . The resolution parameter of the full event is then given by $\chi_{full} = \sqrt{2}\chi_{sub}$, according to Equation (6.6). With this, the resolution of the event plane from the full event can be calculated via Equation (6.7).

6.2. The Analysis Framework

To provide a common framework for the event plane determination inside AliRoot, independent of analysis-specific code, two new classes were developed:

`AliEPSelectionTask`, where the actual calculation of the Q -Vector from the events and the sub-events is performed, and `AliEventplane`, in which the results are stored.

The main features of this framework are the following: first, it enables convenient access to the event plane information inside the user analysis. Second, “default” event plane information is defined as a common reference. Third, the framework also provides the possibility to calculate customized event plane information in order to check for systematic effects on the user analysis, i.e. it allows an easy modification of the default cuts and settings. The framework can be extended in the future, to also include information from other detectors, etc.

6.2.1. Analysis Procedure

In the first iteration the `AliEPSelectionTask` is used to create a φ distribution, necessary for the detector efficiency corrections in azimuth. The φ distributions for several run ranges are stored in an `AliOADBContainer`, from where they can be accessed. The `AliOADBContainer` is an AliRoot class that is responsible for storing analysis-relevant information collected during the reconstruction or later on, e.g. available trigger classes and centrality calibration files. The `AliOADBContainer` provides the correct φ distribution for the current run and since it is a part of AliRoot, it can be accessed by every user.

In the second iteration, the `AliEPSelectionTask` calculates and stores the event plane information and creates control histograms that monitor its performance. It corrects for the efficiency differences in φ using the φ distribution from the first iteration. The calculated Q -Vector, the event plane angle, the Q -Vectors for the sub-events, and the difference of the sub-event event plane angles are members of `AliEventplane`. Furthermore, some physics analyses require a correction for

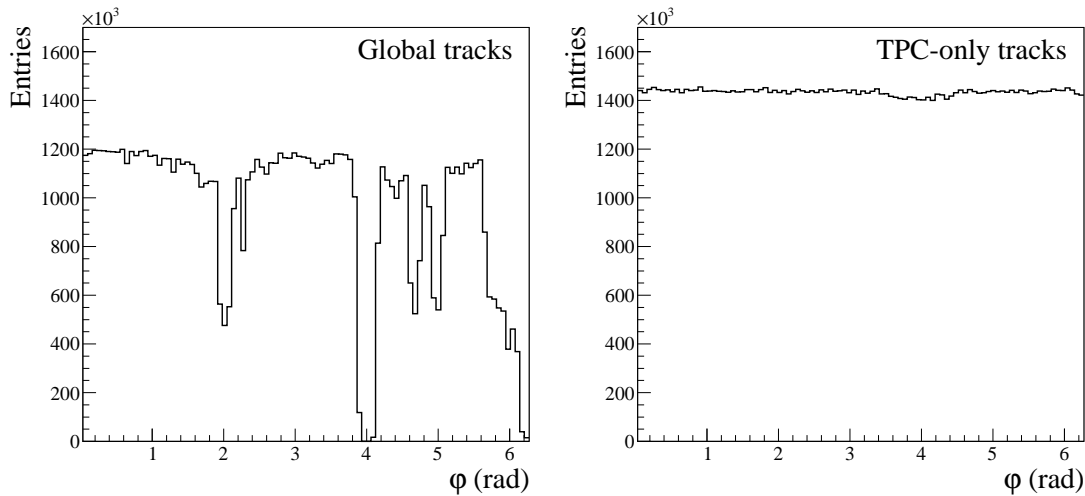


Figure 6.2.: ϕ distribution for global tracks (left) and TPC-only tracks (right), for 240k Pb–Pb events at $\sqrt{s_{NN}} = 2.76$ TeV.

autocorrelations and need to subtract the Q -Vector contribution of the track that is analyzed. To enable such a correction, the Q -Vector contribution of each track is kept as an array in the `AliEventplane`.

This class, `AliEventplane`, is then stored in the `AliESDEvent` and the `AliAODHeader` from where it can be accessed via ESD's and AOD's by the user analysis.

6.2.2. Event and Track Selection

The framework calculates the event plane information for every event that contains more than 4 good tracks. The requirement of a certain number of good tracks is needed, otherwise the sub-events would be empty or would only contain a single track in which case a Q -Vector calculation does not lead to a meaningful result. In practice, this requirement does not have a large impact on the user analysis since the centrality range above 88% is generally excluded due to an incomplete understanding of possible electromagnetic interactions occurring in this regime. Thus, in practice, this cut does not exclude any events since events with a centrality above 88% contain more than 4 good tracks.

As already mentioned, the event plane method is by construction very sensitive to azimuthal efficiency and acceptance differences. A flat distribution of tracks in ϕ is essential. In Figure 6.2 a comparison of tracks that are reconstructed by TPC information only and global tracks that are reconstructed combining information from many detectors are shown for 240k Pb–Pb events at $\sqrt{s_{NN}} = 2.76$ TeV. Since there are major acceptance holes in the SPD, the ϕ distribution of globally reconstructed

Cut Variable	Cut Value
Number of reconstructed TPC clusters	> 50
χ^2 per TPC cluster	< 4
Distance of closest approach to primary vertex in z	< 3.2 cm
Distance of closest approach to primary vertex in x and y	< 2.4 cm
Kink rejection	active

Table 6.1.: Default track cuts applied in the `AliEPSelectionTask`.

tracks in azimuth is not uniform. The TPC-only tracks show a uniform distribution in φ with only small systematic deviations of the order of 1%. Therefore, the default track selection uses TPC-only tracks. However, the `AliEPSelectionTask` provides an option where global tracks can be used for the event plane determination. In this case the φ correction (explained in Section 6.3.1) is crucial.

TPC-only tracks are selected according to the standard track cuts listed in Table 6.1. Additionally, the η range is restricted to $|\eta| < 0.8$, which is the range where the ALICE detector has full coverage. Only particles with $0.15 \text{ GeV}/c < p_T < 20 \text{ GeV}/c$ are considered since particles with smaller p_T do not reach the TPC and the fake track rate for TPC-only tracks increases at high p_T .

6.3. Performance

In order to monitor the performance of the `AliEPSelectionTask`, control histograms are produced automatically. The performance depends strongly on the applied corrections and weighting procedures, as well as on the considered centrality range, as it is described in the following.

6.3.1. φ Correction

Figure 6.3 shows the effect of the non-uniformity of the detector efficiency in φ on the Ψ_{EP} distribution, which should be flat in the ideal case. In Figure 6.3a the φ distribution of TPC-only tracks is shown. It is not completely uniform, the deviation from the average is around 0.7%. This translates into a deviation from the average in the Ψ_{EP} distribution of about 2%, shown in Figure 6.3c. Hence, even though the efficiency differences in azimuth are small, they affect the event plane results.

As discussed before, a correction procedure has to be applied in order to account for the non-uniform detector efficiency in azimuth. The procedure requires a φ distribution of the tracks which are used for the event plane determination. This

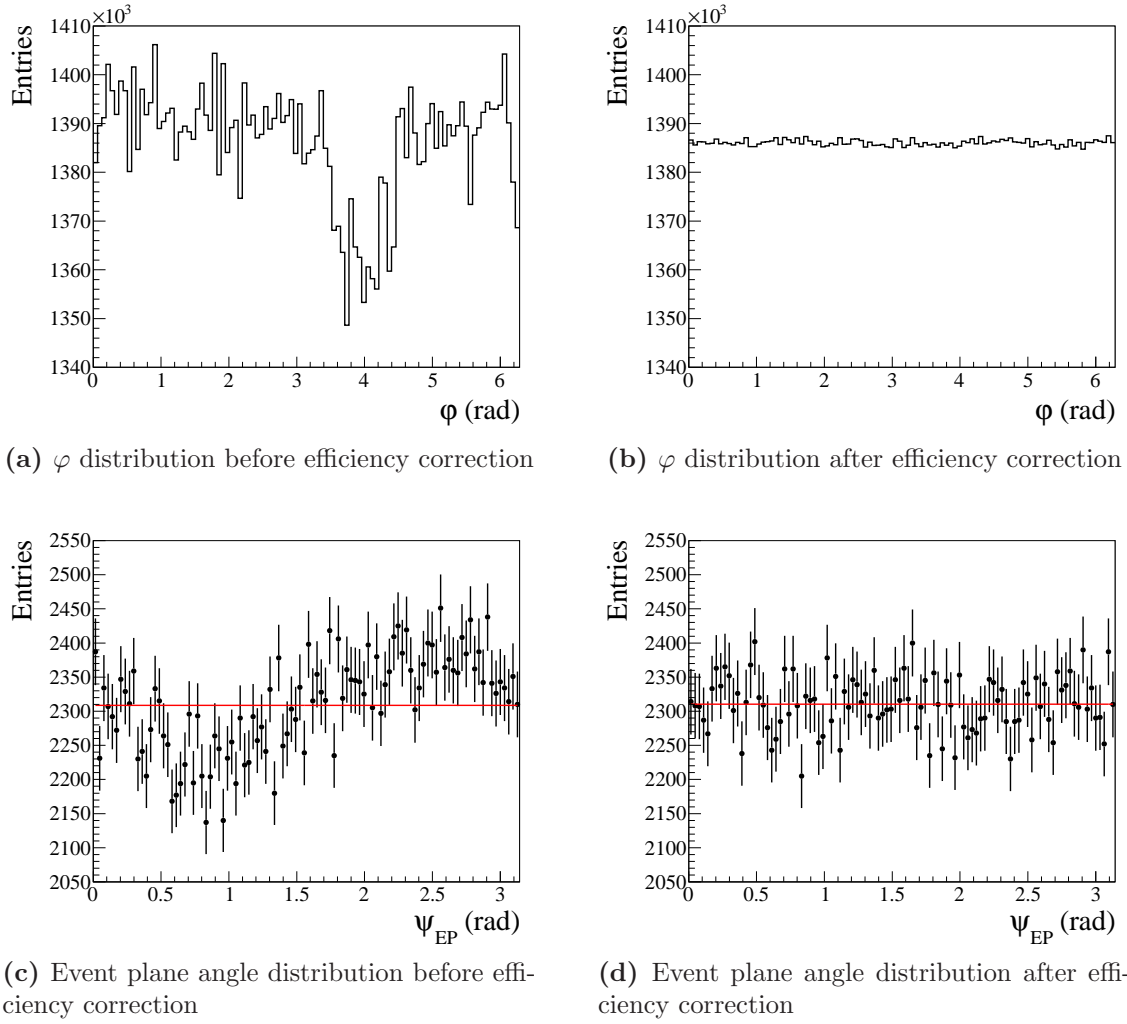


Figure 6.3.: Comparison of φ and event plane angle (Ψ_{EP}) distributions before and after applying the correction for efficiency differences in azimuth.

distribution is inverted and the values are used as bin-wise weights for the particles out of which the Q -Vector is calculated. In principle, the efficiency could also depend on the p_T of the particle and on the event centrality. These effects are found to be small and can be neglected. The same track cuts have to be applied for determining the φ distribution and for the Q -Vector calculation, since different cuts can lead to differences in the φ distribution. The detector effects causing a non-uniform φ distribution do not depend on a particular run. Several runs that were taken under similar conditions and in which the detector efficiency is equal can be grouped together. It is sufficient to create a φ distribution for each such run range and correct every run within the range with the same distribution. The advantage is that then the correction φ distribution contains higher statistics.

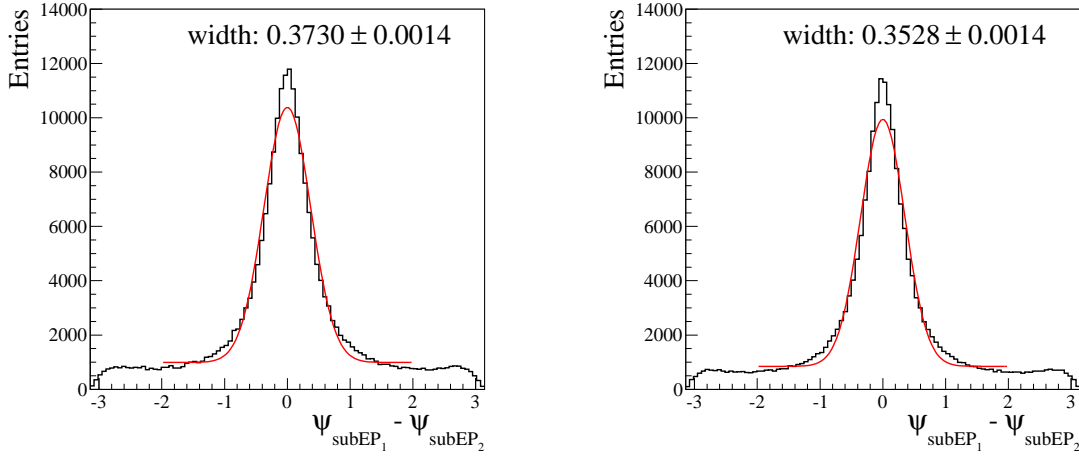


Figure 6.4.: Difference of Ψ_{subEP} without (left) and with (right) p_T weights applied. The width is extracted with a Gaussian fit to the distribution (red curve).

After the efficiency correction, the structures in the φ distribution are not visible anymore (Figure 6.3b) and the event plane distribution is flat as well (Figure 6.3d). The correction procedure is efficient to remove the bias on the event plane angle.

6.3.2. p_T Weights

As discussed in Section 6.1, the track contribution to the Q -Vector should be weighed with the elliptic flow, v_2 , of the track particle. This value is a priori not known and has to be approximated, e.g. by the transverse momentum p_T of the particle since the flow value v_2 was found to rise linearly with p_T up to about 2 GeV/c. Therefore, the p_T of the particles is used as a weight up to 2 GeV/c in the following. For particles with higher transverse momenta a constant weight of 2 is taken since the elliptic flow is found to be only weakly dependent on p_T above 2 GeV/c in ALICE [16].

The usage of p_T weights improves the event plane resolution significantly, as shown in Figure 6.4, where the comparison of the Ψ_{subEP} difference applying and not applying the weights is displayed. The widths quoted in both plots are extracted by a Gaussian fit. Although a Gaussian can not give a perfect description of the functional form of the Ψ_{subEP} difference, it can reflect the width of the observed peak which is connected to the event plane resolution.

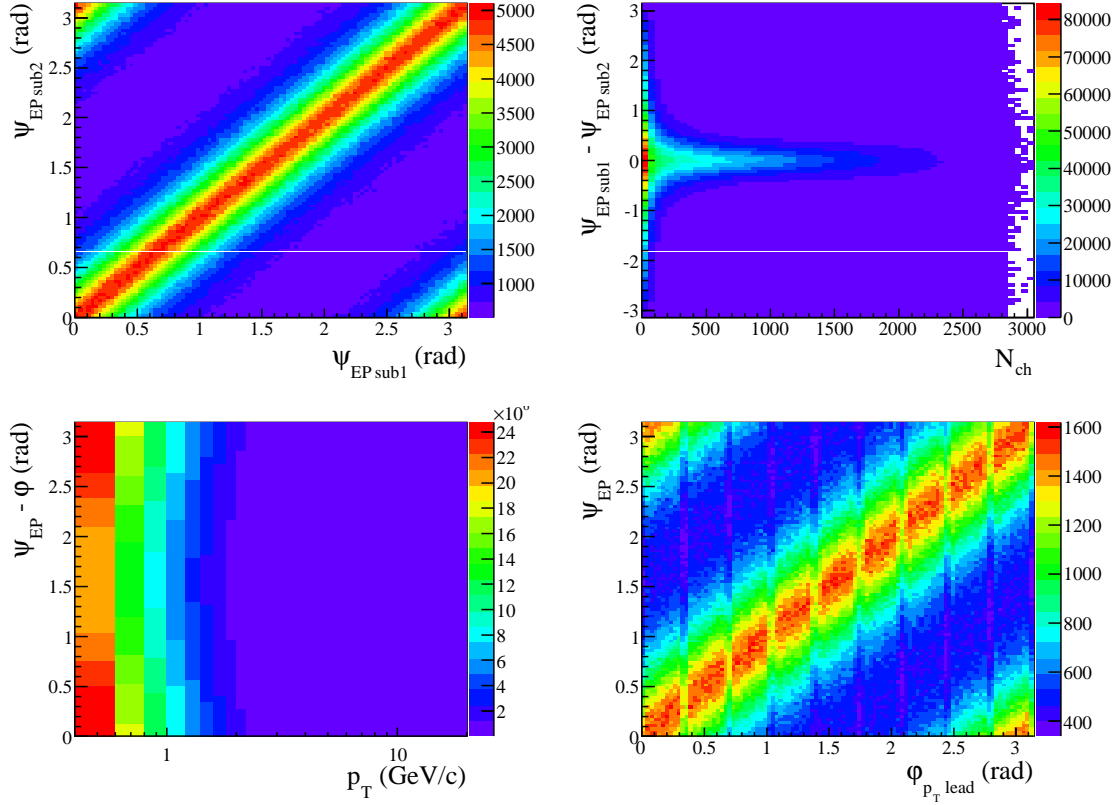


Figure 6.5.: Control histograms produced by the AliEPSelectionTask.

6.3.3. Control Histograms

Apart from a φ distribution and an Ψ_{EP} distribution, the AliEPSelectionTask creates the following control histograms:

- Event plane angle from sub-event 1 (Ψ_{EPsub1}) versus event plane angle from sub-event 2 (Ψ_{EPsub2}).
- Difference of Ψ_{EPsub1} and Ψ_{EPsub2} in dependence on the event multiplicity.
- Difference of the particle emission angle and the event plane angle in dependence on the transverse momentum p_T .
- Emission angle of the particle with the leading p_T versus the event plane angle.

Examples of these control plots are shown in Figure 6.5. These were obtained by analyzing 16.4 million Pb–Pb events at $\sqrt{s_{NN}} = 2.76$ TeV.

The event plane angles obtained from different sub-events (Figure 6.5, upper left plot) show a strong correlation. It is also visible that the method is not sensitive to

differences of π , since the second order event plane does not contain the direction of the Q -Vector but only its orientation. The difference of the Ψ_{subEP} (Figure 6.5, upper right plot) is small and shows a dependence on the measured number of charged particles in the event. The difference is rapidly getting smaller with increasing number of charged particles from low multiplicities up to $N_{ch} = 300$ and then reduces slowly further up to $N_{ch} = 1000$. At higher multiplicities, no clear trend is visible.

The comparison of the event plane angle and the emission angles of the particles with respect to their p_T (Figure 6.5, lower left plot) shows that more particles are emitted in-plane than out-of-plane, as expected. This is true for the whole p_T range which is a hint that the event plane angle is not highly dominated by high- p_T objects. This is further confirmed by the correlation of the emission angle of the particle with leading p_T and the event plane angle (Figure 6.5, lower right plot) which is visible but not as strong as the Ψ_{subEP} correlation. The structure visible in the emission angle of the leading p_T particle reflects the geometry of the TPC. On the borders of two TPC sectors track points cannot be reconstructed leading to the observed “gap” structure. The TPC has 18 sectors in total, since the measurement is projected on $0-\pi$ nine “gaps” are visible. Since low p_T particles are bent stronger in the magnetic field they have enough reconstruction points outside the border region, whereas high p_T tracks are almost straight and can have most of their points in the sector border. Therefore, this effect is only relevant for high p_T particles and not visible in the previous plots. For the event plane determination, this does not play a role, since it is an effect of a higher order in the Fourier series, so the event plane method using the second order Q -Vector as an estimate is not sensitive to it.

6.3.4. Centrality Dependence

The performance of the `AliEPSelectionTask` depends on the strength of the elliptic flow in the analyzed events as explained in Section 6.1. The elliptic flow depends on the event centrality: it is small for central events, then it rises and decreases again towards peripheral events.

The overall behavior of the Ψ_{EP} distribution as a function of centrality is shown on the left side in Figure 6.6. The variation is small and the performance is relatively uniform over all centralities. The right plot of Figure 6.6 is similar to the control histogram, where the event plane difference is shown in dependence of the event multiplicity (upper right panel in Figure 6.5). Here, the event plane difference is plotted versus centrality, the two plots are comparable. In Figure 6.6 finer structures become visible since it is plotted without the very low multiplicity events that otherwise dominate. In this case, not only a broadening for very peripheral events is observed but also for very central events, as is expected due to smaller elliptic flow.

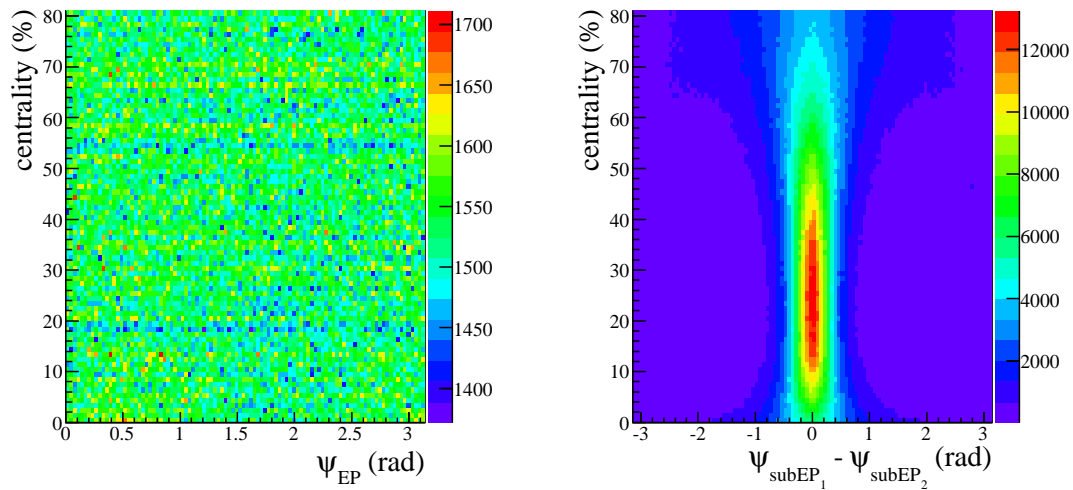


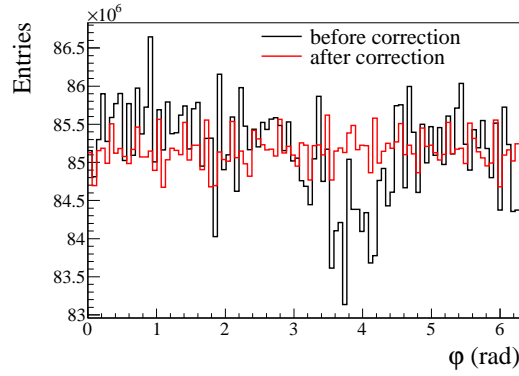
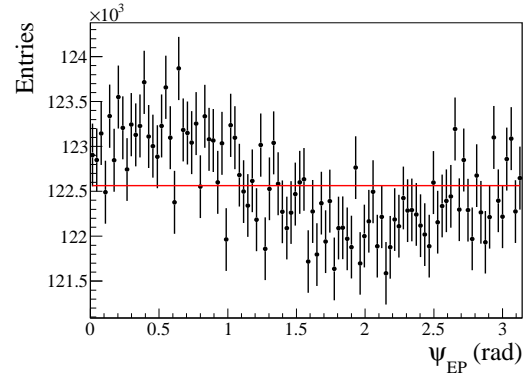
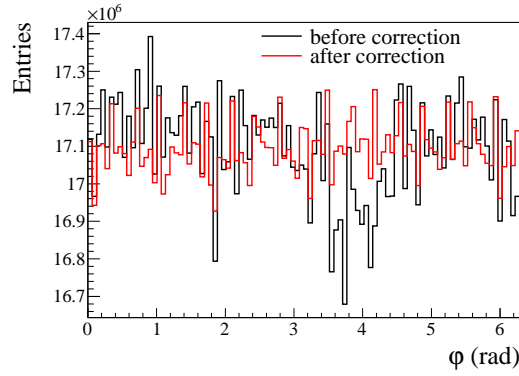
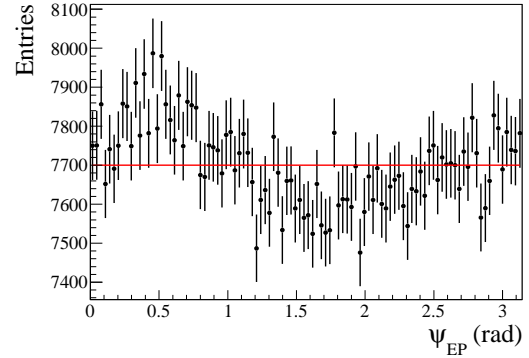
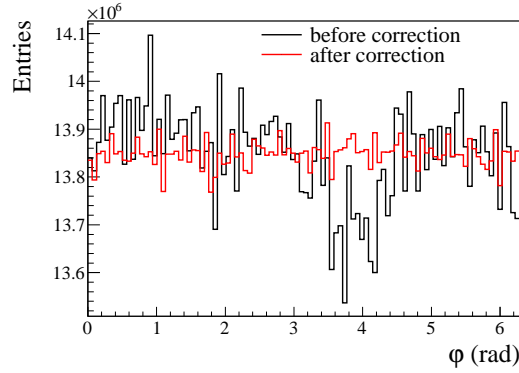
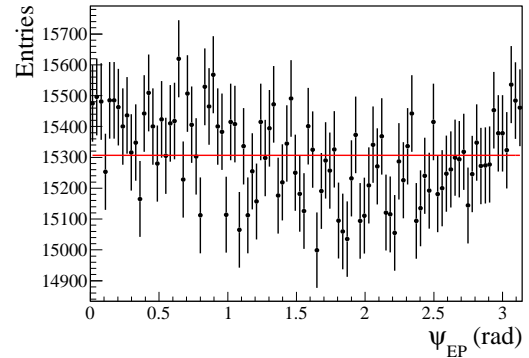
Figure 6.6.: Centrality dependence of Ψ_{EP} distribution (left) and Ψ_{subEP} difference (right).

This centrality dependence is also reflected in the distribution of the event plane angles, shown in Figure 6.7. While the φ distributions look very similar for the different centrality ranges (Figures 6.7a, 6.7c, 6.7e), the Ψ_{EP} distributions are quite different (Figures 6.7b, 6.7d, 6.7f). In the ideal case, the distribution should be flat. For 0-80% centrality (Figure 6.7b) and the 5% most central events (Figure 6.7d) a structure is seen in the distribution. The deviation from the average is up to 0.5% for events with centrality 0-80% (Figure 6.7b) and up to 1.5% for events with centrality 0-5% (Figure 6.7d). For events with 20-30% centrality there is almost no structure remaining (Figure 6.7f). This is also reflected in the quality of a linear fit to the distributions. The reason for the appearing structures in the Ψ_{EP} distribution are non-flow effects dominating over the weak flow in central or very peripheral events, leading to a bias in the event plane determination.

6.4. Monte Carlo Comparison

In order to validate the results from the `AliEPSelectionTask`, the event plane angle obtained from the task is compared with the true reaction plane from Monte Carlo. Only some Monte Carlo generators provide the reaction plane information. Here, the thermal heavy-ion generator Therminator [31] was used to create a sample of events from which 3800 events with 0-5% centrality and 3700 events with 20-30% centrality were included in this analysis.

In Figure 6.8 the correlation of the true reaction plane angle with the experimentally determined event plane angle is shown. Note, that neither p_T weights nor

(a) φ distribution, 0-80% centrality(b) Ψ_{EP} distribution, 0-80% centrality(c) φ distribution, 0-5% centrality(d) Ψ_{EP} distribution, 0-5% centrality(e) φ distribution, 20-30% centrality(f) Ψ_{EP} distribution, 20-30% centrality**Figure 6.7.:** φ and Ψ_{EP} distributions for different centrality ranges.

φ corrections are applied for the experimental method here. The results therefore represent a lower limit for the performance of the `AliEPSelectionTask` including all corrections and weights. For very central events the true and the experimental

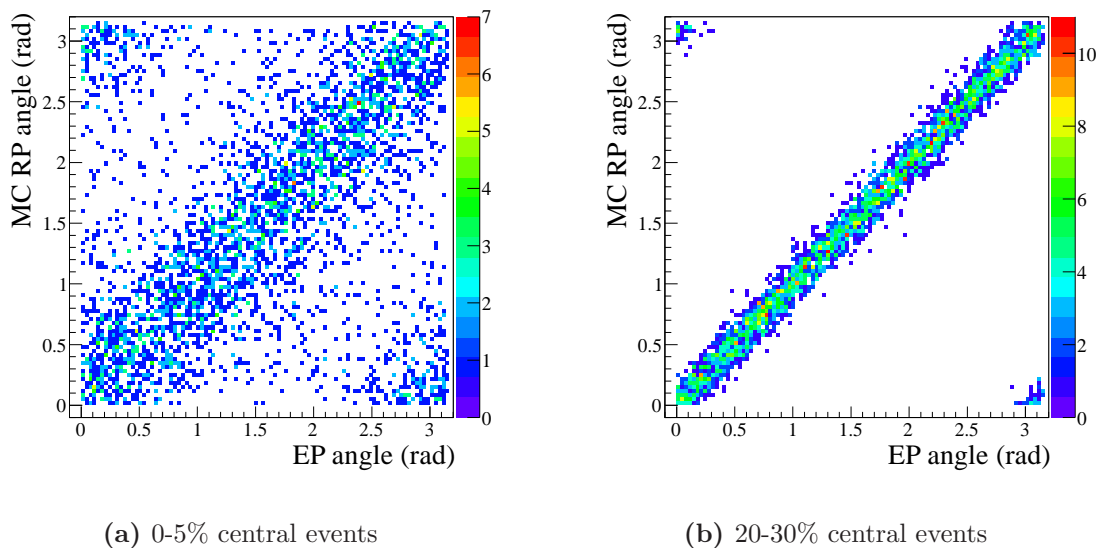


Figure 6.8.: Correlation of Monte Carlo reaction plane angle and event plane angle for 0-5% and 20-30% central events using TPC-only tracks.

results are not as strongly correlated as for events with centrality 20-30%, for which the correlation is very clear. This is expected from the centrality dependence of v_2 .

6.5. Event Plane Resolution

The results measured for the sub-event event plane difference (Figure 6.9) can be confronted with the introduced theoretical description (Equation (6.9)). In Figure 6.9, the colored curves correspond to different values for the resolution parameter and therefore reflect several flow strengths (see Equation (6.6)). The black curves represent the function where the value for the resolution parameter is fitted to the data.

The overall agreement between the fits and the data is reasonably good. For 0-5% centrality (Figure 6.9b) the resolution parameter is found to be relatively small ($\chi = 1.49$), whereas for 20-30% centrality (Figure 6.9c) a higher value is needed to describe the observed correlation correctly ($\chi = 2.64$), as expected from the centrality dependence of flow. For the 0-80% centrality bin the situation is different (Figure 6.9a): none of the curves fits the data very well. It seems as if a superposition of several curves can give a good description. This is expected, since the centrality range is quite large, so samples with different flow values are superimposed.

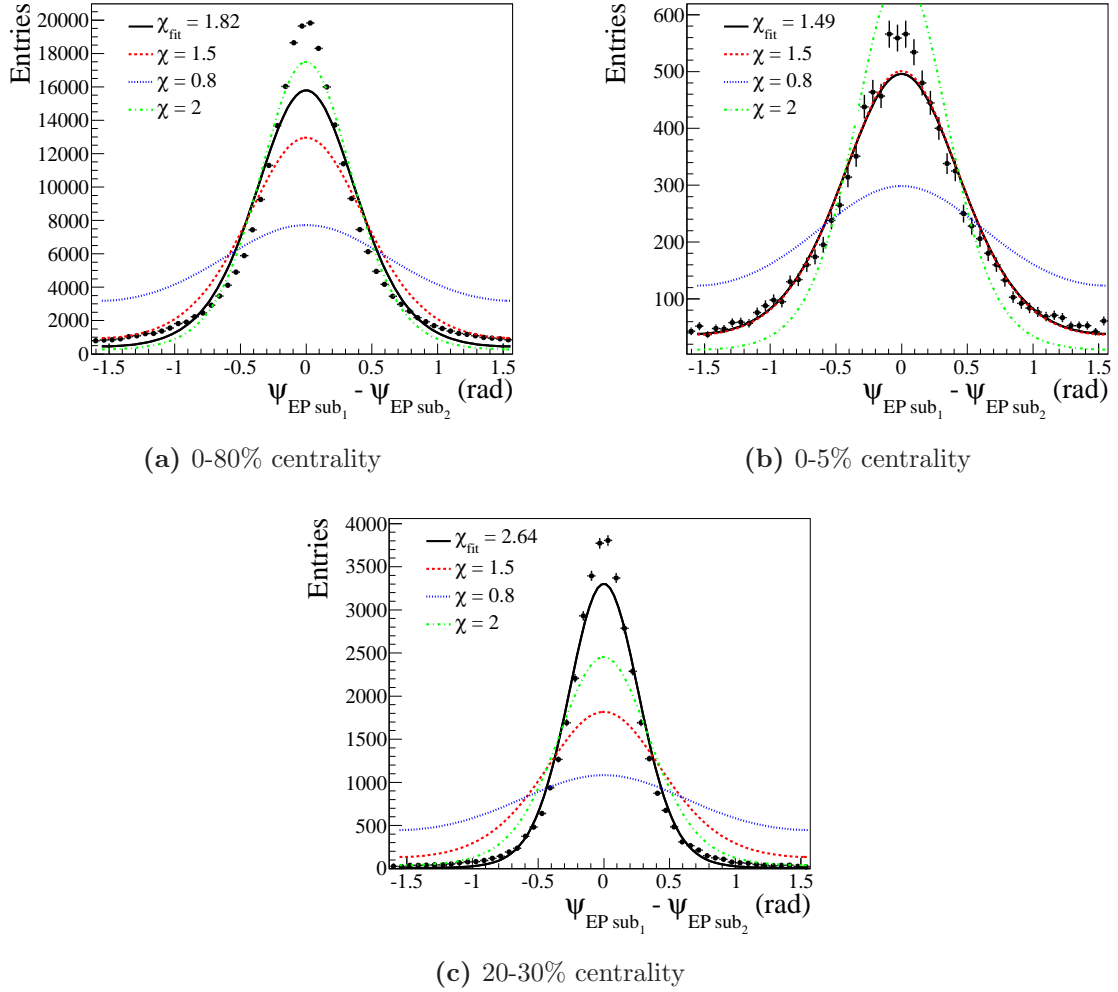


Figure 6.9.: Comparison of Ψ_{subEP} differences for different centrality bins with the theoretical description of the functional form.

The deviation around the peak can originate in flow fluctuations which are present in the data but are not taken into account in the theoretical description. Similar to the discussion of the 0-80% centrality bin, each bin contains events with a bit larger or a bit smaller flow values, and all events for one bin are plotted together. This can slightly change the shape of the correlation. The effect is small and mostly visible in the peak region, where small deviations in the flow strength lead to large differences in the observed correlation.

From the resolution parameter extracted from the fit the resolutions can be calculated via Equation (6.7), the results are shown in Figure 6.10. The trend behaves as expected from the centrality dependence of the elliptic flow and the change in multiplicity. The resolution is above 0.85 for all studied centrality ranges. In con-

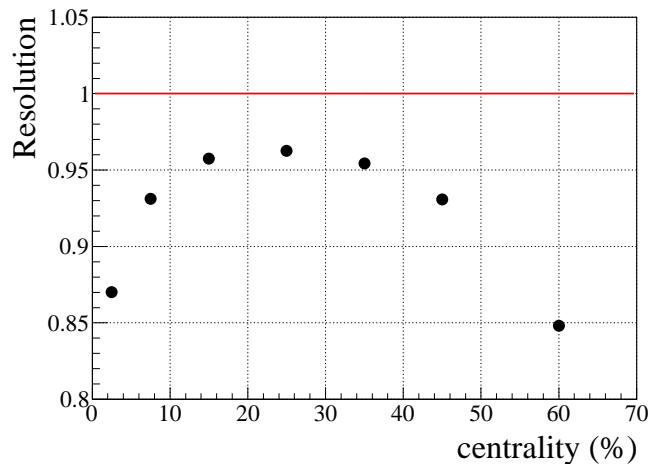


Figure 6.10.: Centrality dependence of the measured event plane resolution.

trast, the achieved resolution at RHIC is around 0.7 [59]. The difference can be understood, since the multiplicities are larger and the particles have larger flow at LHC compared to RHIC.

6.6. Summary

The reaction plane, defined as the plane spanned by the beam axis and the impact parameter of the collision is used to describe the collision geometry. Since the initial spatial geometry causes an asymmetry in momentum space and therefore in the azimuthal particle distribution, the latter can be studied experimentally (Event Plane Method) and used to estimate the reaction plane orientation. The second order event plane is a good reaction plane estimate in practice.

An analysis framework has been developed which provides event plane information to user analyses in ALICE. The framework consists of two classes: `AliEPSelectionTask` and `AliEventplane`. The user can personalize the information easily and customize event and track selection. Thus, every user can study event plane dependent observables in a uniform way. For the default event plane determination, TPC-only tracks are used. A correction for efficiency variations in azimuth is applied, as well as a weighting procedure, where the actual flow value, occurring as a weight in the Q -Vector calculation, is approximated by the particle p_T . These corrections clearly improve the obtained results.

The performance of the event plane determination depends on the studied centrality range as expected from the centrality dependence of elliptic flow. The results show

no strong dependence on the direction of the leading p_T particle, which is a hint that jet-like correlations are not dominant.

A comparison with Monte Carlo validates the obtained results. The theoretical description of the sub-event event plane correlation matches the results from the `AliEPSelectionTask` very well and allows to calculate the achieved event plane resolution. It is found to be between 0.85 and 0.95.

The presented code is included in AliRoot and is used for the azimuthally sensitive HBT interferometry analysis that is presented in Chapter 7.

7. Azimuthally Sensitive HBT Interferometry

HBT interferometry allows to extract the size of the emitting source in space-time (see Chapter 4). Performing the analysis in three dimensions provides information on the source size in different directions. This can be used to determine the shape of the source in addition to its size.

The freeze-out source shape is naturally connected to the initial geometry of the overlapping region. Since the initial spatial asymmetry of the source in non-central collisions causes an anisotropy in momentum space (elliptic flow, v_2), the initial anisotropy in space-time is reduced during the evolution of the fireball. This reduction and therefore the actual freeze-out source shape depends on the pressure gradients inside the fireball as well as on its lifetime. This means that a measurement of the source shape at freeze-out is sensitive to the initial geometry as well as to the details of the hydrodynamic evolution of the source.

The combination of elliptic flow measurements which probe the initial-state properties in momentum space and azimuthally sensitive HBT interferometry which probes the final-state properties at freeze-out can give a detailed picture of lifetime, pressure gradients, temperature and the Equation of State of the source (see also Figure 7.1). The study of the source shape is especially interesting at LHC energies, since the large elliptic flow could lead to a freeze-out source shape that is no longer extended out-of-plane but extended in the direction of the event plane in the case of a long-living system, according to hydrodynamic calculations (Figure 7.2).

Experimentally, the azimuthally sensitive HBT interferometry analysis can be performed by extracting the HBT radii parameters, as it is described in Chapter 4, in bins of the pair emission angle with respect to the event plane (introduced in Chapter 6). In the case of an anisotropic source region the transverse radii are expected to oscillate. These oscillations reflect the eccentricity of the source at freeze-out.

In this Chapter, the analysis technique is explained in detail and the analyzed data sample as well as the applied cuts are introduced. The systematic uncertainties are discussed and the results are presented. Finally, the measurement is compared to theoretical model calculation as well as to the results obtained by the STAR experiment at RHIC.

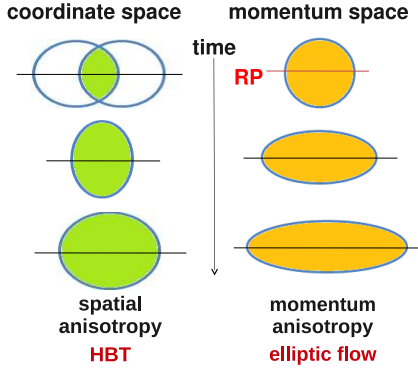


Figure 7.1.: The evolution of the source region in coordinate space (green, left) and momentum space (orange, right).

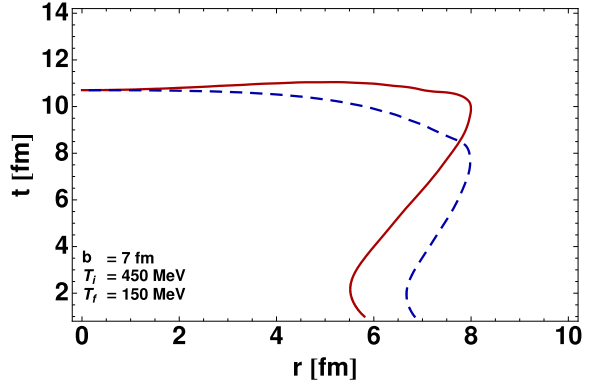


Figure 7.2.: Freeze-out radii in-plane (red solid curve) and out-of-plane (blue dashed curve) in dependence on the freeze-out time (Hydro calculation from KRAKOW model) [62].

7.1. Analysis Technique

Since the HBT analysis needs to be performed over many events and the directions of the impact parameters of the collisions are distributed randomly, all hints on the collision geometry average out in the analysis. The event plane, estimating the direction of the impact parameter based on the final-state particle distribution, can act as a reference in the transverse direction. If the HBT analysis is performed in bins of the pair emission angle with respect to the extracted event plane an azimuthally sensitive measurement of the radii can be obtained.

Hence, the first step of this analysis is to determine the event plane, using the framework presented in Chapter 6. The events are then analyzed like in an azimuthally-integrated HBT analysis but in 6 bins of the pair emission angle with respect to the event plane, φ ($-15^\circ - 15^\circ$, $15^\circ - 45^\circ$, $45^\circ - 75^\circ$, $75^\circ - 105^\circ$, $105^\circ - 135^\circ$, $135^\circ - 165^\circ$). Furthermore, the correlation functions are constructed in 7 centrality bins (0-5%, 5-10%, 10-20%, 20-30%, 30-40%, 40-50%, 50-70%), and in 4 k_T bins (0.2-0.3 GeV/c, 0.3-0.4 GeV/c, 0.4-0.5 GeV/c, 0.5-0.7 GeV/c) to allow a detailed study of the emission angle dependence of the radii.

Pion tracks within one bin in φ , k_T and centrality are then used to build pairs. The signal pairs are formed of tracks from the same event. For the background pairs one track is paired with each possible track in other buffered events. Like that, the background pairs are uncorrelated and can provide a normalization, i.e. the denominator of the correlation function (*event mixing*). The buffer storing the events used for event mixing is filled in 4 bins of z vertex position, 5 bins within one centrality bin and 6 bins in event plane orientation. The mixing is performed within 3 events. The emission angle of each pair has to be recalculated with respect to the

event plane orientation in the event from which the particles are coming from. Real pairs are filled in the numerator histogram, mixed pairs build up the denominator histogram. These histograms are filled in bins of centrality, pair momentum and pair emission angle.

The correlation function is obtained by dividing numerator and denominator and the radii parameter are extracted by fitting the correlation function for each bin with the following functional form (Equation (4.30)) [45]:

$$C(\mathbf{q}) = N[\lambda G(\mathbf{q})K(\mathbf{q}) + (1 - \lambda)]. \quad (7.1)$$

The Gaussian fit function has the following form (Equation (4.32)):

$$G(\mathbf{q}) = 1 + \exp(-R_{out}^2 q_{out}^2 - R_{side}^2 q_{side}^2 - R_{long}^2 q_{long}^2) \quad (7.2)$$

$$- 2R_{os}^2 q_{out} q_{side} - 2R_{ol}^2 q_{out} q_{long} - 2R_{sl}^2 q_{side} q_{long}). \quad (7.3)$$

In case of an anisotropic source, the transverse radii oscillate in dependence on the pair emission angle, illustrated in Figure 7.3. The strength of the oscillations reflect the anisotropy of the source at freeze-out. The longitudinal radius is not expected to depend on the pair emission angle. The cross-term in the transverse plane, R_{os}^2 , describes the tilt of the source in the (q_{out}, q_{side}) plane. If the source is now analyzed in different directions in this plane, the cross-term exhibits a sine oscillation as a function of the pair emission angle. The mean of each cross-term should be zero, they are very sensitive to potential problems, e.g. with the event mixing or pair reconstruction efficiency.

To investigate the radii oscillations in more detail, their φ dependence is fitted. $R_{out}^2(\varphi)$, $R_{side}^2(\varphi)$ and $R_{long}^2(\varphi)$ are described by:

$$R_i^2(\varphi) = R_{i,0}^2 + R_{i,2}^2 \cos(2\varphi), \quad (7.4)$$

where i stands for *out*, *side*, *long*. The cross-term $R_{os}^2(\varphi)$ is fitted with:

$$R_{os}^2(\varphi) = R_{os,0}^2 + R_{os,2}^2 \sin(2\varphi). \quad (7.5)$$

The average values, $R_{i,0}^2$, are directly comparable to the azimuthally-integrated analysis. The oscillation amplitudes, $R_{i,2}^2$, quantify the observed anisotropy, where the index 2 indicates that it is of second order. $R_{o,2}^2$, $R_{s,2}^2$, and $R_{os,2}^2$ are usually quoted normalized to $R_{s,0}^2$, where $R_{l,2}$ is normalized to $R_{l,0}^2$.

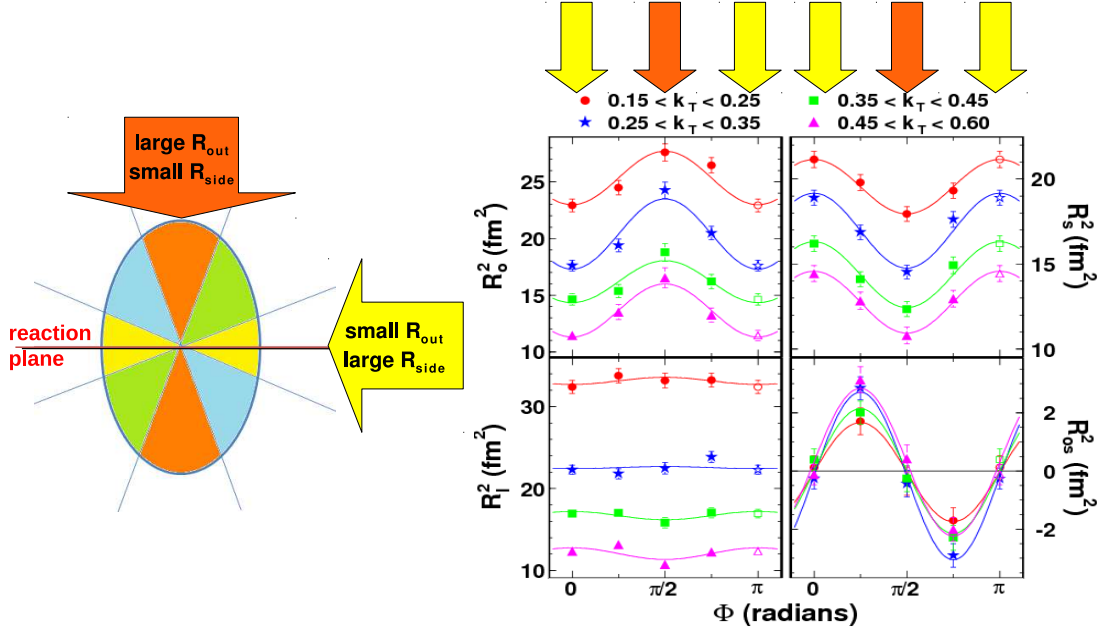


Figure 7.3.: Illustration of the oscillation of the transverse radii in case of an anisotropic source region (Measurement from [64]).

7.1.1. Event, Track and Pair Selection

The analyzed collision data was recorded in fall 2010 during the first Pb–Pb run at the LHC. About 6.5 million events at $\sqrt{s_{NN}} = 2.76$ TeV were selected and analyzed.

At first, collision candidates that have an interaction (bunch crossing) trigger and pass the background rejection criteria (e.g. they are not tagged as beam-gas events) are selected in order to ensure that only physics events are analyzed. Furthermore, a successfully reconstructed event plane is required. This implies that all event cuts that are applied in the event plane reconstruction (see Table 6.1) are also active here. The event vertex position in z is further constrained to ± 8 cm.

For the analysis, TPC-only tracks are used. The tracks are selected according to the standard track cuts listed in Table 7.1. The track information was recalculated after restraining the tracks to the primary vertex reconstructed with the SPD. Additionally, the η range is restricted to $|\eta| < 0.8$. This is the range where the TPC has full coverage. Only particles with $0.15 \text{ GeV}/c < p_T < 2 \text{ GeV}/c$ are considered, since particles with smaller p_T do not reach or curl inside the TPC and because the high- p_T particles are less correlated with the low- p_T bulk particles.

The pion tracks are identified via their specific ionization energy loss (dE/dx) inside the TPC with a σ cut around the pion line. For low-momentum pions

Variable	Cut Value
Number of reconstructed TPC clusters	> 70
χ^2 per TPC cluster	< 4
Distance of closest approach to primary vertex in z	< 3.2 cm
Distance of closest approach to primary vertex in x and y	< 2.4 cm
Kink rejection	applied

Table 7.1.: Default track cuts applied in the analysis.

($p < 0.35$ GeV/ c) the cut is at 5σ , if 0.35 GeV/ $c < p < 0.5$ GeV/ c a 3σ cut is applied, for higher momenta the value is 2σ . Furthermore, a pair cut is applied to reject pairs of very close tracks (introduced in detail in Chapter 5). The values that are defined there are used for the analysis: $\Delta\eta < 0.017$ and $\Delta\varphi_{min} < 0.012$.

To assure a good-quality event plane reconstruction, the distributions shown in Figure 7.4 are monitored. The upper left panel shows the distribution of the event plane angle which is flat, indicating a good performance. The upper right panel illustrates the effects of the slightly non-uniform TPC acceptance in azimuth (discussed in Chapter 6 and corrected for the event plane determination) on the pair φ distribution. Variations from the average are visible but only of the order of 1%. They are not expected to have a large influence on the azimuthally sensitive HBT interferometry results since the radii are not dependent on the number of pairs in one direction but only on their homogeneity length. The lower left plot compares the pair emission angle with respect to the event plane angle for real and mixed pairs. The modulation in both distributions of almost 30% is coming from the single-particle correlation with the event plane. In addition, the ratio is shown on the lower right. There is a small modulation of 0.1% visible in the difference between real and mixed pairs, which might be due to two-particle correlations with the event plane or residual imperfections of the mixing procedure.

The effect of the two-track cut can be seen in the two-dimensional plane of q_{out} and q_{side} . In Figure 7.5 the three-dimensional correlation function is projected over a small range (0.02 GeV/ c) around $q_{long} = 0$ GeV/ c . It can be clearly seen that the cut removes pairs on one diagonal or the other, depending on charge and magnetic field orientation. In the correlation function, the structures coming from two-track effects are removed. For high pair momenta or low centralities the underpopulated region along the cut diagonal can lead to difficulties during a bin-wise fitting procedure due to empty bins. An advantage of the applied pair cut is that it is very narrow at low q_{out} and q_{side} , saving as much good tracks as possible in this region that is important for the correlation function.

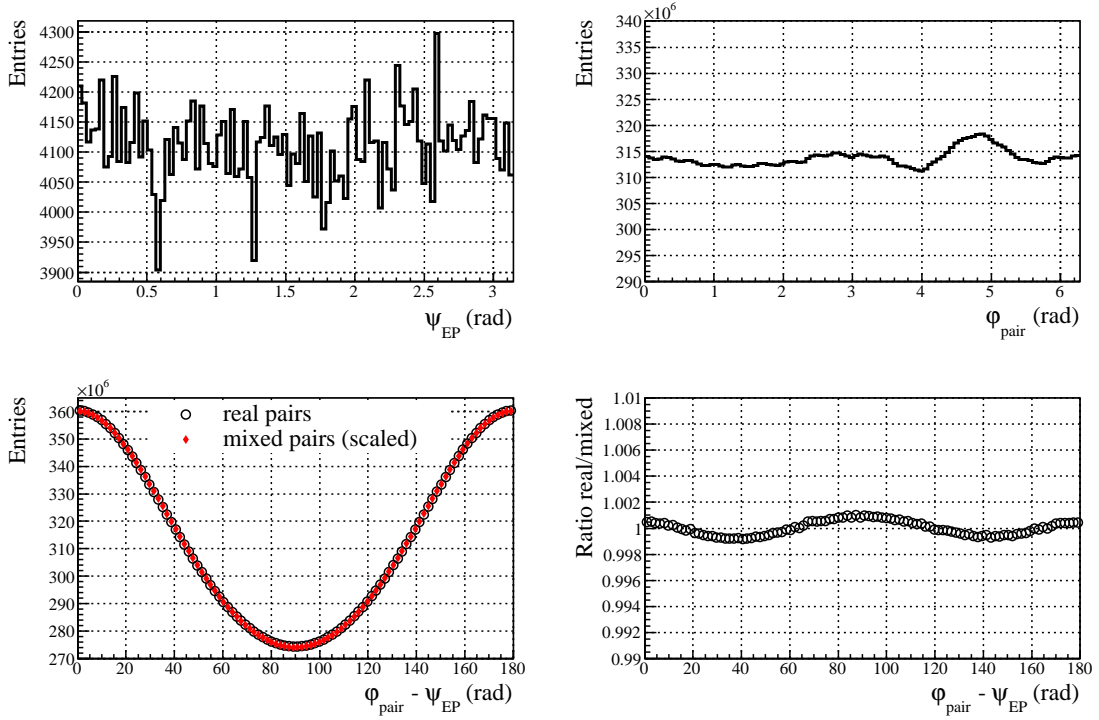


Figure 7.4.: Event plane angle distribution (upper left), pair φ distribution (upper right), distribution of the pair φ with respect to the event plane angle for real and mixed pairs (lower left) and their ratio (lower right).

7.1.2. Corrections

To remove effects that occur in addition to the Bose–Einstein enhancement from the measured correlation function, several corrections have to be applied - some of them directly on the level of the correlation function, some during the fitting procedure.

Correction for Event Plane Resolution

The finite resolution of the event plane (see also Sections 6.1.1 and 6.5) leads to a reduction of the oscillations of the transverse radii that are expected in case of an asymmetric source. This can be thought of as a bin migration effect between the analyzed bins in pair emission angle with respect to the event plane. The simple approach that is also applied in flow analyses is to assume that the finite resolution weakens the correlations with the event plane proportional to the achieved resolution parameter. To correct for this, the measured oscillation amplitude is divided by the event plane resolution.

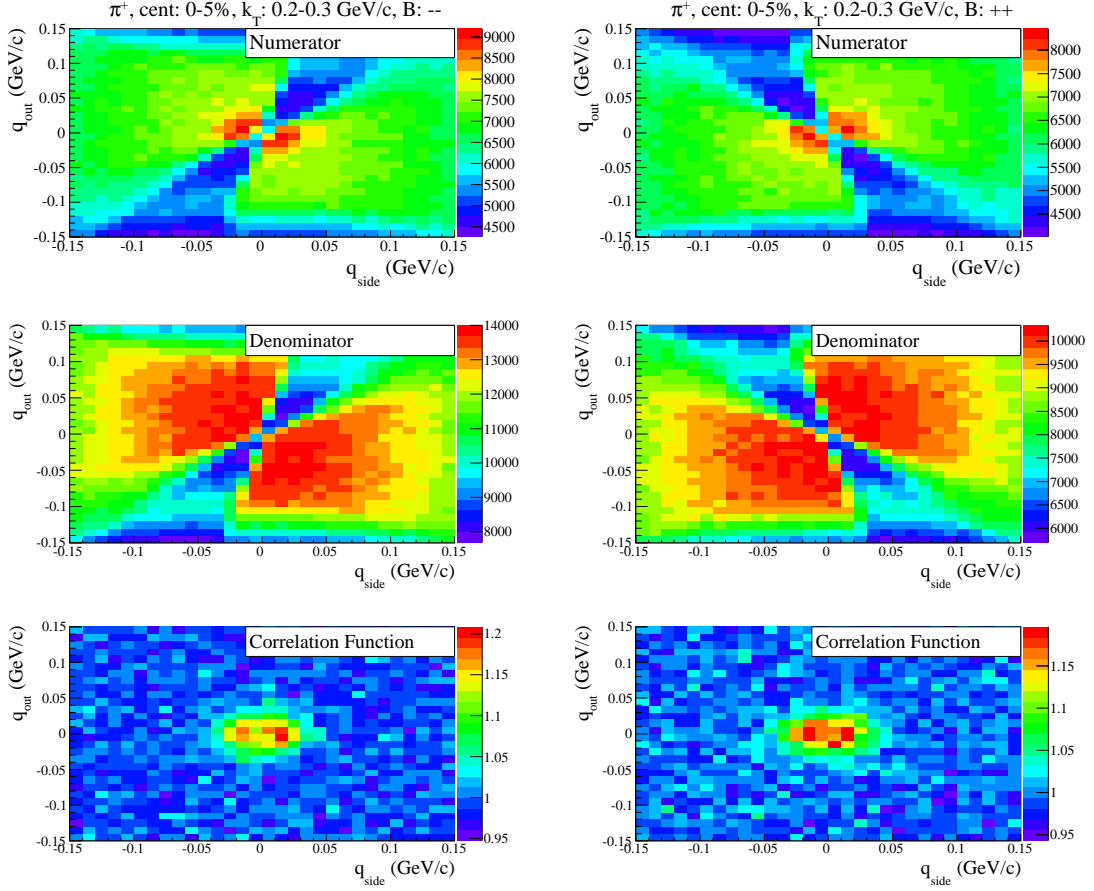


Figure 7.5.: Two-dimensional projections of the numerator, the denominator, and the correlation function in the (q_o, q_s) plane, illustrating the effect of the applied pair cut for different magnetic field orientations.

Another approach, following Reference [60], corrects for resolution effects already on the level of the numerator and denominator and accounts for the reduction of the measured correlation of the radii with the event plane due to a finite number of bins in φ . The correction formula for the numerator in dependence on the relative pair momentum q and the considered pair emission angle bin ϕ_j is given by

$$N(q, \phi_j) = N_{exp}(q, \phi_j) + 2 \left(\sum_{n=1}^{n_{bins}} \xi_{n,m}(\Delta) [N_{c,n}^{exp}(q) \cos(n\phi_j) + N_{s,n}^{exp}(q) \sin(n\phi_j)] \right), \quad (7.6)$$

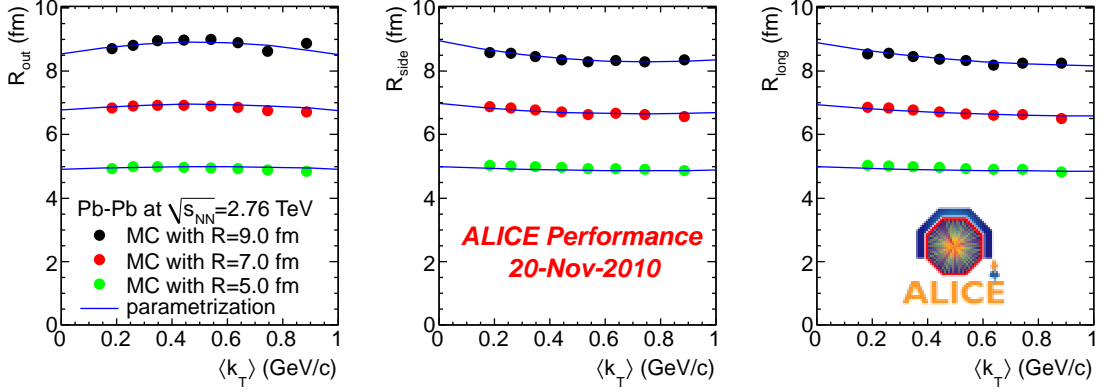


Figure 7.6.: HBT radii extracted from reconstructed Monte Carlo tracks in dependence on the transverse pair momentum [61].

with the experimentally determined distribution, N_{exp} , and its decompositions

$$N_{c,n}^{exp}(q) = \langle N_{exp}(q, \phi) \cos(n\phi) \rangle = \frac{1}{n_{bins}} \sum_{j=1}^{n_{bins}} N_{exp}(q, \phi_j) \cos(n\phi_j),$$

$$N_{s,n}^{exp}(q) = \langle N_{exp}(q, \phi) \sin(n\phi) \rangle = \frac{1}{n_{bins}} \sum_{j=1}^{n_{bins}} N_{exp}(q, \phi_j) \sin(n\phi_j). \quad (7.7)$$

The correction factor ξ is given by

$$\xi_{n,m}(\Delta) = \frac{n\Delta/2}{\sin(n\Delta/2)\mathcal{R}_{EP}}, \quad (7.8)$$

where Δ is the bin width and \mathcal{R}_{EP} is the measured event plane resolution.

Correction for Finite Momentum Resolution

The finite momentum resolution of the detector leads to a broadening of the correlation peak and therefore reduces the extracted HBT radii. The resolution is determined by the finite position resolution inside the detector and multiple scattering. In a Monte Carlo study, an artificial correlation can be introduced by applying a Gaussian weight to the pairs according to their momentum difference. The known input radius is then compared to the result extracted from reconstructed Monte Carlo tracks (Figure 7.6). The difference is found to be of up to 4%. The corresponding correction factors are determined in each bin of k_T and applied to the experimental HBT radii.

Correction for Coulomb Interaction

The Coulomb interaction between the two pions of the pair has an influence on the extracted radii and has to be accounted for in the fit (see Section 4.3). The squared Coulomb wave function averaged over a spherical source with a size comparable to the mean of the three extracted radii parameter was calculated and included in the fit. The used Coulomb source sizes are listed in Table 7.2.

Event Centrality	Coulomb Source
0-5%	11 fm
5-10%	10 fm
10-20%	9 fm
20-30%	8 fm
30-40%	7 fm
40-50%	6 fm
50-70%	4 fm

Table 7.2.: Coulomb source sizes used to calculate the Coulomb interaction between the pair particles.

7.1.3. Systematic Effects

The systematic effects influencing the extracted radii parameters are independent of the pair emission angle, the study of these effects can be performed in an azimuthally integrated analysis. The effects discussed below are added quadratically to estimate the systematic uncertainties of the radii. This results in a systematic uncertainty of up to 7% for R_{out} and of up to 6% for R_{side} and R_{long} . The detailed evaluation of the systematic uncertainties of the HBT radii are summarized in Table 7.3 at the end of this Chapter.

Pair Cut

The pair selection cut that is applied in order to avoid effects of reconstruction difficulties on the extracted radii can be defined in several ways (see Chapter 5). Here, two different variations of a cut on the angular distance of the tracks of a pair are compared to estimate the systematic uncertainty connected to the application of this cut. The effect is expected to be most prominent for very central events, where the multiplicities are the highest. Figure 7.7 shows the ratio of the resulting radii for both pair cuts for 0-5% centrality. These results are taken as an upper limit for the systematic effect in less central events. The effect is k_T dependent, the

7. Azimuthally Sensitive HBT Interferometry

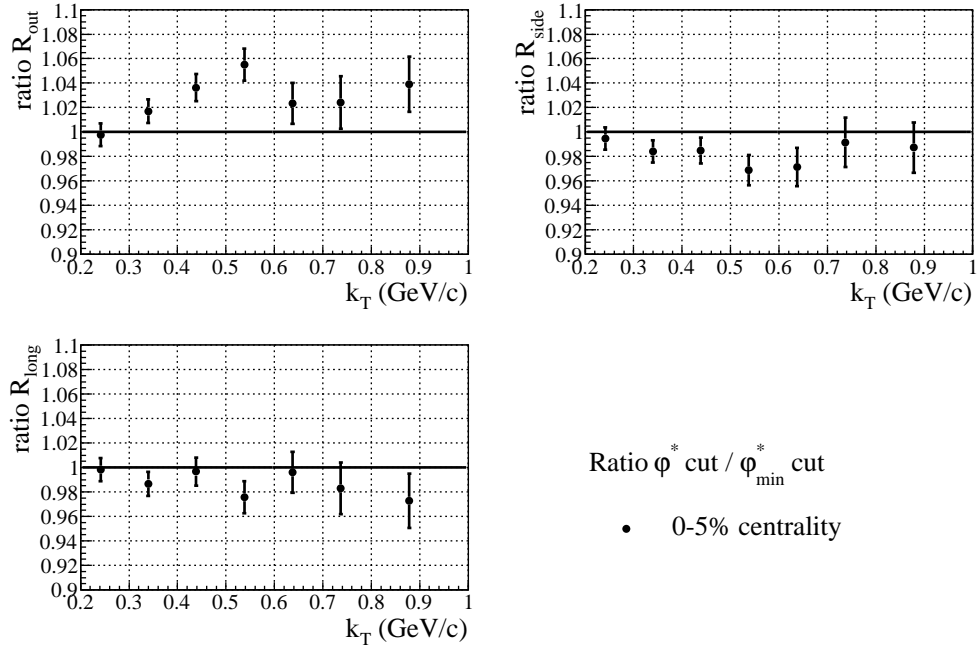


Figure 7.7.: Comparison of two different pair cuts. Shown is the ratio of the results obtained with two different pair cuts.

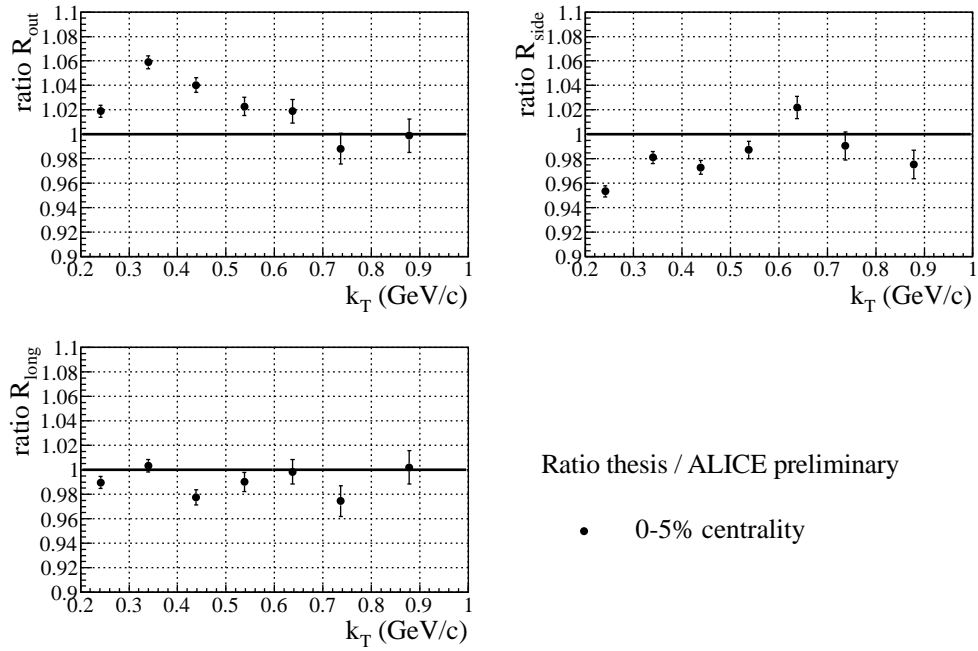


Figure 7.8.: Comparison with results that are obtained with a different analysis code.

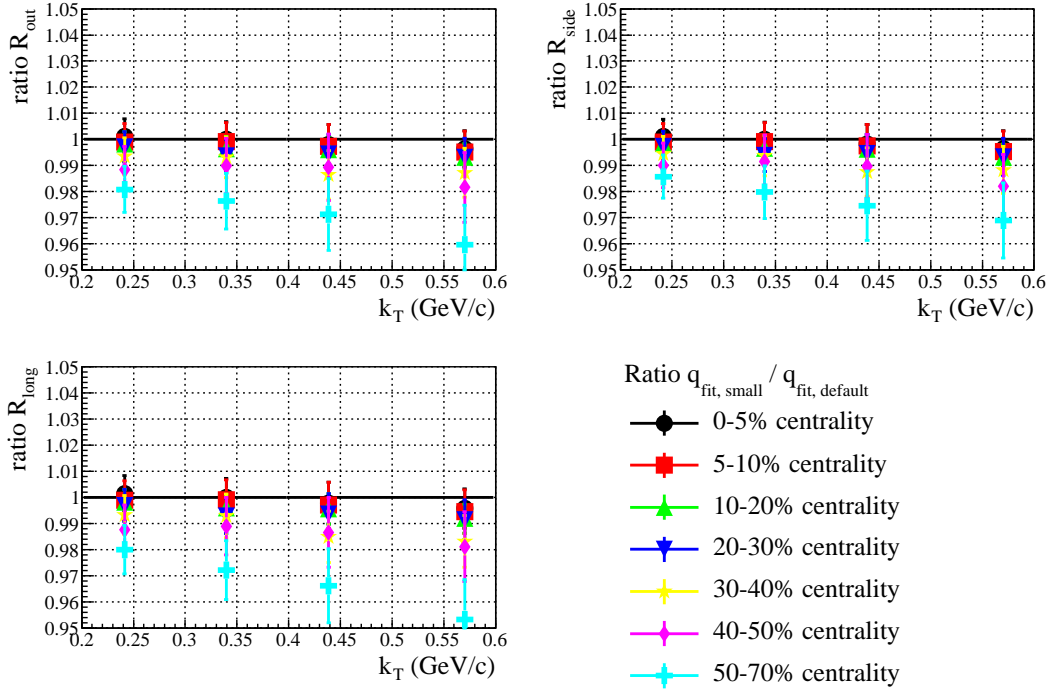


Figure 7.9.: Influence of the considered fit range on the extracted radii.

difference increases with increasing pair momentum. For high k_T bins, the results become similar again. The variation is of up to 5% for R_{out} and up to 3% for R_{side} and R_{long} .

Fitting Procedure, Event and Track Selection

The results are compared to the radii extracted with a different analysis code with slightly different event and track selection criteria, as well as a different fitting procedure (χ^2 minimization) and a different fitting code. Again, the most central events serve as an upper limit for the observed variations. The differences vary with k_T and are of up to 6% for R_{out} , up to 5% for R_{side} and 2% for R_{long} (Figure 7.8).

Fit Range

The extracted radii might depend on the fit range. In order to estimate the variation, the fit range was reduced by 0.04 GeV/c in q_i . The results are plotted in Figure 7.9. The variation is below 1% for 0-30% centrality. For 30-50% central events the variation is found to be smaller than 1% and of up to 1.5% for the highest k_T bin. The most peripheral events with 50-70% centrality are not used to extract

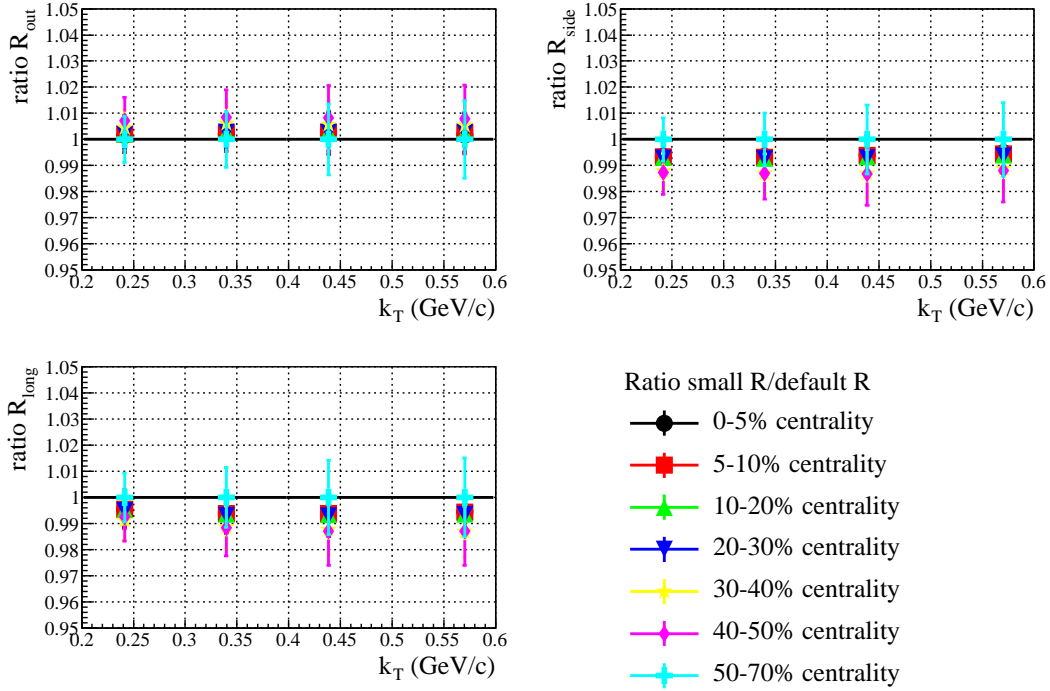


Figure 7.10.: Ratio of results that are obtained with different Coulomb source sizes.

an uncertainty since the reduction of the fit range here means that the correlation peak is already wider than the considered fit range, and a systematic effect would be overestimated.

Coulomb Source Size

For the performance of the Coulomb correction explained above the correlation radius for the interaction has to be given as an input value. This value is a priori not known and can only be extracted from the HBT radii in an iterative process. To give an idea of the methodological uncertainties connected with this correction the HBT radii were extracted with the Coulomb source sizes being reduced by 2 fm. The results can be seen in Figure 7.10. The variations are almost centrality-independent and are smaller than 1.5%.

Magnetic Field Orientation

The results for different magnetic field orientations were compared and the variations are smaller than 3% for the transverse radii and smaller than 5% for R_{out} .

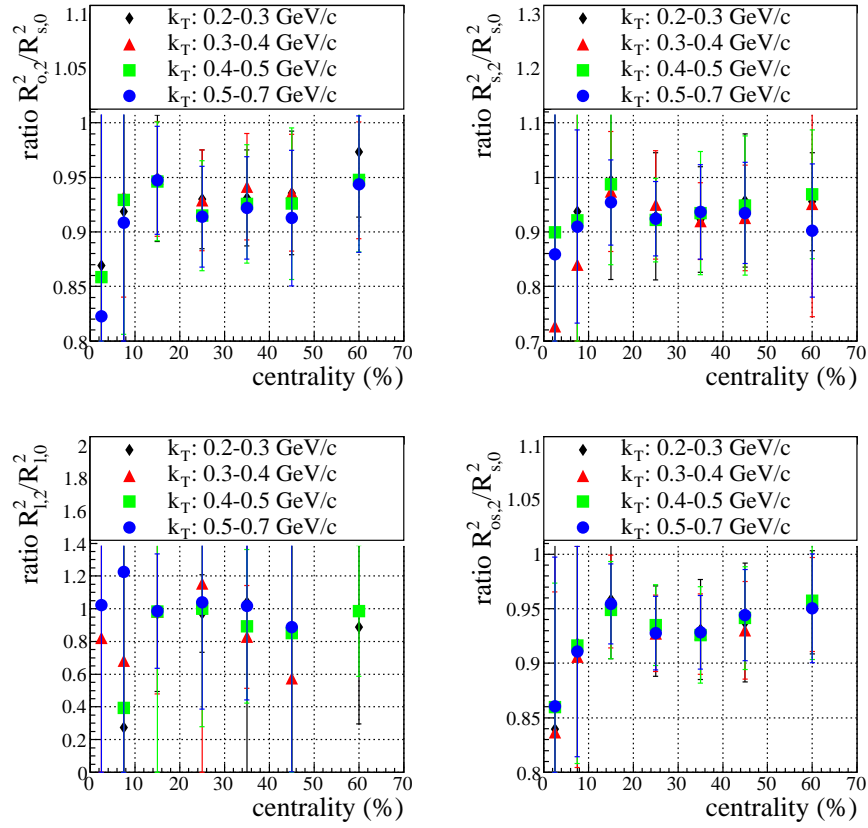


Figure 7.11.: Ratio of fit parameters for both correction procedures for the event plane resolution. Shown is the ratio of the results obtained with the correction procedure that is explained first in Section 7.1.2 over the results obtained with the second method.

Event Plane Resolution Correction

In order to estimate the uncertainty that is connected to the correction of the event plane resolution, the results for the oscillation amplitudes obtained by applying the different correction procedures described in Section 7.1.2 are compared (Figure 7.11). For the very central bins the amplitudes are very small and the ratio can only be quoted with large error bars, and is therefore not included in the estimation of the uncertainty. The difference for the mid-central and peripheral bins is of up to 7% is added as an uncertainty on the oscillation amplitudes.

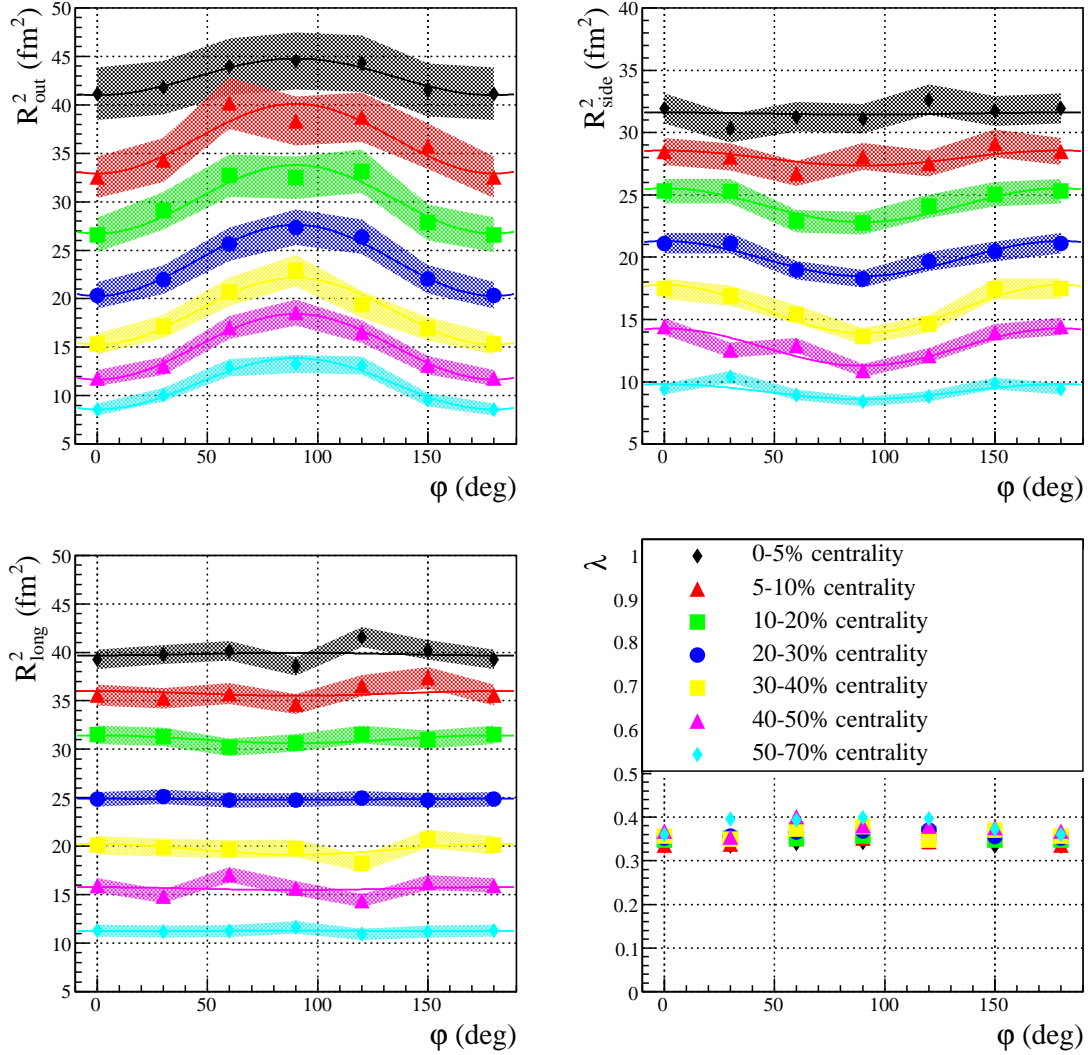


Figure 7.12.: Azimuthal dependence of the extracted radii parameters for $k_T = 0.3 - 0.4 \text{ GeV}/c$, and different centrality bins. The shaded error bands indicate the systematic uncertainties on the radii, the statistical errors are plotted as error bars, but are too small to be visible for most points.

7.2. Results

The HBT radii can now be extracted in dependence on the pair emission angle with respect to the reconstructed event plane. The results for an example bin, $k_T = 0.3 - 0.4 \text{ GeV}/c$ and different centralities are shown in Figures 7.12 and 7.13.

The upper panels of Figure 7.12 show the azimuthal dependence of the transverse radii, R_{out}^2 and R_{side}^2 . They exhibit clear oscillations with opposite amplitudes. R_{long}^2 shows no significant ϕ dependence as expected (lower left panel of Figure 7.12). The

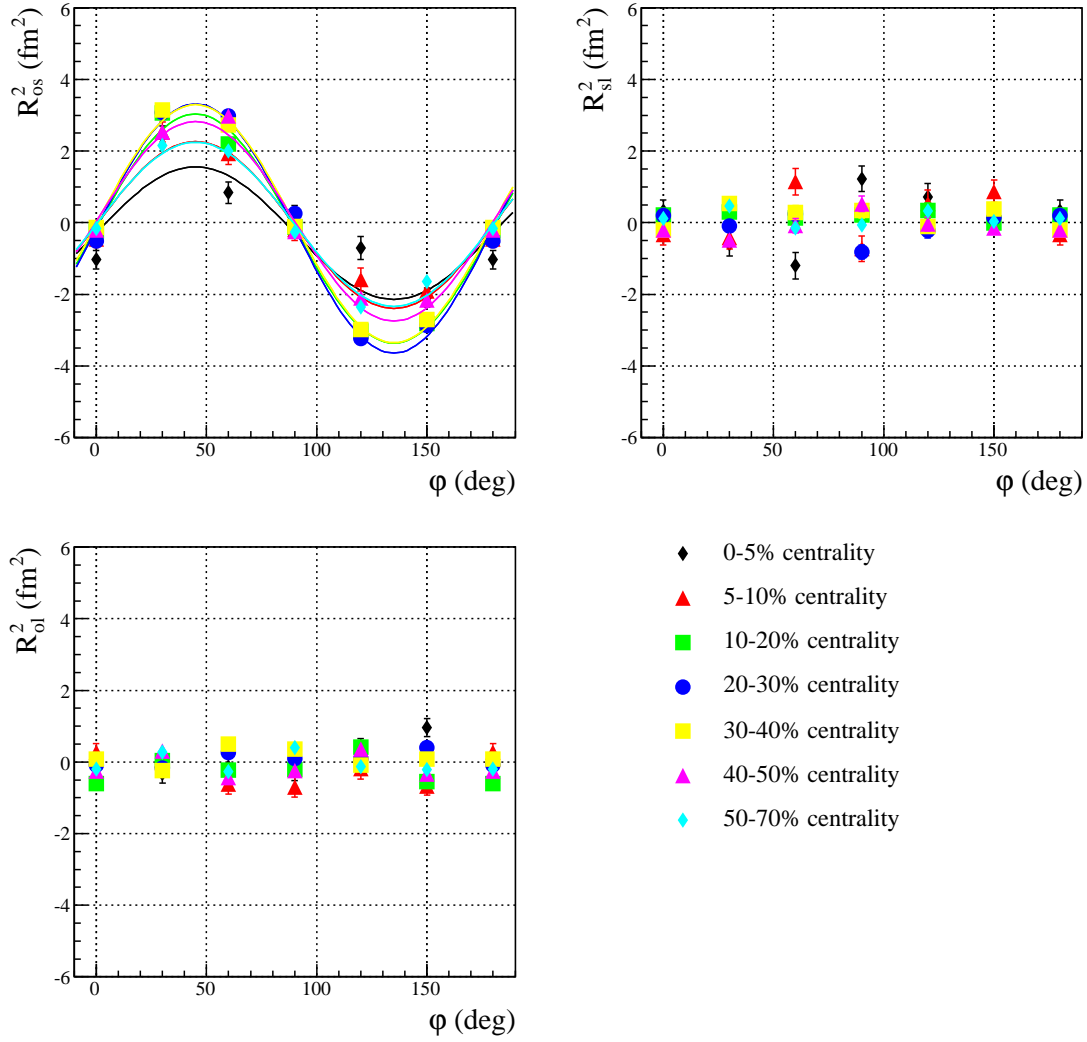


Figure 7.13.: Azimuthal dependence of the cross-term parameters for $k_T = 0.3 - 0.4 \text{ GeV}/c$ and different centrality bins.

oscillations increase when going from central to peripheral events. In Figure 7.13 can be seen that the cross-terms R_{ol} and R_{sl} vanish as expected, whereas R_{os} (upper left panel) shows a sine oscillation, consistent with the dependencies of the transverse radii.

The fit parameter λ is also plotted here to ensure that the observed oscillations of the radii do not occur because of fitting difficulties and fluctuations in this parameter (see Figure 7.12, lower right panel).

In Figures 7.14 and 7.15 the results are shown for one centrality bin (20-30% centrality) and different pair momenta. The oscillations in the transverse radii are clearly

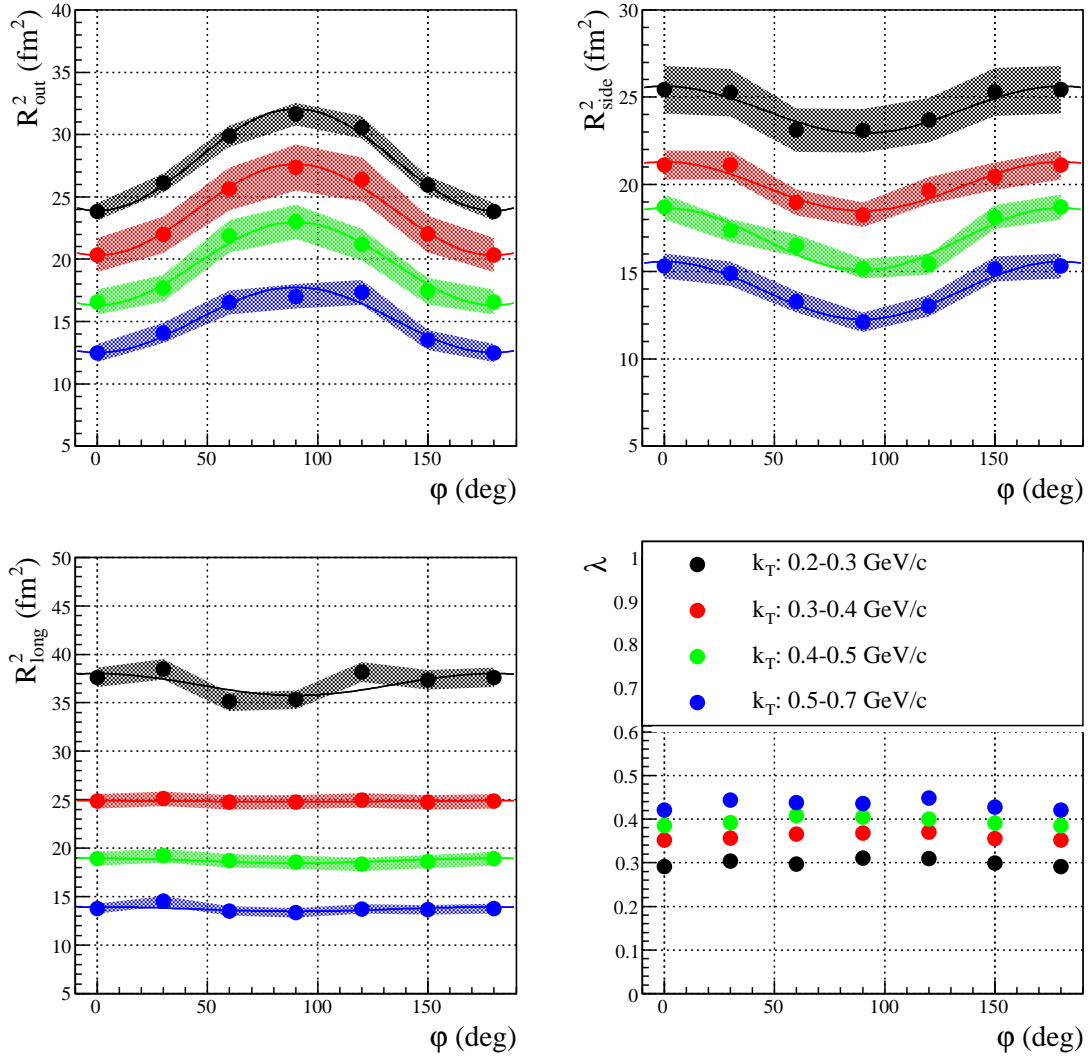


Figure 7.14.: Azimuthal dependence of the extracted radii parameters for 20-30% centrality and different pair transverse momenta. The shaded error bands indicate the systematic uncertainties on the radii, the statistical errors are plotted as error bars, but are too small to be visible for most points.

visible for all k_T bins and the cross-term oscillation is almost independent of k_T as well.

These trends are discussed quantitatively in the following. The observed oscillations are fitted with Equations (7.4) and (7.5) to quantify the azimuthal oscillations of the radii. The obtained fit parameters are shown in Figures 7.16 and 7.17. The average radii $R_{i,0}$ can be seen in Figure 7.16, the oscillation amplitudes are plotted in Figure 7.17. The systematic effects explained above are expected to be uncorrelated

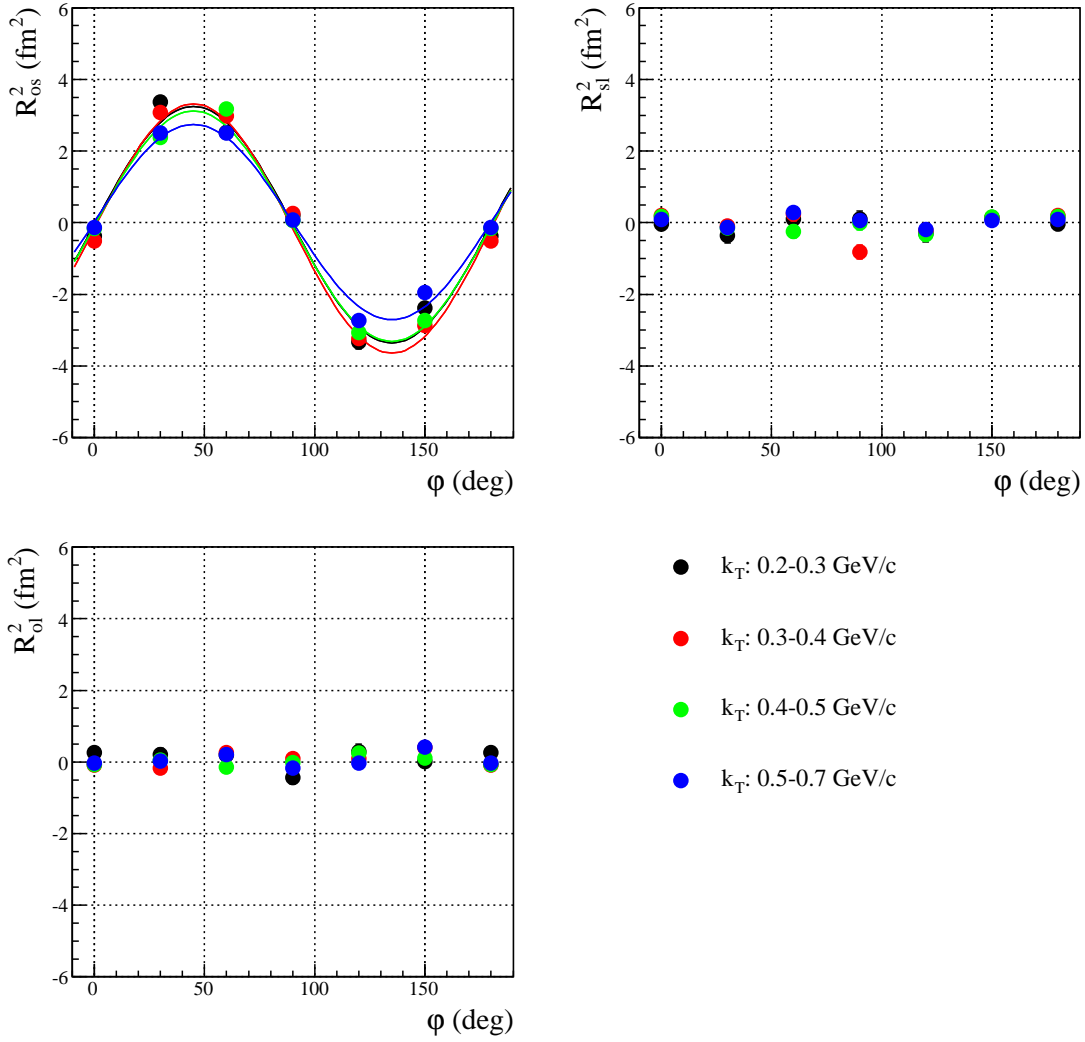


Figure 7.15.: Azimuthal dependence of the cross-term parameters for 20-30% centrality and different pair transverse momenta.

with the emission angle, the uncertainty is considered in the fitting procedure. In addition, the emission-angle dependent uncertainty of the oscillation amplitudes due to the correction methods for the event plane resolution is included.

The average values decrease from central to peripheral events, in agreement with the results from the azimuthally-integrated analysis. The oscillation amplitudes for the transverse radii have opposite signs, $R_{o,2}$ is larger than $R_{s,2}$ (up to a factor of 2). Both amplitudes show a similar centrality dependence, the absolute value increases from central to peripheral events. Furthermore, the amplitudes level out towards peripheral events. The same behavior with centrality is also observed for the cross-

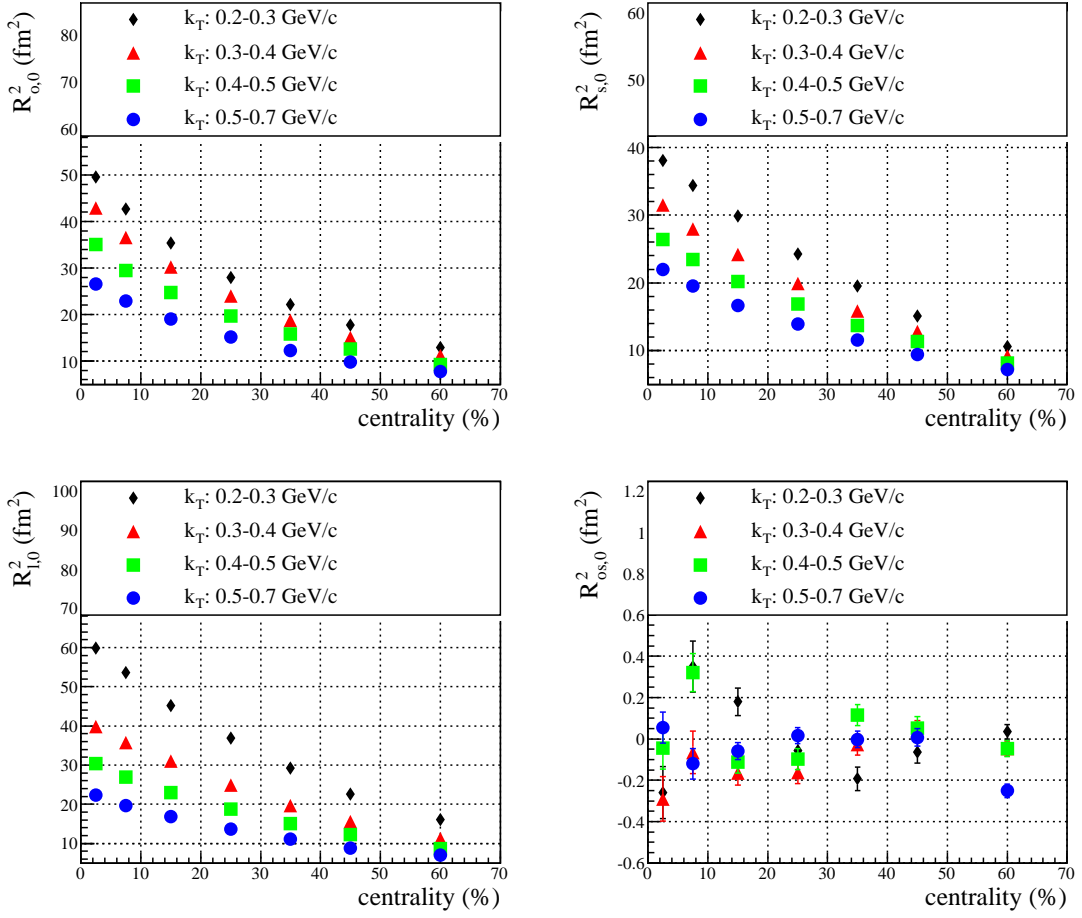


Figure 7.16.: Average value for the radii parameters extracted as the baseline of the fit to the observed oscillations, shown for different pair momenta in dependence on the event centralities.

term $R_{os,2}$. $R_{l,2}$ is consistent with zero, small deviations could be explained as an effect of radial flow.

The results do not change much with pair momentum but indicate that the oscillation amplitudes are higher for higher pair transverse momenta. Additionally, the amplitudes for low k_T level off for very peripheral events, whereas this is not clearly observable at high k_T .

7.3. Comparison to RHIC and Theoretical Models

The extracted fit parameters are confronted with a hydrodynamic calculation from the model AZHYDRO [48]. It is an ideal hydrodynamical calculation and does

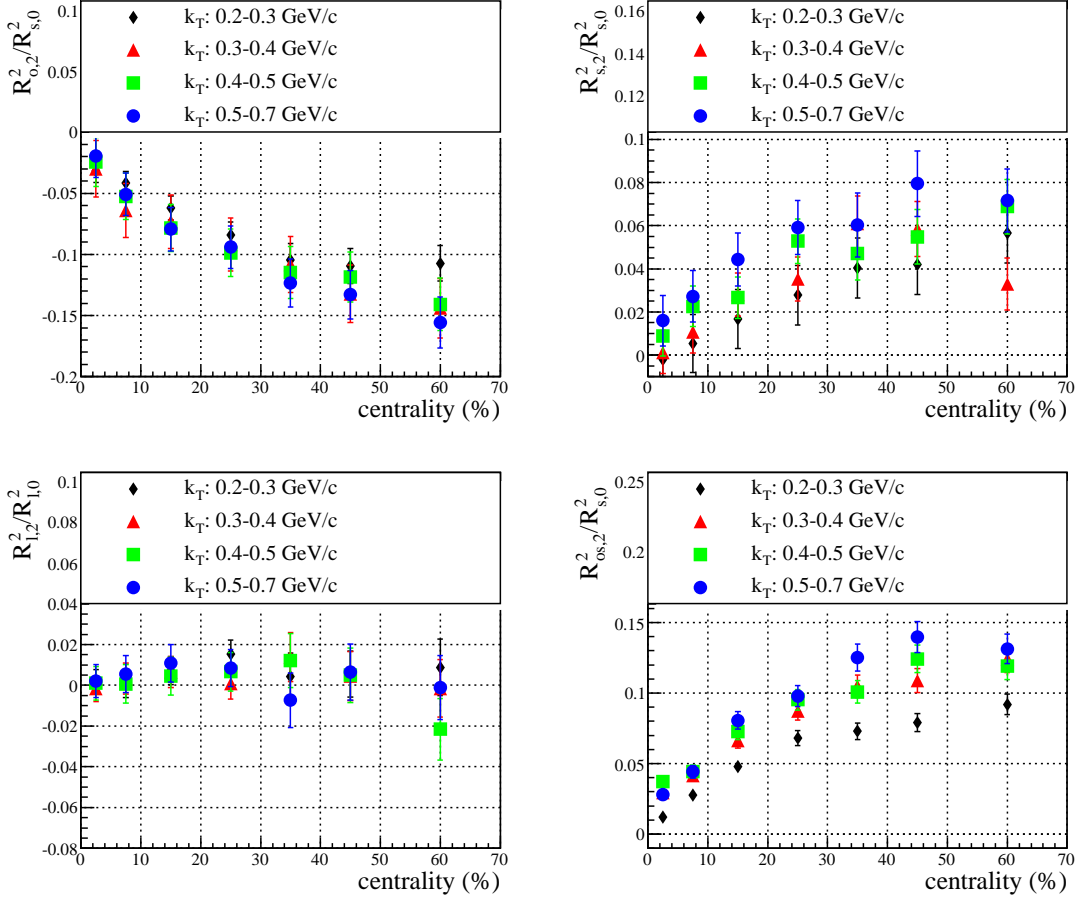


Figure 7.17.: Normalized oscillation amplitudes extracted from the fit to the observed azimuthal dependence of the radii, shown for different pair momenta in dependence on the event centralities.

not consider hadronic rescattering after the chemical freeze-out. It predicted the azimuthal dependence of the HBT radii at the originally planned energy for Pb–Pb collisions at LHC, $\sqrt{s_{NN}} = 5.5$ TeV, instead of $\sqrt{s_{NN}} = 2.76$ TeV. The comparison is shown in Figure 7.18. The calculation was performed for an impact parameter of 7 fm and is therefore compared to events with 20–30% centrality.

The model predicts that the oscillation amplitudes vary less with k_T for higher momenta. This trend is also indicated in the measured data. It also predicts a sign change of the amplitudes at very low k_T . The data can not confirm or exclude this, for this purpose, the analysis would have to be performed for even lower pair momenta. In both model and data the absolute value of the oscillation amplitude is highest for R_{out} and R_{os} , R_{side} , and it is the smallest for R_{long} . Nevertheless, the overall size of the oscillations is overestimated in AZHYDRO and does not agree with the measured values.

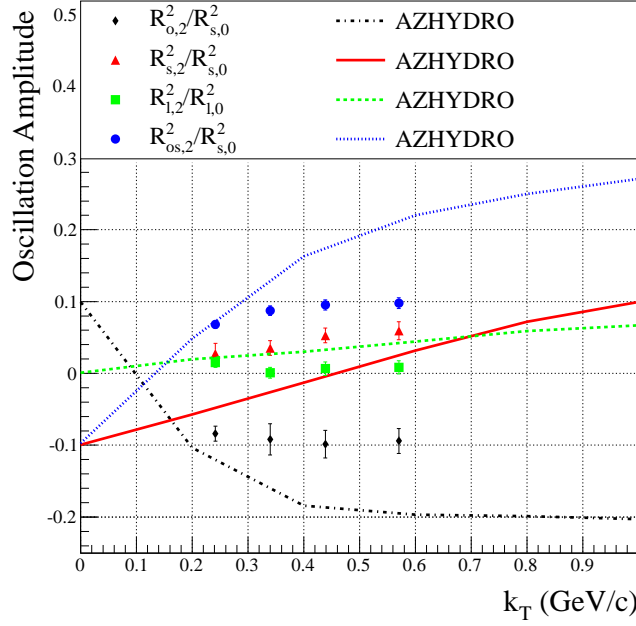


Figure 7.18.: Comparison of the extracted oscillation amplitudes in dependence on the pair transverse momentum with model predictions from AZHYDRO.

A comparison to the KRAKOW model [62] can be seen in Figures 7.19 and 7.20. The results are given as a function of the number of participants which can be connected to the event centrality by a Glauber Model calculation [22]. This model combines perfect-fluid hydrodynamics with statistical hadronization. Gaussian initial conditions are assumed, the hydrodynamic evolution starts early, and an Equation of State including a smooth cross-over transition is used [62]. The hadronization is modeled with Therminator [31], for the azimuthal features of the source the Glauber Monte Carlo GLISSANDO [63] is used. The predictions were made for Pb–Pb collisions at $\sqrt{s_{NN}} = 5.5$ TeV.

Apart from the difference in energy, the k_T binning is slightly different in the model calculation. The bins are given by: 0.15–0.25 GeV/ c , 0.25–0.35 GeV/ c , and 0.35–0.45 GeV/ c . This means that the results are not directly comparable, but the model values for a k_T bin correspond to a slightly lower value. $R_{o,0}$ is relatively well predicted, especially for higher k_T . $R_{s,0}$ and $R_{l,0}$ are overestimated for all k_T bins. The normalized oscillation amplitudes for $R_{s,2}$ and $R_{os,2}$ are predicted quite well. The model calculations agree with the measured results within the errors for many bins. The amplitudes for $R_{o,2}$ are underestimated, especially for lower numbers of participants the measured oscillations are found to be larger in data as is calculated from this model.

The STAR experiment at RHIC performed an azimuthally sensitive HBT analysis

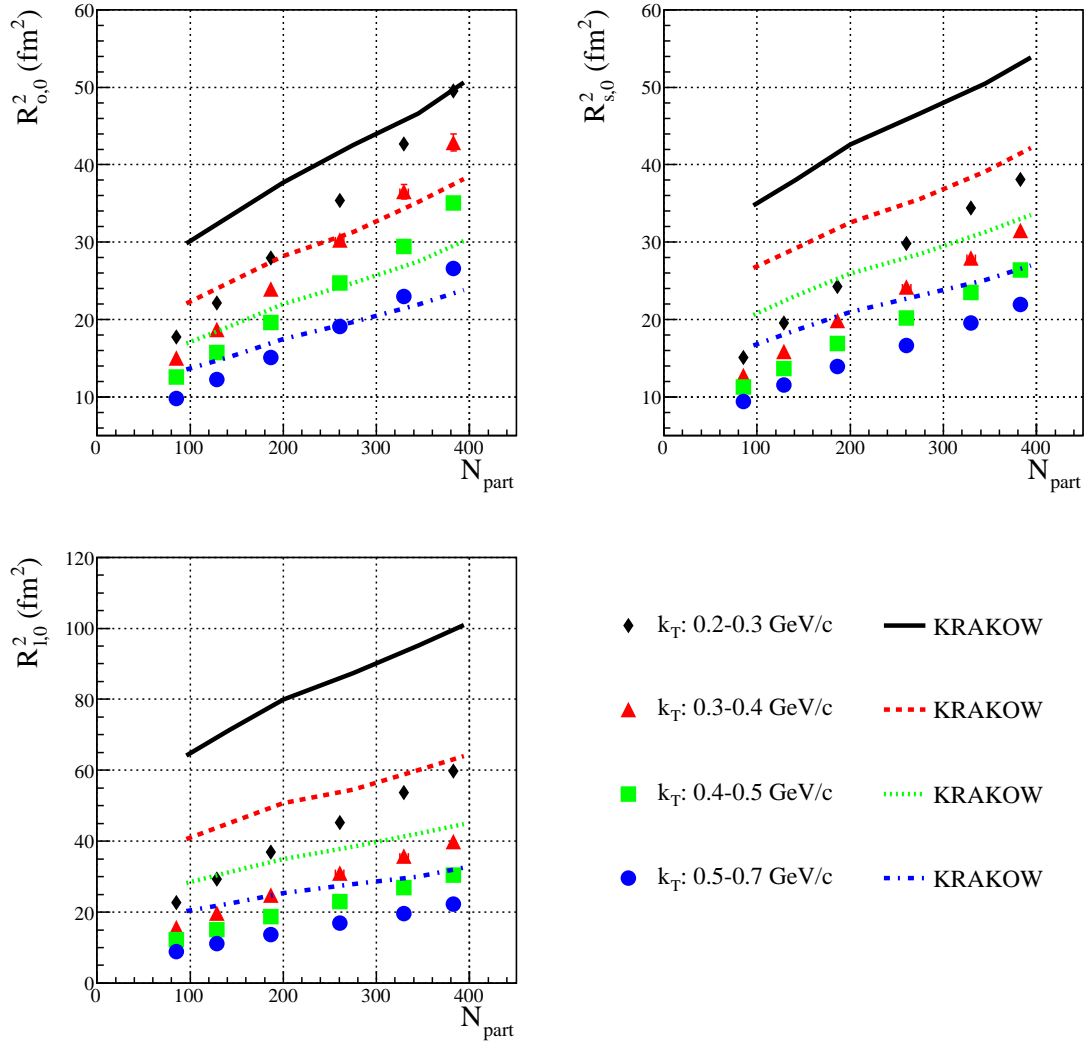


Figure 7.19.: Comparison with KRAKOW model results: average radii.

for Au–Au collisions at 200 GeV [64]. The results are compared to the presented analysis results in Figures 7.21 and 7.22. Apart from the different energies and collision systems, the k_T binning is slightly different in the STAR analysis. Their bins are: 0.15–0.25 GeV/ c , 0.25–0.35 GeV/ c , and 0.35–0.45 GeV/ c . As for the KRAKOW model results, this means that the results are only approximately comparable, but the STAR values for a k_T bin correspond to a slightly lower value.

As already observed in the azimuthally-integrated analysis, the HBT radii at LHC energies are up to 20% higher than at RHIC [47]. The oscillation amplitudes for the transverse radii are similar, no significant reduction of the absolute value is observed. The longitudinal amplitude is at both energies very small. The cross-

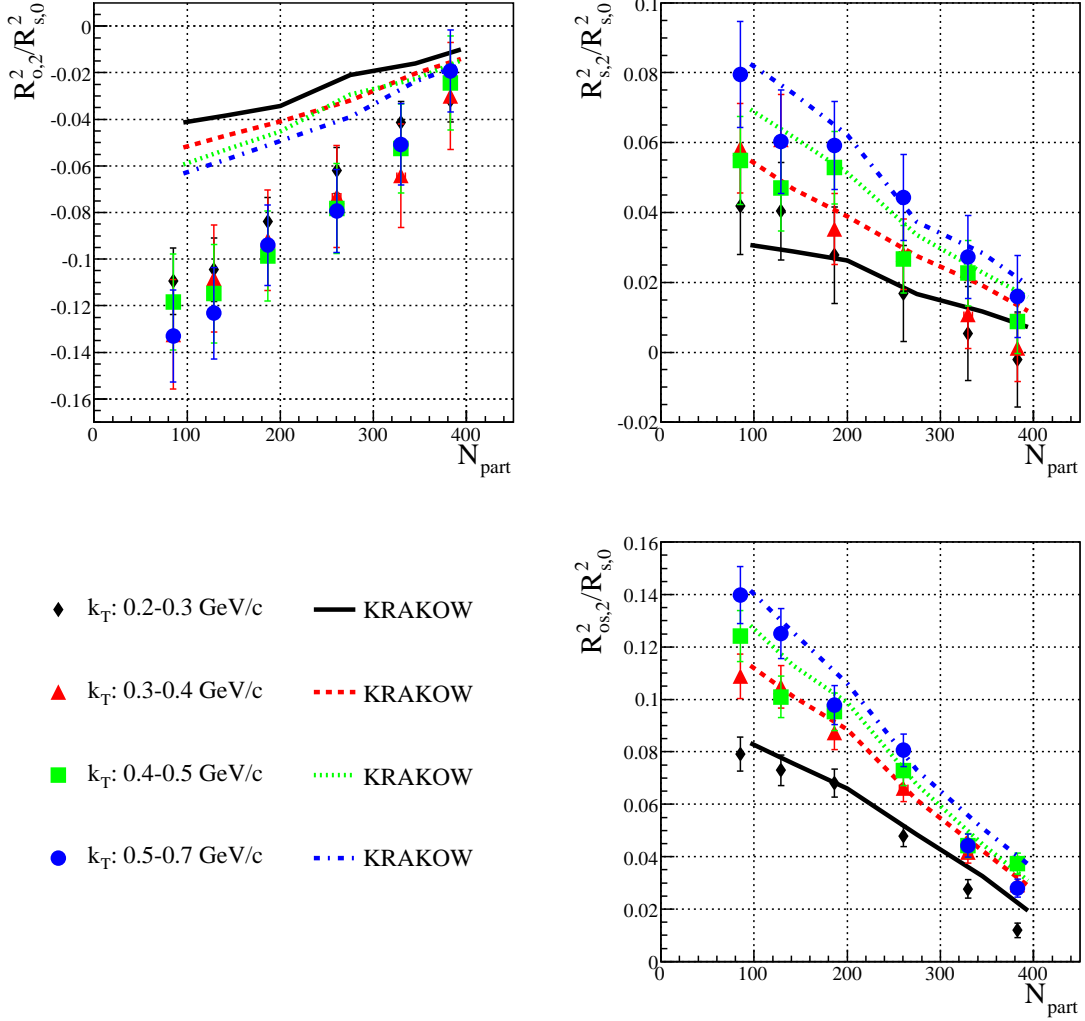


Figure 7.20.: Comparison with KRAKOW model results: radii oscillation amplitudes.

term oscillation seems to be slightly smaller for STAR, but this could as well be an effect of the different binning in pair transverse momentum.

In summary, the extracted oscillation amplitudes are similar to the results obtained at RHIC. The model calculation from AZHYDRO describes some qualitative features of the parameters but overestimates the size of the amplitudes, whereas the KRAKOW model describes the oscillation parameters very well. Only the amplitude of $R_{o,2}$ is underestimated. The predicted average radii also deviate clearly from the measured results.

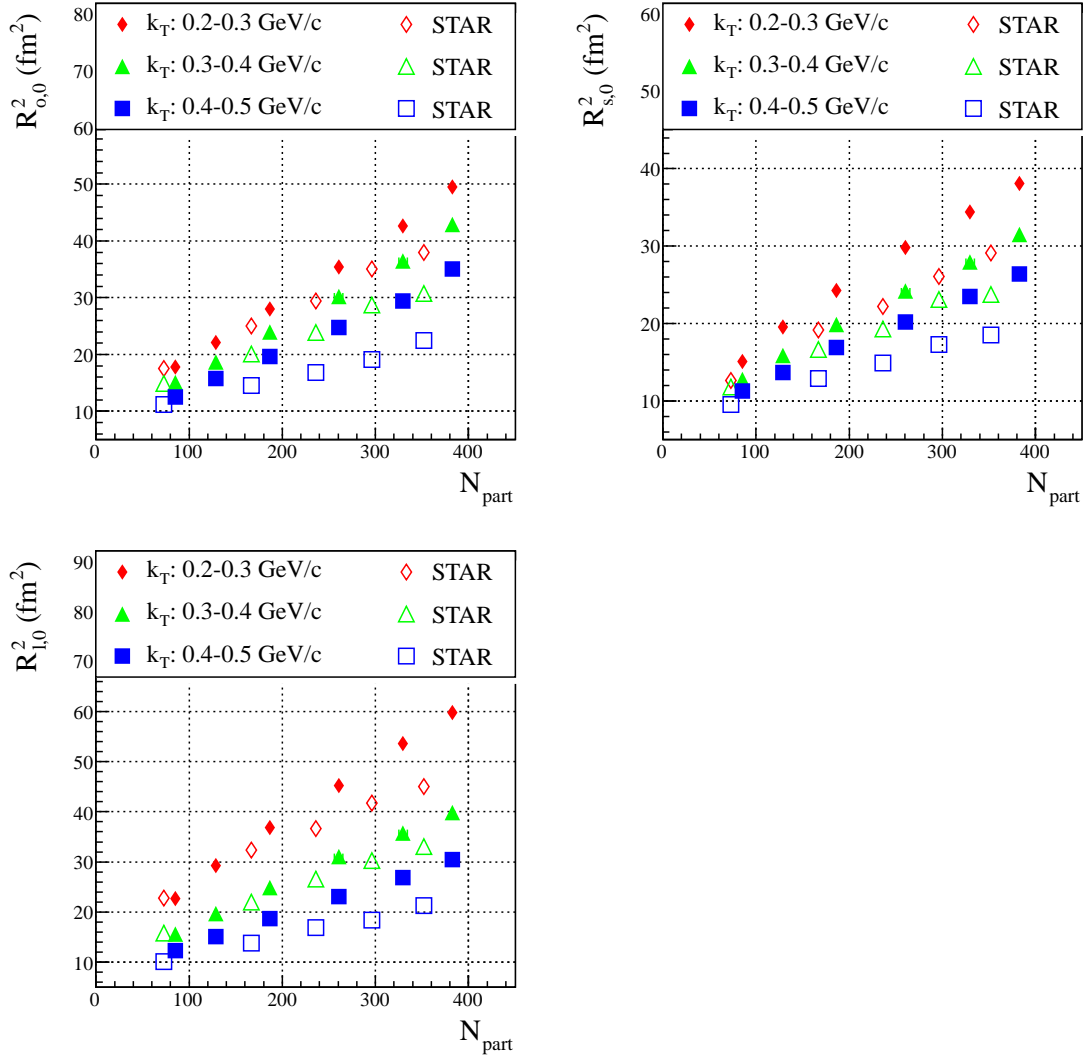


Figure 7.21.: Comparison with STAR results: average radii.

7.4. Summary

Azimuthally sensitive HBT interferometry can provide information about the source shape at freeze-out in addition to the size of the source. The freeze-out source shape is determined by the initial source geometry as well as by the pressure gradients and the lifetime of the source. Therefore, the analysis of the shape allows to constrain the initial shape as well as the evolution of the source.

Pb–Pb collision data that were recorded during the first heavy-ion run at the LHC in November 2010 has been analyzed. In order to extract the HBT radii correctly,

7. Azimuthally Sensitive HBT Interferometry

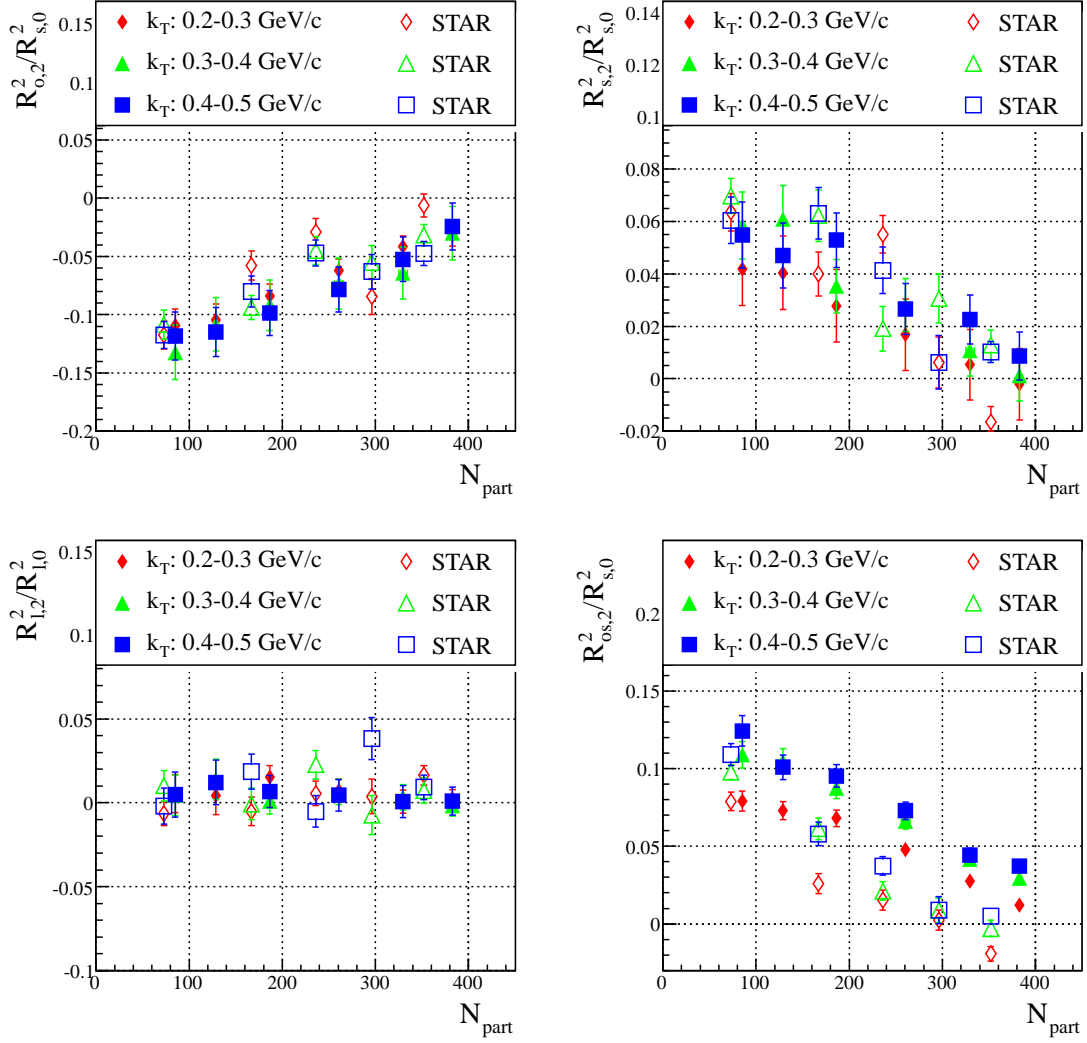


Figure 7.22.: Comparison with STAR results: radii oscillation amplitudes.

several correction procedures have to be applied, namely for finite momentum resolution, final-state Coulomb interaction, and event plane resolution. Systematic effects coming from the pair cut and event and track selection, variation of the fit range and Coulomb source size, magnetic field orientation, and fitting strategy are evaluated. In addition, the event plane resolution correction procedure leads to an additional uncertainty of 7% on the extracted oscillation amplitudes.

The observed azimuthal dependence of the transverse radii, i.e. their opposite oscillation, is consistent with a source that is extended out-of-plane at freeze-out. This means that, also at LHC energies, the initial asymmetry persists and is not significantly reduced or switched around as could be possible for long lifetimes (see

again Figure 7.2). The transverse radii and their cross-term show clear oscillations, whereas R_{long} , and the additional cross-terms are quite independent of φ . The average radii follow the expected trends concerning the centrality and k_T dependence. The oscillation amplitudes are found to increase from central to peripheral events. This is consistent with the geometrical shape of the overlapping region becoming more asymmetric for more peripheral events. The momentum dependence of the oscillations is not strong, the values suggest an increase of the amplitudes with pair momentum. The strong dependence of the oscillations on centrality and the weak dependence on k_T indicates a relation between the source geometry and not dominantly its dynamics.

The results were also compared to hydrodynamical calculations from the AZHYDRO and the KRAKOW model. AZHYDRO describes some qualitative features of the data well, but overestimated the absolute values of the amplitudes. The KRAKOW model overestimates the average radii, especially R_l , but describes the oscillation amplitudes quite well, only the amplitude of $R_{o,2}$ is underestimated. Compared to the results that were obtained at STAR, the average radii are about 20% higher, whereas the oscillation amplitudes are found to be very similar, even though the difference in collision energy is more than an order of magnitude. No significant reduction of the oscillation amplitudes is observed compared to STAR, although expected since the source at higher energies is presumed to have a longer life-time.

Altogether, the presented results demonstrate that azimuthally sensitive HBT interferometry is an interesting and important observable and can lead to constraints of the initial geometry and the medium evolution.

	k_T bin	0-5%			5-10%			10-30%			30-50%			50-70%			
		o	s	l	o	s	l	o	s	l	o	s	l	o	s	l	
pair cut	0	0.5%	0.5%	0.5%	estimated from most central bin												
	1	2%	1.5%	1.5%													
	2	4%	2%	2%													
	3	5%	3%	2.5%													
fits & cuts	0	2%	5%	1%	estimated from most central bin												
	1	6%	3%	1%													
	2	4%	2.5%	2%													
	3	2%	3%	1%													
fit range	0-2	<1%									1%						
	3	<1%									1.5%						
Coulomb	all	<1%									<1%	1.5%		<1%			
B field	all	<1%			1%		2%	1.5%		2%	3%		4%	3%		5%	
total	0	2.7%	5.3%	2.1%	2.7%	5.3%	2.7%	2.9%	5.4%	2.7%	3.9%	5.4%	4.5%	3.9%	5.4%	5.4%	
	1	6.6%	3.8%	2.5%	6.6%	3.8%	3.0%	6.7%	3.9%	3.0%	7.1%	4.8%	4.7%	7.1%	4.7%	5.5%	
	2	5.9%	3.6%	3.3%	5.9%	3.6%	3.7%	6.0%	3.8%	3.7%	6.6%	4.7%	5.2%	6.6%	4.6%	5.9%	
	3	5.7%	4.6%	3.2%	5.7%	4.6%	3.6%	5.8%	4.7%	3.6%	6.4%	5.6%	5.3%	6.4%	5.5%	6.1%	

Table 7.3.: Summary of systematic uncertainties on the HBT radii.

8. Summary and Outlook

Since November 2009 the experiments at the LHC at CERN record and analyze pp and Pb–Pb collisions at unprecedented energies. This thesis presented an analysis using two-particle correlations to measure the spatial extend of the fireball created in Pb–Pb collisions.

The study of high-energy heavy-ion collisions is especially interesting, since the so-called quark-gluon plasma, the state of matter shortly after the big bang, is expected to form in such collisions at LHC energies, where temperature and pressure are taken to be similar to the conditions in the early universe. From the detailed analysis of the reaction products in such collisions information on the properties of the quark-gluon plasma can be extracted. The short lifetime of the system prohibits a direct measurement of position and size of the hot and dense region. However, such information is encoded in particle correlations, their study is important to obtain a complete picture about the properties of the medium.

In this thesis the theoretical background of particle physics, the Standard Model, has been introduced. The basic characteristics of the quark-gluon plasma and the most important analysis approaches have been discussed. The ALICE experiment, its distinguishing features, and its sub-detectors have been explained. The concept of HBT interferometry, intensity interferometry of Bose–Einstein-correlated particles, has been outlined. The first ALICE results on HBT interferometry in Pb–Pb collisions at $\sqrt{s_{NN}} = 2.76$ TeV have been presented. They show that the extracted source radii are up to 20% larger than measured at RHIC in Au–Au collisions at an energy which was more than an order of magnitude lower than the one achieved at LHC. Furthermore, the results can only be described correctly by theoretical model calculations that combine a hydrodynamic evolution and hadronic rescattering. Pair reconstruction effects like track splitting and track merging affect the radii parameter extracted with an HBT analysis. In order to prevent a bias on the results, a pair cut has been developed. Its strategy and performance has been discussed in detail. The cut was found to be efficient in terms of avoiding an influence on the extracted HBT radii due to the two-track resolution. For the azimuthally sensitive HBT analysis, the reconstruction of the event plane is needed to estimate the collision geometry. An analysis framework has been developed to provide the event plane information for user analyses. The implemented method has been explained, as well as the details of the applied corrections. The framework was found to perform well

for all events that are more central than 80%, the event plane is reconstructed with a resolution better than 0.85. An azimuthally sensitive HBT analysis has been performed on Pb–Pb events at $\sqrt{s_{NN}} = 2.76$ TeV, measured with ALICE. The analysis strategy has been outlined and its systematic uncertainties have been studied. The transverse HBT radii oscillate as a function of the pair emission angle with respect to the event plane. The oscillations are consistent with a source extended out-of-plane. The amplitudes have been compared to two theoretical model calculations. AZHYDRO was found to overestimate the oscillations. In addition, this model predicted a sign-change of the amplitudes which is not observed in the measured results. This could be further confirmed with a detailed measurement of the low k_T regime in the future. Another calculation from the KRAKOW model was found to describe the oscillation amplitudes well, only in the *out* direction the oscillations were found to be significantly higher than predicted by the model. The comparison with data measured by the STAR experiment at RHIC showed that the oscillation amplitudes were measured to be similar at both experiments despite the large difference in collision energy and the therefore expected different life-times of the source.

In conclusion, the first results of azimuthally sensitive HBT interferometry are promising and interesting. The presented analysis can be a baseline for any further study of the details of the source shape. In the future the analysis could be extended to other particle species, unidentical particle correlations, or three- or four-particle analyses. In my opinion, it would be especially interesting to apply the concept of azimuthally sensitive HBT interferometry also in pp collisions, where the jet axis serves as an azimuthal reference. If oscillations are also observed in pp collisions, an actual geometry of the emission region might be rediscussed as an explanation.

Bibliography

- [1] F. Halzen, A. D. Martin, “Quarks and Leptons: An Introductory Course in Modern Particle Physics”, Wiley (1984).
- [2] D. E. Morrissey, T. Plehn, T. M. P. Tait, “Physics searches at the LHC”, arXiv:0912.3259 (2010).
- [3] F. Zwicky, “On the Masses of Nebulae and of Clusters of Nebulae”, *Astrophys. J.* 86, 217 (1937).
- [4] K. Nakamura et al. (PDG), “Review of Particle Physics”, *J. Phys. G* 37, 075021 (2010).
- [5] P. W. Higgs, “Broken Symmetries and the Masses of Gauge Bosons”, *Phys. Rev. Lett.* 13, 508 (1964).
- [6] M. E. Peskin, D. V. Schröder, “An introduction to quantum field theory”, Westview (2006).
- [7] S. Bethke, “The 2009 World Average of α_s ”, *Eur. Phys. J. C* 64, 689-703 (2009).
- [8] http://www.gsi.de/forschung/fair_experiments/CBM/Phasendiagramm.jpg.
- [9] T. DeGrand et al., “Masses and other parameters of the light hadrons”, *Phys. Rev. D* 12, 2060 (1975).
- [10] M. Cheng et. al., “Equation of state for physical quark masses”, *Phys. Rev. D* 81, 054504 (2010).
- [11] M. L. Miller, K. Reygers, S. J. Sanders, P. Steinberg, “Glauber Modeling in High Energy Nuclear Collisions”, *Ann. Rev. Nucl. Part. Sci.* 57, 205 (2007).
- [12] <http://star.physics.yale.edu/~salur/lightcone>.
- [13] H. Appelshäuser for the ALICE Collaboration, “Particle Production at Large Transverse Momentum with ALICE”, arXiv:1110.0638 (2011).
- [14] K. Aamodt et al., ALICE Collaboration, “Particle-yield modification in jet-like azimuthal di-hadron correlations in Pb-Pb collisions at $\sqrt{s_{NN}} = 2.76$ TeV”, arXiv:1110.0121 (2011).

- [15] A. Andronic et al., “Evidence for charmonium generation at the phase boundary in ultra-relativistic nuclear collisions”, *Phys. Lett. B* 652, 259 (2007).
- [16] K. Aamodt et al., ALICE Collaboration, “Elliptic Flow of Charged Particles in Pb-Pb Collisions at $\sqrt{s_{NN}} = 2.76$ TeV”, *Phys. Rev. Lett.* 105, 252302 (2010).
- [17] K. Aamodt et al., ALICE Collaboration, “The ALICE Experiment at the CERN LHC”, *JINST* 3, S08002 (2008).
- [18] CERN-EX-0708002 01, <http://cdsweb.cern.ch/record/1051740>.
- [19] LHC-PHO-1998-320, <http://cdsweb.cern.ch/record/841503>.
- [20] <http://ab-div.web.cern.ch/ab-div/Publications/LHC-DesignReport.html>.
- [21] ALICE Collaboration, Event Display, private communication (2011).
- [22] K. Aamodt et al., ALICE Collaboration, “Centrality Dependence of the Charged-Particle Multiplicity Density at Midrapidity in Pb-Pb Collisions at $\sqrt{s_{NN}} = 2.76$ TeV”, *Phys. Rev. Lett.* 106, 032301 (2011).
- [23] <http://aliceinfo.cern.ch/Public/en/Chapter2/Chap2Experiment-en.html>.
- [24] CERN-EX-071103001, <http://cdsweb.cern.ch/record/1091724>.
- [25] <https://alimonitor.cern.ch>.
- [26] R. Brun, F. Rademakers, “ROOT: An object oriented data analysis framework”, *Nucl. Instrum. Meth. A* 389, 81 (1997).
- [27] <http://aliweb.cern.ch/Offline>.
- [28] T. Sjöstrand, S. Mrenna, P. Skands, “A brief introduction to PYTHIA 8.1”, *Comput. Phys. Commun.* 178, 852 (2008).
- [29] R. Engel, J. Ranft, “Hadronic photon-photon interactions at high energies”, *Phys. Rev. D* 54, 4244 (1996).
- [30] M. Gyulassi, X. N. Wang, “HIJING 1.0: A Monte Carlo Program for Parton and Particle Production in High Energy Hadronic and Nuclear Collisions”, *Comput. Phys. Commun.* 83, 307 (1994).
- [31] A. Kisiel et al., “THERMINATOR: THERMal heavy-IoN generATOR”, *Comput. Phys. Commun.* 174, 669-687 (2006).
- [32] R. Brun et al., “Geant: Simulation Program for Particle Physics Experiments. User Guide and Reference Manual”, CERN-DD-78-2-REV (1978).
- [33] S. Agostinelli et al., “Geant4 - a simulation toolkit”, *Nucl. Instrum. Meth. A* 506, 250 (2003).

-
- [34] A. Fasso et al., “The physics models of FLUKA: status and recent development”, arXiv:hep-ph/0306267 (2003).
- [35] P. Billoir, “Progressive track recognition with a Kalman-like fitting procedure”, *Comput. Phys. Commun.* 57, 390 (1989).
- [36] R. Hanbury-Brown, R. Q. Twiss, “A Test of a New Type of Stellar Interferometer on Sirius”, *Nature* 178, 1046 (1956).
- [37] G. Goldhaber, S. Goldhaber, W. -Y. Lee, A. Pais, “Influence of Bose-Einstein Statistics on the Antiproton-Proton Annihilation Process”, *Phys. Rev.* 120, 300 (1960).
- [38] M. A. Lisa et al., “Femtoscopia in Relativistic Heavy Ion Collisions: Two Decades of Progress”, *Annu. Rev. Nucl. Part. Sci.* 55, 357-402 (2005).
- [39] U. Heinz, “How to extract physics from HBT radius parameters”, *Nucl. Phys. A* 610, 264c (1996).
- [40] U. A. Wiedemann et al., “Quantum mechanical localization effects for Bose-Einstein correlations”, *Phys. Rev. C* 56, 614 (1997).
- [41] U. A. Wiedemann, U. Heinz, “Particle Interferometry for Relativistic Heavy-Ion Collisions”, *Physics Reports* 319, 145-230 (1999).
- [42] U. Heinz et al., “Lifetimes and sizes from two-particle correlation functions”, *Phys. Lett. B* 382, 181-188 (1996).
- [43] M. G. Bowler, “Coulomb corrections to Bose-Einstein corrections have greatly exaggerated”, *Phys. Lett. B* 270, 69-74 (1991).
- [44] G. Baym, P. Braun-Munzinger, “Physics of Coulomb Corrections in Hanbury-Brown Twiss Interferometry in Ultrarelativistic Heavy Ion Collisions”, *Nucl. Phys. A* 610, 286c-296c (1996).
- [45] Y. Sinyukov, R. Lednicky, S. V. Akkelin, J. Pluta, B. Erasmus, “Coulomb corrections for interferometry analysis of expanding hadron systems”, *Phys. Lett. B* 432, 248 (1998).
- [46] S. V. Akkelin, Y. M. Sinyukov, “The HBT-interferometry of expanding sources”, *Phys. Lett. B* 356, 525 (1995).
- [47] K. Aamodt et al., ALICE Collaboration, “Two-pion Bose-Einstein correlations in central PbPb collisions at $\sqrt{s_{NN}} = 2.76$ TeV”, *Phys. Lett. B* 696, 328-337 (2011).
- [48] E. Frodermann, R. Chatterjee, U. Heinz, “Evolution of pion HBT radii from RHIC to LHC – Predictions from ideal hydrodynamics”, *J. Phys. G* 34, 2249-2254 (2007).

- [49] P. Bozek, M. Chojnacki, W. Florkowski, B. Tomasik, “Hydrodynamic predictions for Pb+Pb collisions at 2.76 TeV”, *Phys. Lett. B* 694, 238-241 (2010).
- [50] M. Chojnacki, W. Florkowski, W. Broniowski, A. Kisiel, “Soft heavy-ion physics from hydrodynamics with statistical hadronization: Predictions for collisions at 5.5 TeV”, *Phys. Rev. C* 78, 014905 (2008).
- [51] I. A. Karpenko, Y. M. Sinyukov, “Energy dependence of pion interferometry scales in ultra-relativistic heavy ion collisions”, *Phys. Lett. B* 688, 50-54 (2010).
- [52] N. Armesto (ed.) et al., “Heavy-ion collisions at the LHC - Last call for predictions”, *J. Phys. G* 35, 054001 (2008).
- [53] T. J. Humanic, “Hadronic observables from Au+Au collisions at $\sqrt{s_{NN}}=200$ GeV and Pb+Pb collisions at $\sqrt{s_{NN}}=5.5$ TeV from a simple kinematic model”, *Phys. Rev. C* 79, 044902 (2009).
- [54] T. J. Humanic, “Predictions of hadronic observables in Pb+Pb collisions at $\sqrt{s_{NN}} = 2.76$ TeV from a hadronic rescattering model”, arXiv:1011.0378 (2010).
- [55] J. L. Gramling, for the ALICE Collaboration, “Two-pion Bose-Einstein correlations in Pb-Pb collisions at $\sqrt{s_{NN}} = 2.76$ TeV measured with the ALICE experiment”, arXiv:1109.5366 (2011).
- [56] <http://www.quantumdiaries.org/wp-content/uploads/2011/02/FlowPr.jpg>.
- [57] S. A. Voloshin, A. M. Poskanzer, R. Snellings, “Collective phenomena in non-central nuclear collisions”, arXiv:0809.2949 (2008).
- [58] A. M. Poskanzer, S. A. Voloshin, “Methods for analyzing anisotropic flow in relativistic nuclear collisions”, *Phys. Rev. C* 58: 1671-1678 (1998).
- [59] K. H. Ackermann et al., “Elliptic flow in Au+Au collisions at $\sqrt{s_{NN}} = 130$ GeV”, *Phys. Rev. Lett.* 86: 402-407 (2001).
- [60] U. Heinz, A. Hummel, M. A. Lisa, U. A. Wiedemann, “Symmetry constraints for the emission angle dependence of Hanbury Brown–Twiss radii”, *Phys. Rev. C* 66, 044903 (2002).
- [61] J. Mercado, for the ALICE Collaboration, “Two-pion Bose-Einstein correlations in Pb-Pb collisions at 2.76 TeV with ALICE”, *J. Phys. G: Nucl. Part. Phys.* 38 124056 (2011).
- [62] A. Kisiel et al., “Azimuthally sensitive femtoscopy in hydrodynamics with statistical hadronization from the BNL Relativistic Heavy Ion Collider to the CERN Large Hadron Collider”, *Phys. Rev. C* 79, 014902 (2009).
- [63] W. Broniowski et al., “GLISSANDO: GLauber Initial-State Simulation AND more”, *Comput. Phys. Commun.* 180, 69-83 (2009).

- [64] J. Adams et al., STAR Collaboration, “Azimuthally sensitive Hanbury Brown-Twiss interferometry in Au+Au collisions at $\sqrt{s_{NN}} = 200$ GeV”, Phys. Rev. Lett. 93, 012301 (2004).

List of Figures

2.1.	$q\bar{q}$ pair from the vacuum	7
2.2.	Q dependence of α_s	9
2.3.	A sketch of the QCD phase diagram	11
2.4.	Evolution of heavy-ion collision	12
2.5.	LHC prediction from statistical hadronization	14
3.1.	View inside the LHC tunnel	16
3.2.	LHC dipole field lines	16
3.3.	ALICE event display	17
3.4.	The setup of the ALICE detector	18
3.5.	View inside the ALICE central barrel	19
4.1.	The Pratt–Bertsch parametrization	30
4.2.	Multiplicity dependence of the measured HBT radii	35
4.3.	Illustration of the k_T dependence of the radii	37
4.4.	k_T dependence of the measured HBT radii	38
4.5.	Homogeneity volume and decoupling time	39
5.1.	Two-dimensional ratio in $(\Delta\eta, \Delta\varphi)$	44
5.2.	Illustration of the variable $\Delta\varphi^*$	45
5.3.	Two-dimensional ratio in $(\Delta\eta, \Delta\varphi^*)$: different radii	46
5.4.	Two-dimensional ratio in $(\Delta\eta, \Delta\varphi^*)$: different k_T	46
5.5.	Projections in $\Delta\eta$ and $\Delta\varphi^*$ at different radial distances	47
5.6.	Projections in $\Delta\eta$ and $\Delta\varphi^*$ for different ranges in k_T	47
5.7.	Two-dimensional ratio in $\Delta\eta$ and $\Delta\varphi_{min}^*$	48
5.8.	Two-dimensional ratio in $\Delta\eta$ and $\Delta\varphi_{min,TPC}^*$	49
5.9.	Consideration of the opening angle	50
5.10.	Extracted widths of the inefficiency region	51
5.11.	Cut values for different k_T	52
5.12.	Two-dimensional ratio with and without the pair cut applied	53
5.13.	Correlation functions for different k_T bins.	54
5.14.	Sketch for <i>cowboy</i> and <i>sailor</i> pairs.	55
5.15.	Correlation functions for <i>cowboy</i> and <i>sailor</i> pairs	56
5.16.	HBT radii extracted for <i>cowboy</i> and <i>sailor</i> pairs	57
6.1.	Sketch of the reaction plane definition	60

6.2.	φ distribution for global tracks and TPC-only tracks	64
6.3.	Effect of φ correction	66
6.4.	Effect of p_T weights	67
6.5.	Control histograms produced by the <code>AliEPSelectionTask</code>	68
6.6.	Centrality dependence of Ψ_{EP} distribution	70
6.7.	φ and Ψ_{EP} distributions for different centrality ranges.	71
6.8.	Monte Carlo comparison	72
6.9.	Ψ_{subEP} differences with theoretical description	73
6.10.	Centrality dependence of the measured event plane resolution.	74
7.1.	The evolution of the source region	78
7.2.	Hydro calculation from KRAKOW model	78
7.3.	Illustration of the oscillation of the transverse radii	80
7.4.	Control histograms	82
7.5.	Two-dimensional projections of correlation function	83
7.6.	Momentum resolution correction	84
7.7.	Comparison of two different pair cuts	86
7.8.	Comparison with different analysis code	86
7.9.	Influence of the considered fit range on the extracted radii.	87
7.10.	Ratio of results that are obtained with different Coulomb source sizes.	88
7.11.	Ratio of correction procedures for the event plane resolution	89
7.12.	Azimuthal dependence of radii for different centrality bins	90
7.13.	Azimuthal dependence of cross-terms for different centrality bins	91
7.14.	Azimuthal dependence of radii for different k_T	92
7.15.	Azimuthal dependence of cross-terms for different k_T	93
7.16.	Average value for the radii parameters	94
7.17.	Normalized oscillation amplitudes	95
7.18.	Comparison with AZHYDRO model	96
7.19.	Comparison with KRAKOW model results: average radii.	97
7.20.	Comparison with KRAKOW model results: oscillation amplitudes	98
7.21.	Comparison with STAR results: average radii.	99
7.22.	Comparison with STAR results: radii oscillation amplitudes.	100

List of Tables

2.1. The Standard Model particles	5
5.1. Variables stored in the <code>NTuple</code>	42
5.2. Cuts applied in the two-track resolution study	43
5.3. Defined cut values.	51
6.1. Default track cuts applied in the <code>AliEPSelectionTask</code>	65
7.1. Default track cuts applied in the analysis.	81
7.2. Coulomb source sizes used to calculate the Coulomb interaction . . .	85
7.3. Summary of systematic uncertainties on the HBT radii.	102

Erklärung

Ich versichere, dass ich diese Arbeit selbständig verfasst und keine anderen als die angegebenen Quellen und Hilfsmittel benutzt habe.

Heidelberg, den 12.12.2011

.....

Johanna Lena Gramling